Micromagnetic Simulations of Ferromagnetic Domain Walls in Nanowires

Dissertation
zur Erlangung des Doktorgrades
des Fachbereichs Physik
der Universität Hamburg

vorgelegt von
Theo Gerhardt
aus Friedberg

Hamburg
2014

Gutachter der Dissertation:	PD Dr. Guido Meier
	Prof. Dr. Kornelius Nielsch
Gutachter der Disputation:	PD Dr. Guido Meier
	Prof. Dr. Ralf Röhlsberger
Datum der Disputation:	22. Januar 2015
Vorsitzender des Prüfungsausschusses:	Prof. Dr. Michael Rübhausen
Vorsitzender des Promotionsausschusses:	Prof. Dr. Daniela Pfannkuche
Dekan der MIN Fakultät:	Prof. Dr. Heinrich Graener

Abstract

In this work domain walls in nanowires with perpendicular magnetic anisotropy are investigated by means of micromagnetic simulations and analytical calculations. The creation of domain walls by field-induced switching is studied as well as the control of field- and current-driven domain-wall motion. In both cases a local reduction of the anisotropy constant is used in order to create artificial nucleation and pinning sites. The performed simulations reveal a local switching of the magnetization at the areas of reduced anisotropy. In dependence on the reduction of the anisotropy constant the corresponding switching fields decrease significantly. Eigenmode analysis is employed to determine the switching fields analytically. The calculated values are in excellent agreement with the data obtained by simulations. The local reduction of the anisotropy also creates an anisotropy boundary where the field- and current-driven domain walls get pinned. A one-dimensional model including the resulting pinning potential is derived in order to calculate the corresponding depinning fields and current densities. A perfect accordance between simulated and analytically obtained data is achieved. Depending on the characteristics of the anisotropy boundary an intrinsic and an extrinsic pinning regime can be identified. The one-dimensional model is furthermore employed to describe the rotational motion of a domain wall as it is driven through the anisotropy boundary. Again, a good agreement between the theoretical description and the micromagnetic simulation is obtained.

Zusammenfassung

In dieser Arbeit werden Domänenwände in Nanodrähten mit senkrechter magnetischer Anisotropie mit Hilfe von mikromagnetischen Simulationen und analytischen Berechnungen untersucht. Die Erzeugung von Domänenwänden durch feldinduziertes Schalten wird genauso studiert wie die Kontrolle von feld- und stromgetriebener Domänenwandbewegung. In beiden Fällen wird eine lokale Reduzierung der Anisotropiekonstanten benutzt, um künstliche Nukleations- bzw. Pinningzentren zu erzeugen. Die durchgeführten Simulationen zeigen ein lokales Schalten der Magnetisierung in den Bereichen mit reduzierter Anisotropie. In Abhängigkeit der Reduzierung der Anisotropiekonstanten verringert sich das entsprechende Schaltfeld erheblich. Um die Schaltfelder analytisch zu bestimmen, wird eine Eigenmodenanalyse verwendet. Die berechneten Werte stimmen exzellent mit den durch die Simulationen erhaltenen Daten überein. Die lokale Reduzierung der Anisotropie erzeugt auch eine Anisotropiegrenzfläche, an der die feld- und stromgetriebenen Domänenwände gepinnt werden. Ein eindimensionales Modell wird einschließlich des resultierenden Pinningpotentials hergeleitet, um die entsprechenden Depinningfelder und -stromdichten zu berechnen. Es wird eine perfekte Übereinstimmung zwischen simulierten und analytisch erlangten Daten erreicht. In Abhängigkeit der Eigenschaften der Anisotropiegrenzfläche kann ein intrinsisches und ein extrinsisches Pinningregime identifiziert werden. Das eindimensionale Modell wird des Weiteren verwendet, um die Rotationsbewegung einer Domänenwand zu beschreiben, während diese durch die Anisotropiegrenzfläche getrieben wird. Wieder wird dabei eine gute Übereinstimmung zwischen theoretischer Beschreibung und mikromagnetischer Simulation erreicht.

Contents

Chapter 1

Introduction

In the recent decade the investigation of domain-wall dynamics in nanowires has been a booming field of research due to new concepts of highly dense, ultrafast, and non-volatile storage devices [1,2]. Crucial prerequisites for the realization of these concepts are not only a frequent creation of data in form of magnetic domains, but also the controlled motion of the therewith associated domain walls to achieve a high data stability.

Several techniques for the local switching of the magnetization and hence the injection of domain walls into a nanowire have evolved over the years. Two prominent possibilities to create domains are the application of so-called nucleation pads [3–6] and Oersted fields generated by a current pulse through a strip line across the nanowire [7–11]. While the latter technique is appropriate for both in-plane magnetized samples and nanowires with perpendicular magnetic anisotropy (PMA), nucleation pads do not work reliably in PMA materials since demagnetization effects play a less important role. In contrast, inhomogeneities in form of defects or imperfections of the material's crystal structure turn out to act as nucleation centers for domains [12]. Theoretical investigations of the inhomogeneities in thin films especially determine a large impact of a modified anisotropy constant K_1 [13–15] which is why the creation of artificial nucleation sites by using these inhomogeneities is proposed. And indeed, intentional modifications of the material parameters as the anisotropy constant are a promising technique to inject domain walls in nanowires with perpendicular magnetic anisotropy. This has been confirmed by studies based on micromagnetic simulations [16, 17] and more or less accidentally by experiments as well [18, 19].

Although the injection of domain walls is well understood, the creation of reliable pinning sites to control the domain walls is a still demanding challenge. A promising approach to attain these goals is to apply local modifications to the material parameters, as well. Besides their role as nucleation center, defects and imperfections of the material‘s crystal structure influence the motion of field- and current-driven domain walls in nanowires, too, as has been shown by recent experiments [20, 21]. Based on these findings sev-

eral studies have been conducted to manipulate the domain-wall motion in a desired way. At first geometrical constrictions of nanowires have been investigated in in-plane magnetized materials [8, 22–26] and in media with perpendicular magnetic anisotropy – experimentally [27] and theoretically [28–30]. Since an accurate modification of the wire geometry is challenging, especially in narrow nanowires, in recent studies the local modification of the material parameters has been favored to create artificial pinning sites [17, 31–35]. The basic idea behind this concept is to make the energy of the system dependent on the position of the domain wall. In in-plane materials like permalloy this is achieved by the modification of the saturation magnetization M_s which can be realized by ion irradiation [36, 37]. In nanowires with perpendicular magnetic anisotropy usually the anisotropy constant K_1 is modified, also by ion irradiation [38–40]. A new promising approach is to manipulate the anisotropy constant by the application of electric fields. This allows for a dynamic modification of the material parameter and thus enables to create a switch for pinning sites [19, 41].

Throughout this thesis analytical calculations and micromagnetic simulations of nanowires with perpendicular magnetic anisotropy that comprise an intentional modification of the anisotropy constant are presented. The modifications of the material parameters act as artificial nucleation site for the field-induced injection of a domain wall as well as intentional pinning site for a field- or current-driven domain wall. In chapter 2 the theoretical basis in form of the micromagnetic model is introduced. The investigated material system and the functionality of micromagnetic simulations is discussed in chapter 3. Due to their importance for this work, domain walls are discussed in detail with respect to their characteristics, creation, dynamics, and pinning in chapter 4. The analytical calculations, which are performed in order to determine the switching field in a round nucleation site are based on eigenmode analysis. For the investigation of the domain-wall dynamics at the boundary that arises between the modification and the rest of the nanowire a one-dimensional model is employed. Furthermore, in combination with the energy landscape formed due to the pinning site the resulting depinning fields and depinning current densities are calculated in the same chapter. In chapter 5 all analytical calculations are consequently compared to data obtained by the micromagnetic simulations performed with the micromagnetic code MicroMagnum [42]. In addition, further interactions of the domain wall with the anisotropy boundary are discussed.

Chapter 2

Micromagnetism

The theoretical description of a ferromagnetic solid-state body is most accurate in a full quantum mechanical approach. In dependence on the included interactions between the particles that compose the ferromagnetic body a quantum mechanical theory can be very complex even for only few particles. For the analytical description of systems in the size of microns this approach is thus inappropriate.

To describe systems on larger than the sub-nanometer length scale, the theoretical model has to be simplified. As depicted in Tab. 2.1 a certain number of models is available for different length scales. Within its particular range each model approximately describes ferromagnetic phenomena under certain assumptions. But in dependence on the length scale of the investigated system they provide a sufficiently accurate theoretical description.

Systems on the submicron scale and domain-wall motion is investigated. On this length scale the micromagnetic model has proven to be accurate in comparison with experiments. Up to now, the widely used micromagnetic simulator OOMMF, which is based on this model has been cited 1600 times [44]. Since the micromagnetic model is able to resolve the inner structure of domain walls and can be numerically solved for sufficiently large systems, it is a reasonable choice for the description of the investigated

Model	**Description**	**Length Scale**
Atomistic theory	Quantum mechanical calculations	< 1 nm
Micromagnetic theory	Continuum theory of classical magnets	$1 - 1000$ nm
Domain theory	Magnetic microstructure and domains	$1 - 1000$ µm
Phase theory	Texture of magnetization directions	> 0.1 mm
Magnetic hysteresis	Average magnetization of a sample	always

Table 2.1: Models for the description of ferromagnetic phenomena on different length scales based on Fig. 1.5 in Ref. [43].

problems.

Throughout this chapter the prerequisites to work with the micromagnetic model are provided. The assumptions used by the micromagnetic model are discussed in Sec. 2.1. Section 2.2 explains the Landau-Lifshitz-Gilbert equation, which is the basic equation of motion in micromagnetism and describes the magnetization dynamics. In Sec. 2.3 the effective field is derived. It is the driving force of the dynamics and originates from the different energy contributions in a ferromagnetic body. The chapter finishes with Sec. 2.4 which gives an overview of the applicability of micromagnetism.

2.1 Assumptions in Micromagnetism

In general, magnetism of solid-state bodies originates from the intrinsic spin and the orbital momentum of electrons of single atoms. Each of these charges can be connected with a dipole that can be identified with an elementary magnet. On a macroscopic scale these magnetic moments can have a cumulative effect due to the interaction of the electrons on the atomic scale.

The inherent characteristics of a material can cause a parallel spin alignment of adjacent electrons with overlapping wave functions. This results in a ferromagnetic behavior with a net magnetic moment. The responsible effect is the so-called exchange interaction which describes an energy splitting between parallel and anti-parallel aligned spins (see Sec. 2.3.3). The energy cost due to a misalignment allows for the assumption that adjacent elementary magnets $\boldsymbol{m}_\mathrm{i}$ at positions $\boldsymbol{r}_\mathrm{i}$ are aligned almost parallel and there are no abrupt changes:

$$|\boldsymbol{m}_\mathrm{i} - \boldsymbol{m}_\mathrm{j}| \approx 0 \qquad \text{for} \qquad |\boldsymbol{r}_\mathrm{i} - \boldsymbol{r}_\mathrm{j}| < l_\mathrm{ex}. \tag{2.1.1}$$

Here, l_ex is the exchange length, a measure for the range of the exchange interaction. Another assumption is the homogeneous density of electrons and thereby elementary magnets in the ferromagnetic material. Thus – having the parallel alignment in mind – on a larger than the atomic length scale the discrete distribution of elementary magnetic moments $\boldsymbol{m}_\mathrm{i}$ can be transformed into a continuous vector field $\boldsymbol{M}(\boldsymbol{r})$ referred to as magnetization. The exchange interaction assures that

$$\int_V \boldsymbol{M}(\boldsymbol{r})\,\mathrm{d}\boldsymbol{r} \approx \sum_{i \text{ in } V} \boldsymbol{m}_\mathrm{i}(\boldsymbol{r}_\mathrm{i}) \qquad \text{and thus} \qquad \boldsymbol{M}(\boldsymbol{r}) = \frac{\sum_i \boldsymbol{m}_\mathrm{i}}{V} \tag{2.1.2}$$

holds true for a certain volume V with an upper boundary of l_ex^3. The modulus of the magnetization is constant since the density of the elementary magnets is homogeneous:

$$\boldsymbol{M} = M_\mathrm{s} \cdot \boldsymbol{m} \qquad \text{and} \qquad |\boldsymbol{m}| = 1. \tag{2.1.3}$$

M_s is referred to as the saturation magnetization and $\boldsymbol{m}$ is the so-called reduced magnetization.

The magnetization is a central parameter in the micromagnetic model and its dynamics are described by the Landau-Lifshitz-Gilbert equation. Although this equation is of classical origin, the assumption of a slowly varying magnetization in the ferromagnetic body is a result of the consideration of quantum mechanical effects as the exchange interaction, see Sec. 2.3.3. Thus micromagnetism is a semi-classical model that can be used to describe much smaller structures than can be investigated in a classical theory.

2.2 Landau-Lifshitz-Gilbert Equation

The central equation of micromagnetism that describes the temporal evolution of a magnetic moment in an effective magnetic field is the Landau-Lifshitz-Gilbert equation. In its original form it was first proposed by L. D. Landau and E. M. Lifshitz in 1935 [45] and consists of a physically derived precession term and a phenomenological damping term. The latter accounts for the relaxation of a magnetic moment and is believed to be caused by relativistic interactions, see Sec. 2.2.2. Since the original approach encounters problems at large damping in 1955 Gilbert proposed an equation that is based on a Lagrangian approach and takes large damping into account [46, 47].

In this section the Landau-Lifshitz-Gilbert equation is derived from a quantum mechanical approach. Then the damping term is introduced and the difference between the Landau-Lifshitz and the Gilbert approach is discussed. The properties with respect to micromagnetism and general physics are briefly sketched as well. Finally, the Landau-Lifshitz-Gilbert equation will be extended by the interaction of a magnetic moment with a spin-polarized current.

2.2.1 Quantum Mechanical Approach

As described in Sec. 2.1 the continuous magnetization in micromagnetism is conducted from spins that are discrete in space and orientation. In quantum mechanics a single spin is described by the operator $\widehat{\boldsymbol{S}}$. The temporal evolution of the j-th component of the spin operator is given by the Heisenberg equation

$$\frac{\mathrm{d}\widehat{S}_\mathrm{j}}{\mathrm{d}t} = \frac{1}{i\hbar}\left[\widehat{S}_\mathrm{j}, \widehat{H}\right]. \tag{2.2.1}$$

Since the Hamiltonian $\widehat{H}$ of the system in micromagnetism usually depends on the spin, an expansion of the Hamiltonian in spin operators is reasonable

$$[\widehat{S}_\mathrm{j}, \widehat{H}] = -\sum_k \frac{\partial \widehat{H}}{\partial \widehat{S}_\mathrm{k}} [\widehat{S}_\mathrm{k}, \widehat{S}_\mathrm{j}] + \mathcal{O}(\hbar^2). \tag{2.2.2}$$

Use of the commutation rule for angular momenta $[\widehat{S}_\mathrm{k}, \widehat{S}_\mathrm{j}] = -i\hbar \sum_l \epsilon_{\mathrm{jkl}} \widehat{S}_\mathrm{l}$ yields

$$[\widehat{S}_\mathrm{j}, \widehat{H}] = i\hbar \sum_{k,l} \frac{\partial \widehat{H}}{\partial \widehat{S}_\mathrm{k}} \epsilon_{\mathrm{jkl}} \widehat{S}_\mathrm{l} + \mathcal{O}(\hbar^2). \tag{2.2.3}$$

Inserting into Eqn. 2.2.1 and expressing the ϵ-tensor as cross product the time development of the spin $\widehat{\boldsymbol{S}}$ results in

$$\frac{\mathrm{d}\widehat{\boldsymbol{S}}}{\mathrm{d}t} = -\widehat{\boldsymbol{S}} \times \frac{\partial \widehat{H}}{\partial \widehat{\boldsymbol{S}}} + \mathcal{O}(\hbar) \tag{2.2.4}$$

where the partial differentiation is defined by $\partial/\partial \boldsymbol{S} = \left(\partial/\partial S_\mathrm{x}, \partial/\partial S_\mathrm{y}, \partial/\partial S_\mathrm{z}\right)$. In the classical limit $\hbar \to 0$ is assumed and thus the last term can be omitted. According to the Ehrenfest theorem the operators are then replaced by their expectation values and the spin can be connected with the macroscopic magnetic moment

$$\boldsymbol{M} = -\gamma^* \langle \widehat{\boldsymbol{S}} \rangle \tag{2.2.5}$$

with the gyromagnetic ratio $\gamma^* = g\mu_\mathrm{B}/\hbar$, where g is the Landé factor and μ_B is the Bohr magneton. Furthermore, the expectation value of the Hamiltonian is defined by the energy E of the system $\langle \widehat{H} \rangle = E$. Inserting both in Eqn. 2.2.4 yields

$$\frac{\mathrm{d}\boldsymbol{M}}{\mathrm{d}t} = \gamma^* \boldsymbol{M} \times \frac{\partial E}{\partial \boldsymbol{M}}. \tag{2.2.6}$$

In the continuum limit, which is used in the micromagnetic model, the partial differentiation is replaced by the variational derivative $\delta E/\delta \boldsymbol{M}$. A change of the energy E of the system as a result of the change of the magnetic moment M is correlated with the existence of an effective field, since $\delta E = -\mu_0 \, \delta \boldsymbol{M} \cdot \boldsymbol{H}_\mathrm{eff}$. We can thus define

$$\boldsymbol{H}_\mathrm{eff} = -\frac{1}{\mu_0} \frac{\delta E}{\delta \boldsymbol{M}}, \tag{2.2.7}$$

which will be discussed in detail in Sec. 2.3. Inserting this expression into Eqn. 2.2.6 yields the temporal evolution of a magnetic moment $\boldsymbol{M}$ in an effective magnetic field $\boldsymbol{H}_\mathrm{eff}$

$$\frac{\mathrm{d}\boldsymbol{M}}{\mathrm{d}t} = -\gamma \boldsymbol{M} \times \boldsymbol{H}_\mathrm{eff} \tag{2.2.8}$$

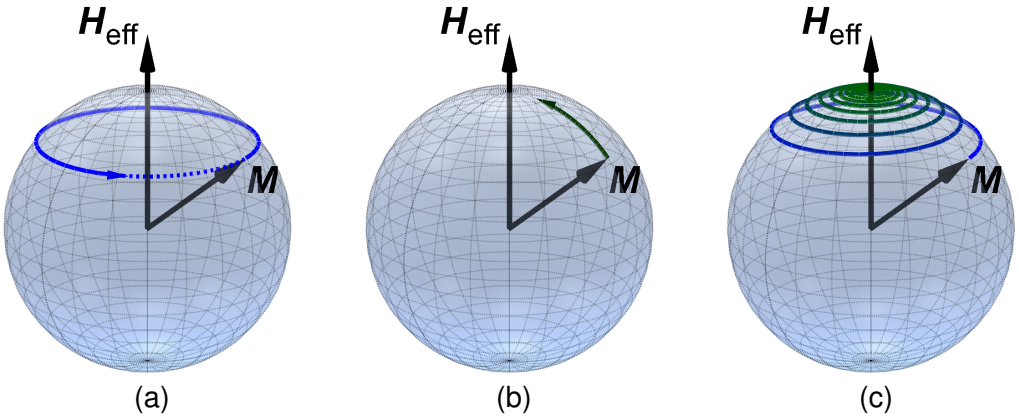

Figure 2.1: Depiction of the temporal evolution of a single magnetic moment $\boldsymbol{M}$ in the effective field $\boldsymbol{H}_{\text{eff}}$ as described by the Landau-Lifshitz-Gilbert equation. (a) Undamped precessional motion of $\boldsymbol{M}$ around $\boldsymbol{H}_{\text{eff}}$. (b) Relaxation of the magnetic moment towards the effective field due to dissipation effects. (c) Combined time evolution of the magnetic moment including precession and damping. In the end $\boldsymbol{M}$ is aligned in parallel with the effective field.

with $\gamma = g\mu_0\mu_B/\hbar$. This equation describes a precessional motion of the magnetization $\boldsymbol{M}$ around the field $\boldsymbol{H}_{\text{eff}}$ without any loss of energy resulting in a stationary oscillation of the magnetic moment as depicted in Fig. 2.1(a). Accordingly the right-hand side of Eqn. 2.2.8 is referred to as precessional term of the Landau-Lifshitz-Gilbert equation. In fact, magnetic moments relax into an energetic equilibrium parallel to the effective field due to dissipative effects.

2.2.2 Damping Term

Landau and Lifshitz as well as Gilbert introduced a phenomenological damping term that accounts for the dissipation, see Fig. 2.1(b). The former believed the relaxation of the magnetic moment $\boldsymbol{M}$ towards the effective field $\boldsymbol{H}_{\text{eff}}$ is due to a weak relativistic interaction. Thus Landau and Lifshitz introduced a term pointing towards $\boldsymbol{H}_{\text{eff}}$ which results in the magnetization dynamics to be described by

$$\frac{\mathrm{d}\boldsymbol{M}}{\mathrm{d}t} = -\gamma \boldsymbol{M} \times \boldsymbol{H}_{\text{eff}} - \frac{\lambda}{M_s^2}\, \boldsymbol{M} \times (\boldsymbol{M} \times \boldsymbol{H}_{\text{eff}}) \tag{2.2.9}$$

where $\lambda \ll \gamma M_s$ [45]. Gilbert on the other hand argued that the damping force on the magnetization field is the result of a classical energy transfer from macroscopic motion to microscopic thermal motion in the form of spin waves, phonons, and thermal excitation of conduction electrons [47]. Thus in his Lagrangian formulation of the motion equation of a magnetic moment he added a Rayleigh dissipation function which is

proportional to the velocity resulting in

$$\frac{\mathrm{d}\boldsymbol{M}}{\mathrm{d}t} = -\gamma \boldsymbol{M} \times \boldsymbol{H}_{\mathrm{eff}} + \frac{\alpha}{M_{\mathrm{s}}} \boldsymbol{M} \times \frac{\mathrm{d}\boldsymbol{M}}{\mathrm{d}t}. \tag{2.2.10}$$

Both equations are similar and lead to a parallel alignment of the magnetic moment $\boldsymbol{M}$ with the effective field $\boldsymbol{H}_{\mathrm{eff}}$ – but only for small damping with $\alpha \ll 1$. This becomes apparent if the implicit form of Eqn. 2.2.10 is transformed into an explicit form, which is comparable to Eqn. 2.2.9. This is done by applying the cross product with $\boldsymbol{M}$ from left on both sides and using the Grassman identity $\boldsymbol{a} \times (\boldsymbol{b} \times \boldsymbol{c}) = (\boldsymbol{a} \cdot \boldsymbol{c})\boldsymbol{b} - (\boldsymbol{a} \cdot \boldsymbol{b})\boldsymbol{c}$ which yields with some transformations

$$\boldsymbol{M} \times \frac{\mathrm{d}\boldsymbol{M}}{\mathrm{d}t} = -\gamma \boldsymbol{M} \times (\boldsymbol{M} \times \boldsymbol{H}_{\mathrm{eff}}) - \alpha M_{\mathrm{s}} \frac{\mathrm{d}\boldsymbol{M}}{\mathrm{d}t}. \tag{2.2.11}$$

Inserting Eqn. 2.2.11 into Eqn. 2.2.10 results with minor transformations in

$$\frac{\mathrm{d}\boldsymbol{M}}{\mathrm{d}t} = -\gamma' \boldsymbol{M} \times \boldsymbol{H}_{\mathrm{eff}} - \frac{\alpha'}{M_{\mathrm{s}}} \boldsymbol{M} \times (\boldsymbol{M} \times \boldsymbol{H}_{\mathrm{eff}}) \tag{2.2.12}$$

where

$$\gamma' = \frac{\gamma}{1+\alpha^2} \quad \text{and} \quad \alpha' = \frac{\alpha\gamma}{1+\alpha^2}. \tag{2.2.13}$$

Thus with $\lambda = \alpha\gamma M_{\mathrm{s}}$ Eqns. 2.2.12 and 2.2.9 differ only by a factor of $\left(1+\alpha^2\right)^{-1}$ in the gyromagnetic ratio. For a static magnetization this factor has no effect. But in dynamics it acts as a renormalization to the velocity of the magnetic moment, based on the fact that a damped system moves slower. Thus the damping term introduced by Gilbert takes large damping into account. Nevertheless, the dimensionless Gilbert damping parameter α has to be determined in experiments and is usually found to be $\alpha \ll 1$. Equation 2.2.12 is known as the Landau-Lifshitz-Gilbert equation which is commonly used in micromagnetic simulations. The resulting motion of a magnetic moment $\boldsymbol{M}$ and its parallel alignment with an effective field $\boldsymbol{H}_{\mathrm{eff}}$ are depicted in Fig. 2.1(c).

2.2.3 Properties of the Landau-Lifshitz-Gilbert Equation

Energy of the Magnetic System

Besides the temporal evolution of the magnetic moments the Landau-Lifshitz-Gilbert equation allows for a prediction of the time development of the energy E of a magnetic system. If the effective field is not explicitly time dependent, the energy density U can be written as

$$\frac{\mathrm{d}U}{\mathrm{d}t} = \frac{\delta E}{\delta \boldsymbol{M}} \cdot \frac{\mathrm{d}\boldsymbol{M}}{\mathrm{d}t} \tag{2.2.14}$$

$$= -\mu_0 \boldsymbol{H}_{\mathrm{eff}} \cdot \boldsymbol{M}. \tag{2.2.15}$$

Inserting the Landau-Lifshitz-Gilbert equation (Eqn. 2.2.12) and integrating over space to obtain the time development of the energy E yields

$$\frac{\mathrm{d}E}{\mathrm{d}t} = -\mu_0 \int_V \boldsymbol{H}_{\mathrm{eff}} \cdot \left(-\gamma' \boldsymbol{M} \times \boldsymbol{H}_{\mathrm{eff}} - \frac{\alpha'}{M_{\mathrm{s}}} \boldsymbol{M} \times (\boldsymbol{M} \times \boldsymbol{H}_{\mathrm{eff}}) \right) \mathrm{d}\boldsymbol{r} \tag{2.2.16}$$

$$= -\mu_0 \alpha' \int_V |\boldsymbol{M} \times \boldsymbol{H}_{\mathrm{eff}}|^2 \, \mathrm{d}\boldsymbol{r} \tag{2.2.17}$$

$$\leq 0. \tag{2.2.18}$$

Thus the energy of a magnetic system never increases over time. Especially in the case of a non-damped system with $\alpha = 0$ the system energy is constant and a magnetic moment remains in an ongoing precession around the effective field. In the case of $\alpha > 0$ dissipation is present and as long as the magnetic moments precess the system is losing energy. Consequently, if the magnetic moments are relaxed and aligned in parallel with the effective field the system is in a local energy minimum. Hence every rotation of a magnetic moment means transformation of the system into an energetically favorable state, referred to as relaxation.

Preservation of Modulus

A prerequisite for the description of the temporal evolution of a magnetic moment within the micromagnetic model with the Landau-Lifshitz-Gilbert equation is the preservation of the modulus of the magnetic moment $\boldsymbol{M}$ as postulated in Sec. 2.1. To check for this feature it is possible to calculate the time development of the squared magnetization

$$\frac{\mathrm{d}}{\mathrm{d}t} |\boldsymbol{M}|^2 = \frac{\mathrm{d}}{\mathrm{d}t} (\boldsymbol{M} \cdot \boldsymbol{M}) = 2\boldsymbol{M} \cdot \frac{\mathrm{d}\boldsymbol{M}}{\mathrm{d}t}. \tag{2.2.19}$$

Inserting Eqn. 2.2.12 yields

$$\frac{\mathrm{d}}{\mathrm{d}t} |\boldsymbol{M}|^2 = 2\boldsymbol{M} \cdot \left(-\gamma' \boldsymbol{M} \times \boldsymbol{H}_{\mathrm{eff}} - \frac{\alpha'}{M_{\mathrm{s}}} \boldsymbol{M} \times (\boldsymbol{M} \times \boldsymbol{H}_{\mathrm{eff}}) \right) = 0 \tag{2.2.20}$$

Thus the modulus of the magnetization is preserved by the Landau-Lifshitz-Gilbert equation.

2.2.4 Extension with Spin-polarized Current

Besides a magnetic field there are alternatives to manipulate the magnetization of a ferromagnet. One possibility is to exert a torque on the magnetic moments by applying a spin-polarized current. The idea to influence the magnetization by currents was first proposed by L. Berger in 1978 by the means of current-driven domain-wall motion [48]. He suggested that electrons passing a domain wall apply a torque since their spins

are flipped and angular momentum is conserved. This torque is referred to as spin-transfer torque and its origin is explained by the so-called *sd*-model that is employed to describe the magnetic transition metals iron, cobalt, and nickel. While the electrons in the *d*-band account for the magnetization since they are localized, the electrons of the *s*-band can move freely through a sample resulting in a current if a voltage is applied. Thus they are referred to as itinerant or conducting electrons. Due to the exchange interaction between spins the *s*-electrons align in parallel with the *d*-electrons and thus with the magnetization as they move. In this case the exchange interaction is hence called *sd*-interaction and in a constant magnetization the current gets polarized.

If such a polarized current flows through an area of varying magnetization the spin of the electrons align in parallel with the magnetization. The change of the direction is usually adiabatic since adjacent magnetic moments in the sample align almost parallel, see Sec. 2.1. Due to the conservation of angular momentum the passing electrons of the s-band have to exert a torque on the local electrons of the d-band as they follow the magnetization direction. This results in a change of the local magnetization as described by L. Berger [48–50] and J. C. Slonczewski [51].

The first who included the adiabatic spin-transfer torque into the Landau-Lifshitz-Gilbert equation were Y. B. Bazaliy *et al.* [52] in 1998. They considered the conducting electrons to be non-interacting and thus made the assumption of a ballistic electron transport. But this is not the entire truth since conduction electrons experience damping. In 2004 S. Zhang and Z. Li followed another approach, starting from the generalized spin-continuity equation and taking spin scattering into account [53]. In the following the full spin-transfer torque that extends the Landau-Lifshitz-Gilbert equation with the interaction of a magnetic moment and a spin-polarized current is calculated according to the original publication.

If $\widehat{\boldsymbol{s}}$ is the spin operator of the itinerant electrons and $\widehat{J}$ is the spin-current operator, the spin-continuity equation reads

$$\frac{\partial \widehat{\boldsymbol{s}}}{\partial t} + \boldsymbol{\nabla} \cdot \widehat{J} = \frac{1}{i\hbar}\left[\widehat{\boldsymbol{s}}, \widehat{H}_{\mathrm{sd}}\right] + \frac{1}{i\hbar}\left[\widehat{\boldsymbol{s}}, \widehat{H}_{\mathrm{scat}}\right]. \tag{2.2.21}$$

While the second term on the right-hand side accounts for a torque due to scattering of the itinerant electrons with impurities, the first term corresponds to a torque that results from the *sd*-interaction between conducting and localized electrons. The *sd*-Hamiltonian

$$\widehat{H}_{\mathrm{sd}} = -J_{\mathrm{ex}}\, \widehat{\boldsymbol{s}} \cdot \widehat{\boldsymbol{S}} \tag{2.2.22}$$

is used to model the *sd*-interaction, where J_{ex} is the exchange constant and $\widehat{\boldsymbol{S}}$ is the spin of a localized electron. A semi-classical picture as in Sec. 2.2.1 is used and thus the operators are replaced by their expectation values. In the case of the localized spin the expectation value $\langle \widehat{\boldsymbol{S}} \rangle$ can be further replaced by its corresponding magnetization

$\boldsymbol{M} = -M_\mathrm{s}\langle\widehat{\boldsymbol{S}}\rangle/S$. The expectation value of the itinerant electron spin $\langle\widehat{\boldsymbol{s}}\rangle$ and the spin current $\langle\widehat{J}\rangle$ are replaced by a corresponding electron spin density $\boldsymbol{m} = \langle\widehat{\boldsymbol{s}}\rangle$ – which acts like an induced magnetization – and a spin current density $J = \langle\widehat{J}\rangle$. Explicit calculation of the first commutator on the right-hand side of Eqn. 2.2.21 and the transition to the classical limit yields

$$\frac{\partial \boldsymbol{m}}{\partial t} + \boldsymbol{\nabla} \cdot J = -\frac{SJ_\mathrm{ex}}{M_\mathrm{s}} \boldsymbol{m} \times \boldsymbol{M} + \langle \Gamma_\mathrm{re} \rangle \tag{2.2.23}$$

where $\langle\Gamma_\mathrm{re}\rangle$ expresses the relaxation of itinerant electrons due to scattering. The spin density can now be divided into two parts:

$$\boldsymbol{m} = m_0 \frac{\boldsymbol{M}}{M_\mathrm{s}} + \delta\boldsymbol{m}. \tag{2.2.24}$$

The first part m_0 follows the direction of the local magnetization $\boldsymbol{M}$ and is referred to as equilibrium magnetization or equilibrium spin density. The second part of the induced magnetization $\boldsymbol{m}$ is defined perpendicular to $\boldsymbol{M}$ and known as non-equilibrium magnetization $\delta\boldsymbol{m}$. The damping $\langle\Gamma_\mathrm{re}\rangle$ of the itinerant electrons is assumed to be proportional to the non-equilibrium magnetization $\delta\boldsymbol{m}$. In addition, the coefficient τ_sf is used to denote the average time before an itinerant electron is scattered and its spin flips. Likewise, the exchange relaxation time $\tau_\mathrm{ex} = 1/SJ_\mathrm{ex}$ is defined. Furthermore, higher orders in response of $\delta\boldsymbol{m}$ to the time derivate of the magnetization than the first are neglected (see Ref. [53]) and the spin current density J is expressed by an electric current density $\boldsymbol{j}$ times a magnetic moment connected with an electron. With all assumptions, expressions, and inserting Eqn. 2.2.24, Eqn. 2.2.23 can be written as

$$\frac{m_0}{M_\mathrm{s}} \frac{\partial \boldsymbol{M}}{\partial t} - \frac{\mu_\mathrm{B} P}{e M_\mathrm{s}} (\boldsymbol{j} \cdot \boldsymbol{\nabla}) \boldsymbol{M} = -\frac{1}{\tau_\mathrm{ex} M_\mathrm{s}} \delta\boldsymbol{m} \times \boldsymbol{M} - \frac{\delta\boldsymbol{m}}{\tau_\mathrm{sf}} \tag{2.2.25}$$

where e is the electron charge and P is the spin current polarization of the ferromagnet. From Eqn. 2.2.25 it is possible to immediately recognize two source terms for the non-equilibrium spin density $\delta\boldsymbol{m}$ – the time variation and the spatial variation of the magnetization $\boldsymbol{M}$, both damping terms with different relaxation times. This implicit equation can be transformed into an explicit expression for the non-equilibrium magnetization $\delta\boldsymbol{m}$ by using vector manipulations similar to Sec. 2.2.2 and then reads

$$\delta\boldsymbol{m} = \frac{\tau_\mathrm{ex}}{1+\xi^2} \left[-\frac{\xi m_0}{M_\mathrm{s}} \frac{\partial \boldsymbol{M}}{\partial t} + \frac{\xi \mu_\mathrm{B} P}{e M_\mathrm{s}} (\boldsymbol{j} \cdot \boldsymbol{\nabla}) \boldsymbol{M} - \frac{m_0}{M_\mathrm{s}^2} \boldsymbol{M} \times \frac{\partial M}{\partial t} + \frac{\mu_\mathrm{B} P}{e M_\mathrm{s}^2} \boldsymbol{M} \times (\boldsymbol{j} \cdot \boldsymbol{\nabla}) \boldsymbol{M} \right]. \tag{2.2.26}$$

Here, the relation $\xi = \tau_\mathrm{ex}/\tau_\mathrm{sf}$ between the relaxation times is used. From Eqn. 2.2.22 it is possible to calculate an additional torque $\boldsymbol{T}$ on the magnetization quite analogously to Sec. 2.2.1, which reads in the classical limit

$$\boldsymbol{T} = -\frac{SJ_\mathrm{ex}}{M_\mathrm{s}} \boldsymbol{M} \times \boldsymbol{m} = -\frac{1}{\tau_\mathrm{ex} M_\mathrm{s}} \boldsymbol{M} \times \delta\boldsymbol{m}. \tag{2.2.27}$$

Zhang and Li argue that for typical ferromagnets m_0 is much smaller than the saturation magnetization M_s and thus the first and the third term of Eqn. 2.2.26 can be omitted. Inserting Eqn. 2.2.26 into Eqn. 2.2.27 then yields

$$\boldsymbol{T} = \underbrace{-\frac{b_j}{M_s^2}\boldsymbol{M}\times[\boldsymbol{M}\times(\boldsymbol{j}\cdot\boldsymbol{\nabla})\boldsymbol{M}]}_{\text{adiabatic spin torque}} \underbrace{-\frac{\xi b_j}{M_s}\boldsymbol{M}\times(\boldsymbol{j}\cdot\boldsymbol{\nabla})\boldsymbol{M}}_{\text{non-adiabatic spin torque}} \tag{2.2.28}$$

with

$$b_j = \frac{\mu_B P}{eM_s\left(1+\xi^2\right)}. \tag{2.2.29}$$

The adiabatic spin-transfer torque describes the adiabatic process of the non-equilibrium conduction electrons as already found by Y. B. Bazaliy *et al.* [52], namely the parallel alignment of the electrons with the magnetization. The non-adiabatic spin-transfer torque is new and accounts for scattering and thus damping of the itinerant electrons. Although it is much smaller than the adiabatic torque it has a large impact on the manipulation of the magnetization $\boldsymbol{M}$ by a spin-polarized current density $\boldsymbol{j}$ [54]. Since the prefactor of the non-adiabatic torque differs from the prefactor of the adiabatic torque by the factor ξ, which is the relation between the relaxation times, this factor is also referred to as non-adiabaticity. Adding the torque $\boldsymbol{T}$ to Eqn. 2.2.10 yields the implicit Landau-Lifshitz-Gilbert equation extended by a spin-transfer torque due to spin-polarized currents. Transformations yield the explicit form which reads

$$\begin{aligned}\frac{\mathrm{d}\boldsymbol{M}}{\mathrm{d}t} =& -\gamma'\boldsymbol{M}\times\boldsymbol{H}_{\text{eff}} - \frac{\alpha'}{M_S}\boldsymbol{M}\times(\boldsymbol{M}\times\boldsymbol{H}_{\text{eff}}) \\ &- \frac{1+\xi\alpha}{1+\alpha^2}\frac{b_j}{M_s^2}\boldsymbol{M}\times[\boldsymbol{M}\times(\boldsymbol{j}\cdot\boldsymbol{\nabla})\boldsymbol{M}] - \frac{1-\alpha\xi^{-1}}{1+\alpha^2}\frac{\xi b_j}{M_s}\boldsymbol{M}\times(\boldsymbol{j}\cdot\boldsymbol{\nabla})\boldsymbol{M}.\end{aligned} \tag{2.2.30}$$

While the adiabatic torque usually results in a displacement of e.g. a domain wall and the non-adiabatic torque distorts the domain wall, the torques are referred to motion term and distortion term. Equation 2.2.30 is the basis to describe the time evolution of a magnetic moment $\boldsymbol{M}$ in an effective field $\boldsymbol{H}_{\text{eff}}$ that is additionally manipulated by a spin-polarized current $\boldsymbol{j}$ in all simulations throughout this thesis.

2.3 Effective Field

The dynamics of a magnetic moment in a ferromagnet can be calculated with Eqn. 2.2.12 – the Landau-Lifshitz-Gilbert equation. Both the precession and the damping term depend on the effective field $\boldsymbol{H}_{\text{eff}}$, which is hence a prerequisite to calculate the temporal evolution of the magnetization $\boldsymbol{M}$. In general, the effective field is a tool to describe the forces that act on a magnetic moment. It can be deduced from a change of the system energy U as a result of a changing magnetization $\boldsymbol{M}$ as described by Eqn.

2.2.7. Consequently, an alignment of the magnetization with the effective field always results in a local minimization of the energy of the ferromagnetic system. With respect to the magnetization the system energy has multiple sources. In the semi-classical picture of the micromagnetic model the main contributions to the system energy can be of classical and quantum mechanical origin. While the anisotropy energy and the exchange energy are based on quantum mechanical effects, the demagnetization energy and the Zeeman energy can be described classically. In the following the different energy contributions and their corresponding effective fields are discussed within the context of micromagnetism.

2.3.1 Anisotropy Energy

Some magnetic materials exhibit an intrinsic characteristic that results in a preferred orientation of the magnetic moments. The so-called anisotropy depends on the crystalline structure of the ferromagnet and is caused by an inhomogeneous electron-density distribution in the material. As a consequence it is energetically favorable for the magnetic moments to align in parallel with certain axes referred to as easy axes. In dependence on its lattice structure a material comprises one or more easy axes.

Although the anisotropy energy is a consequence of the quantum mechanical spin-orbit interaction its description in micromagnetism follows a phenomenological approach. It turns out that the easy axes have no distinguished direction meaning that a parallel alignment of the magnetization is just as energetically favorable as an antiparallel alignment. Thus if the anisotropy energy is expressed as orders of the scalar product between a magnetic moment and the easy axis only even orders are considered to account for the symmetric characteristic.

Uniaxial Anisotropy

The hexagonal-closest-package structure of e.g. cobalt causes a single easy axis resulting in the so-called uniaxial anisotropy. If the axis is for simplicity assumed to be parallel to the z-direction the anisotropy energy can be calculated as

$$\begin{aligned} E_\mathrm{K} &= -\int_V \left[K_1 \left(\frac{\boldsymbol{M} \cdot \boldsymbol{e}_\mathrm{z}}{M_\mathrm{s}} \right)^2 + K_2 \left(\frac{\boldsymbol{M} \cdot \boldsymbol{e}_\mathrm{z}}{M_\mathrm{s}} \right)^4 \right] \mathrm{d}\boldsymbol{r} \\ &= \int_V \left[K_1' \sin^2\theta + K_2' \sin^4\theta \right] \mathrm{d}\boldsymbol{r} \end{aligned} \tag{2.3.1}$$

where K_1 and K_2 are material constants called anisotropy constants and θ is the angle between the magnetization $\boldsymbol{M}$ and the anisotropy easy axis $\boldsymbol{e}_\mathrm{z}$. Constant terms that contribute to the anisotropy energy E_k and higher orders of the scalar product are neglected.

Thin magnetic films can consist of materials or material systems with an easy axis that is perpendicular to the film plane. For positive anisotropy constants $K_1 > 0$ and $K_2 > 0$ the magnetization then points along the easy axis and thus out-of-plane. This characteristic property of a magnetic film is referred to as perpendicular magnetic anisotropy (PMA). Besides materials with an hcp-lattice thin films that are composed of multilayers with alternating materials can exhibit perpendicular magnetic anisotropy as well. Correspondingly negative anisotropy constants $K_1 < 0$ and $K_2 < 0$ result in an in-plane orientation of the magnetization. For a ratio $0 > K_1/K_2 > -2$ of the anisotropy constants where $K_1 < 0$ the magnetization relaxes under a certain angle with the easy axis resulting in a so-called canted phase [55]. Nevertheless, in many applications and analytical calculations only the lowest order of anisotropy is considered. Thus the second order anisotropy constant is $K_2 = 0$ which results in $K_1 = K_1'$. The corresponding uniaxial anisotropy field is given by

$$\boldsymbol{H}_\mathrm{K} = -\frac{1}{\mu_0}\frac{\delta E_\mathrm{K}}{\delta \boldsymbol{M}} = \frac{2K_1}{\mu_0 M_\mathrm{s}^2}\begin{pmatrix}0\\0\\M_\mathrm{z}\end{pmatrix} + \frac{4K_2}{\mu_0 M_\mathrm{s}^4}\begin{pmatrix}0\\0\\M_\mathrm{z}^3\end{pmatrix}. \tag{2.3.2}$$

Cubic Anisotropy

The more complex cubic anisotropy is a result of the body-centered-cubic structure of e.g. iron or the face-centered-cubic structure of e.g. nickel that both exhibit a cubic symmetry. Such materials comprise three easy axes that are pairwise orthogonal. Assuming the cubic anisotropy energy to be a function of the three magnetic components M_x, M_y, and M_z it can be calculated by a series expansion along the easy axes. Again, only even orders are considered. Terms that are not invariant under a permutation of the magnetic components are also not taken into account. The resulting cubic anisotropy energy reads

$$E_\mathrm{CK} = \int_V \left(K_\mathrm{C1}\frac{M_\mathrm{y}^2 M_\mathrm{z}^2 + M_\mathrm{x}^2 M_\mathrm{z}^2 + M_\mathrm{x}^2 M_\mathrm{y}^2}{M_\mathrm{s}^4} + K_\mathrm{C2}\frac{M_\mathrm{x}^2 M_\mathrm{y}^2 M_\mathrm{z}^2}{M_\mathrm{s}^6} \right) \mathrm{d}\boldsymbol{r} \tag{2.3.3}$$

with the corresponding cubic anisotropy field

$$\boldsymbol{H}_\mathrm{CK} = -\frac{1}{\mu_0}\frac{\delta E_\mathrm{CK}}{\delta \boldsymbol{M}} = -\frac{2K_\mathrm{C1}}{\mu_0 M_\mathrm{s}^4}\begin{pmatrix}M_\mathrm{x}M_\mathrm{y}^2 + M_\mathrm{x}M_\mathrm{z}^2\\ M_\mathrm{x}^2 M_\mathrm{y} + M_\mathrm{y}M_\mathrm{z}^2\\ M_\mathrm{x}^2 M_\mathrm{z} + M_\mathrm{y}^2 M_\mathrm{z}\end{pmatrix} - \frac{4K_\mathrm{C2}}{\mu_0 M_\mathrm{s}^6}\begin{pmatrix}M_\mathrm{x}M_\mathrm{y}^2 M_\mathrm{z}^2\\ M_\mathrm{x}^2 M_\mathrm{y} M_\mathrm{z}^2\\ M_\mathrm{x}^2 M_\mathrm{y}^2 M_\mathrm{z}\end{pmatrix}. \tag{2.3.4}$$

Despite the phenomenological description the resulting anisotropy energies are very accurate in comparison with experiments [56, 57]. Throughout this thesis the uniaxial anisotropy will be mainly used with the lowest order term.

2.3.2 Demagnetization Energy

Each elementary magnet in a ferromagnetic sample can be also described as a magnetic dipole that generates a magnetic field referred to as stray field. This field is felt by other magnetic moments and the arising interaction can be modeled by a classical long range dipole-dipole interaction. The possible resulting energy contribution due to a non-parallel alignment of the magnetic moments within a ferromagnet with the stray field is thus caused by the magnetization itself and referred to as demagnetization energy, stray-field energy, or magnetostatic energy.

To calculate the demagnetization energy Maxwell's equations from the classical electromagnetic theory are employed. In the absence of a current $\boldsymbol{j}$ a magnetic field $\boldsymbol{H}$ and the magnetic flux density $\boldsymbol{B}$ satisfy the conditions

$$\nabla \times \boldsymbol{H} = 0 \tag{2.3.5}$$

$$\nabla \cdot \boldsymbol{B} = 0. \tag{2.3.6}$$

Since Eqn. 2.3.5 – also known as Ampère's law – yields that the magnetic field $\boldsymbol{H}$ is conservative and can be expressed by the gradient of a scalar potential:

$$\boldsymbol{H} = -\nabla \Phi_{\mathrm{M}}. \tag{2.3.7}$$

Equation 2.3.5 is the magnetic analogon to Gauß's law and it ensues that there are no magnetic monopoles. The magnetic flux density $\boldsymbol{B}$ is connected with the magnetic field $\boldsymbol{H}$ via the magnetization $\boldsymbol{M}$

$$\boldsymbol{B} = \mu_0 \left(\boldsymbol{H} + \boldsymbol{M}\right). \tag{2.3.8}$$

Combining Eqns. 2.3.6, 2.3.7, and 2.3.8 and applying the divergence provides a Poisson equation that is satisfied by the scalar potential

$$\Delta \Phi_{\mathrm{M}} = -\nabla \cdot \boldsymbol{H} = \nabla \cdot \boldsymbol{M}. \tag{2.3.9}$$

Assuming the boundary condition that the magnetic field vanishes at infinity the Poisson equation 2.3.9 is solved by the magnetic potential (cf. e.g. [58])

$$\Phi_{\mathrm{M}}(\boldsymbol{r}) = -\frac{1}{4\pi} \int_{\mathrm{V}} \frac{\nabla' \cdot \boldsymbol{M}(\boldsymbol{r}')}{|\boldsymbol{r} - \boldsymbol{r}'|} \, \mathrm{d}\boldsymbol{r}' + \frac{1}{4\pi} \int_{\mathrm{A}} \frac{\boldsymbol{M}(\boldsymbol{r}') \cdot \boldsymbol{n}}{|\boldsymbol{r} - \boldsymbol{r}'|} \, \mathrm{d}\boldsymbol{a}' \tag{2.3.10}$$

where V is the volume of a magnetic sample and A is its surface. Furthermore, $\mathrm{d}\boldsymbol{a}'$ denotes an undirected infinitesimal surface element and $\boldsymbol{n}$ is the unit normal vector of the surface which is pointing out of the sample. The magnetic potential Φ_{M} is hence built up of two terms. The first term is a volume contribution due to a diverging magnetization, which is why the expression $\rho = -\nabla \cdot \boldsymbol{M}$ is identified with magnetic volume

charges. Consequently the second term is a surface contribution caused by magnetic moments pointing out of the sample which are identified with surface charges expressed by $\sigma = \boldsymbol{M} \cdot \boldsymbol{n}$. The surface contribution here accounts for the boundary condition. Equation 2.3.10 can be rewritten with the divergence theorem to an easier expression

$$\Phi_{\mathrm{M}}(\boldsymbol{r}) = \frac{1}{4\pi} \int_{\mathrm{V}} \boldsymbol{M}(\boldsymbol{r}') \cdot \nabla' \frac{1}{|\boldsymbol{r} - \boldsymbol{r}'|} \tag{2.3.11}$$

According to Eqn. 2.3.7 the demagnetization field at a point $\boldsymbol{r}$ is generated by the magnetic dipoles in a volume V and hence calculated by

$$\boldsymbol{H}_{\mathrm{demag}} = -\nabla \Phi_{\mathrm{M}}(\boldsymbol{r}) = \int_V \widetilde{\boldsymbol{N}}(\boldsymbol{r} - \boldsymbol{r}') \cdot \boldsymbol{M}(\boldsymbol{r}') \, \mathrm{d}\boldsymbol{r}' \tag{2.3.12}$$

where the so-called demagnetization tensor $\widetilde{\boldsymbol{N}}$, which is a 3×3 matrix, determines the strength of the dipole-dipole interaction of magnetic moments. Its components are given by

$$\widetilde{N}_{\mathrm{ij}}(\boldsymbol{r} - \boldsymbol{r}') = -\frac{1}{4\pi} \nabla_{\mathrm{i}} \nabla'_{\mathrm{j}} \frac{1}{|\boldsymbol{r} - \boldsymbol{r}'|} \tag{2.3.13}$$

where the operator ∇_{i} denotes the gradient in the i-th direction. The demagnetization energy in a ferromagnetic material is now given by

$$E_{\mathrm{demag}} = -\frac{\mu_0}{2} \int_V \boldsymbol{M} \cdot \boldsymbol{H}_{\mathrm{demag}} \, \mathrm{d}\boldsymbol{r} \tag{2.3.14}$$

$$= -\frac{\mu_0}{2} \iint_V \boldsymbol{M}(\boldsymbol{r}) \cdot \widetilde{\boldsymbol{N}}(\boldsymbol{r} - \boldsymbol{r}') \cdot \boldsymbol{M}(\boldsymbol{r}') \, \mathrm{d}\boldsymbol{r} \, \mathrm{d}\boldsymbol{r}' \tag{2.3.15}$$

where the factor $1/2$ accounts for the fact that the demagnetization energy is a self energy since the demagnetization field is generated by the magnetization itself. The double integration over space results in a doubled counting of each dipole-dipole interaction of the magnetic moments and has to be corrected.

Shape Anisotropy

Very thin magnetic structures, although considered three-dimensional in micromagnetic simulations, are often described as infinitely thin magnetic films in analytical calculations. This allows to avoid the very complex calculation of the demagnetization tensor $\widetilde{\boldsymbol{N}}$, instead the following approximation is used. If a uniform magnetization is assumed, the demagnetization field can be written as

$$\boldsymbol{H}_{\mathrm{demag}} = -\int_V \widetilde{\boldsymbol{N}}(\boldsymbol{r} - \boldsymbol{r}') \, \mathrm{d}\boldsymbol{r}' \cdot \boldsymbol{M}' \tag{2.3.16}$$

For a magnetic film in the xy-plane the integration over the demagnetization tensor yields a matrix with only one non-zero entry which is $\widetilde{N}_{\mathrm{zz}} = 1$ and zero elsewhere. The

resulting field is $\boldsymbol{H}_{\text{demag}} = (0, 0, -M_z)$ and thus it scales with the out-of-plane component of the magnetization. Thereby it is directed along the z-axis and acting against the out-of-plane magnetization hence favoring an in-plane orientation of the magnetic moments. The demagnetization energy (see Eqn. 2.3.14) can now be written as

$$E_{\text{demag}} = \frac{\mu_0}{2} \int_V M_z^2 \, \mathrm{d}\boldsymbol{r} \tag{2.3.17}$$

$$= -\frac{\mu_0 M_s^2}{2} \int_V \sin^2\theta \, \mathrm{d}\boldsymbol{r} + C \tag{2.3.18}$$

where θ is the angle between a magnetic moment and the z-axis and C is a constant energy term that can be omitted since it does not affect the magnetization dynamics. In this special case the demagnetization energy corresponds to a uniaxial anisotropy energy and is hence referred to as shape anisotropy.

Effective Anisotropy

The shape anisotropy has a uniaxial character. Thus in thin magnetic films that comprise a perpendicular magnetic anisotropy both anisotropies can be combined to an effective anisotropy. Although both depend on the out-of-plane component of the magnetization, they have oppositional impacts on the magnetic moments. While the uniaxial anisotropy of a material with PMA favors an out-of-plane orientation of the magnetization the shape anisotropy results in an in-plane alignment. In the case of a simple low order uniaxial anisotropy the energy thus reads

$$E_{\text{k}_{\text{eff}}} = \left(K_1 - \frac{\mu_0 M_s^2}{2} \right) \int_V \sin^2\theta \, \mathrm{d}\boldsymbol{r} \tag{2.3.19}$$

$$= K_{\text{eff}} \int_V \sin^2\theta \, \mathrm{d}\boldsymbol{r} \tag{2.3.20}$$

where K_{eff} is called the effective anisotropy constant. Strictly speaking, the use of the simple effective anisotropy is only valid for uniform magnetized and infinitely thin magnetic films. Nevertheless, this approach is widely-used to describe magnetization properties in nanowires and other thin structures and yields good results.

2.3.3 Exchange Energy

Although magnetic dipoles in a solid-state body would favor an anti-parallel alignment due to the stray-field energy, in ferromagnets there are obviously areas of uniform magnetization. This behavior is a consequence of a quantum mechanical effect called exchange interaction. Despite the arising stray-field energy, a parallel alignment of adjacent magnetic moments is energetically much more favorable. Consequently, materials with a weak exchange interaction like dia- and paramagnets are dominated by

the demagnetization energy and show a non-uniform magnetization pattern.

For the understanding of the exchange interaction – which basically describes the energy difference of a parallel or non-parallel alignment of two adjacent spins – a crucial point is the behavior of the corresponding wave functions. If a system with two electrons that have overlapping wave functions is assumed, the overall wave function has to be asymmetric due to the fermionic character of the particles. Now, the energy of the system is mainly determined by the spin wave function. A parallel orientation of the electron spins features a symmetric spin wave function resulting in an anti-symmetric orbital wave function. Since an anti-symmetric orbital wave function is characterized by a larger mean distance of the electrons a parallel alignment reduces the Coulomb energy. On the other hand, this implies the electrons to be in different orbital states due to the Pauli principle that increases the energy. Nevertheless, if the reduction of the Coulomb energy overcompensates the increased energy due to an excited orbital state the spins align in parallel. Transferring this simple consideration to many particles means the material is ferromagnetic. Obviously, this is only true for very few elements of the transition metals – namely iron, cobalt, and nickel.

In 1926 P. A. M. Dirac and W. Heisenberg already described the exchange interaction of neighboring spins [59, 60] and in 1928 Heisenberg related magnetism with the exchange phenomenon [61]. Thus the Heisenberg picture is used in the following to describe the exchange energy of two adjacent moments in the context of micromagnetism. The exchange energy density of two neighboring spins $\boldsymbol{S}_\mathrm{i}$ and $\boldsymbol{S}_\mathrm{j}$ is given by

$$U_{\mathrm{ex}_{\mathrm{i,j}}} = -J_{\mathrm{i,j}}\, \boldsymbol{S}_\mathrm{i} \cdot \boldsymbol{S}_\mathrm{j} \tag{2.3.21}$$

$$= -J_{\mathrm{i,j}} S^2 \cos\phi_{\mathrm{i,j}}, \tag{2.3.22}$$

where $J_{\mathrm{i,j}}$ is the exchange integral which determines the strength of the interaction and the resulting spin alignment, $\phi_{\mathrm{i,j}}$ is the angle between the spins, and $S = |\boldsymbol{S}_\mathbf{i}| = |\boldsymbol{S}_\mathbf{j}|$ is the spin magnitude. Since the exchange interaction stems from overlapping wave functions it acts only on short ranges. Thus usually only the interaction between nearest neighbors contributes to the exchange energy. Summing over all nearest neighbors yields the exchange energy density due to a single spin

$$U_\mathrm{ex} = -S^2 \sum_\mathrm{i} J_\mathrm{i} \cos\phi_\mathrm{i}, \tag{2.3.23}$$

where *i* denotes the nearest neighbors and ϕ_i is the angle between a spin and its neighboring spin. In the model of micromagnetism the spins are now connected with magnetic moments $\boldsymbol{M}(\boldsymbol{r})$. With the law of cosine two adjacent magnetic moments at

$\boldsymbol{M}(\boldsymbol{r})$ and $\boldsymbol{M}(\boldsymbol{r}+\boldsymbol{r}_\mathrm{i})$ fulfill the relation

$$\cos\phi_\mathrm{i} = 1 - \frac{1}{2M_\mathrm{s}^2}\left[\boldsymbol{M}(\boldsymbol{r}+\boldsymbol{r}_\mathrm{i}) - \boldsymbol{M}(\boldsymbol{r})\right]^2 \tag{2.3.24}$$

where $\boldsymbol{r}_\mathrm{i}$ is the distance between a magnetic moment and its nearest neighbors. Since one crucial assumption in micromagnetism is an almost parallel alignment of the magnetization within the range of the exchange interaction an expansion of the magnetization in a Taylor series is feasible. The magnetic moment at the position of the nearest neighbors can hence be written as

$$\boldsymbol{M}(\boldsymbol{r}+\boldsymbol{r}_\mathrm{i}) \approx \boldsymbol{M}(\boldsymbol{r}) + (\boldsymbol{r}_\mathrm{i}\cdot\boldsymbol{\nabla})\,\boldsymbol{M}(\boldsymbol{r}). \tag{2.3.25}$$

Thus the exchange energy density of a ferromagnetic body can be written as

$$U_\mathrm{ex} = \frac{S^2}{2M_\mathrm{s}^2}\sum_\mathrm{i} J_\mathrm{i}\left[(\boldsymbol{r}_\mathrm{i}\cdot\boldsymbol{\nabla})\,\boldsymbol{M}(\boldsymbol{r})\right]^2 + C. \tag{2.3.26}$$

The number and the positions of the nearest neighbors vary in dependence on the lattice structure the spins are arranged in. However, for a cubic, a face-centered, and a body-centered lattice the summation results in the same exchange energy. Furthermore in isotropic materials the exchange integral does not depend on the nearest neighbor. If a is the lattice constant it can thus be written

$$U_\mathrm{ex} = \frac{JS^2a^2}{M_\mathrm{s}^2}\left(\boldsymbol{\nabla}\boldsymbol{M}\right)^2. \tag{2.3.27}$$

Assuming a spin density c/a^3 – where c is the number of spins per unit cell and depends on the lattice structure – the total exchange energy of a ferromagnetic body is calculated by

$$E_\mathrm{ex} = \frac{JS^2c}{aM_\mathrm{s}^2}\int_V \left(\boldsymbol{\nabla}\boldsymbol{M}\right)^2 \,\mathrm{d}\boldsymbol{r} \tag{2.3.28}$$

$$= -\frac{A}{M_\mathrm{s}^2}\int_V \boldsymbol{M}\cdot\boldsymbol{\Delta}\boldsymbol{M}\,\mathrm{d}\boldsymbol{r} \tag{2.3.29}$$

where the identity $2(\boldsymbol{\nabla}\boldsymbol{M})^2 = \boldsymbol{\Delta}(\boldsymbol{M}^2) - 2\boldsymbol{M}\cdot\boldsymbol{\Delta}\boldsymbol{M}$ has been used and constant terms are omitted. $A = JS^2c/a$ is the so-called exchange constant and on a microscopic scale it can be only determined by experiment. If $A > 0$ the magnetic moments align in parallel and the material is ferromagnetic, whereas $A < 0$ results in an antiferromagnetic behavior. The effective field due to the exchange interaction can consequently be calculated by

$$\boldsymbol{H}_\mathrm{ex} = -\frac{1}{\mu_0}\frac{\delta E_\mathrm{ex}}{\delta\boldsymbol{M}} = \frac{2A}{\mu_0 M_\mathrm{s}^2}\boldsymbol{\Delta}\boldsymbol{M} \tag{2.3.30}$$

and thus the misalignment of adjacent magnetic moments generates an effective field to parallelize the magnetization. Although the magnetic moments that are connected with the electron spins are not localized in a ferromagnetic sample, the Heisenberg picture is based on the interaction of spins at fixed positions. Nevertheless, in the micromagnetic model that describes magnetization as a continuous vector field the description of the exchange interaction with the Heisenberg picture is a reasonable approximation.

2.3.4 Zeeman Energy

Besides the intrinsic energies of a ferromagnet the overall energy can be drastically manipulated by an external contribution – the Zeeman energy. It is a result of the Zeeman field $\boldsymbol{H}_{\text{zee}}$ and is given by

$$E_{\text{zee}} = -\mu_0 \int_V \boldsymbol{M} \cdot \boldsymbol{H}_{\text{zee}} \, \mathrm{d}\boldsymbol{r}. \tag{2.3.31}$$

As a consequence from the Landau-Lifshitz-Gilbert equation the magnetization aligns in parallel with the Zeeman field in order to minimize the energy of the system. Thus the Zeeman field provides the possibility to manipulate the magnetization of a ferromagnetic body from the outside. It is hence used to switch the magnetization or to drive domain walls.

2.4 Applicability of the Micromagnetic Model

The micromagnetic model allows for the description of the temporal evolution of a continuous magnetization using the Landau-Lifshitz-Gilbert equation. Various internal and external influences can be taken into account either by additional contributions to the effective field $\boldsymbol{H}_{\text{eff}}$ (see Sec. 2.3) or by extensions to the Landau-Lifshitz-Gilbert equation, e.g. the extension due to spin currents in Sec. 2.2.4. However, when a model in physics is used it is important not to discuss only possibilities, but limitations as well. Since the model, as any model, is an adaption of nature it does not take all effects into account. To successfully apply a theoretical model to a specific physical problem the basic parameters and conditions have to match. Furthermore, a profound knowledge about simplifications and assumptions and their underlying physical principles is necessary in order to make a statement about the validity and accuracy of obtained results. Therefore, in this section several limitations that have to be kept in mind if the micromagnetic model is used are discussed and a few effects that can further extend the model and the Landau-Lifshitz-Gilbert equation are briefly introduced. Furthermore, the application of the micromagnetic model in computational science, i.e. simulations, is presented.

2.4.1 Temperature

An omnipresent phenomenon that has to be dealt with in physics is temperature. Except in very complex low temperature experiments it affects most physical properties including magnetism. In general, temperature can be considered as a stochastic perturbation on the atomic scale. For magnetic moments this results in an continuous arbitrary deflection from the initial orientation. In the sense of classical magnetism averaging over a certain space and time then results in a reduced saturation magnetization. The reduction increases with higher temperature and at the Curie temperature the magnetic moments are disordered and ferromagnetism is abolished. Nevertheless, this classical approach does not account for stochastic effects as thermically activated switching or depinning. Thus a more common approach to include temperature in the micromagnetic model is made by adding a fluctuating term to the effective field as has been first done by W. F. Brown in 1963 [62, 63]. The Landau-Lifshitz-Gilbert equation is then replaced by a Langevin equation to account for the stochastic nature of temperature. However, Brown's approach neglects the temperature dependence of the saturation magnetization and is hence only reasonable for low temperature cases. A third approach that considers a local change of the saturation magnetization as well as the stochastic effective field is given by the Landau-Lifshitz-Bloch equation [64].

2.4.2 Bloch Points

Another phenomenon that was first described by E. Feldtkeller are so-called Bloch points [65]. At these singularities that occur in certain magnetic configurations the magnetization vanishes and in the volume around the Bloch points the magnetization is changing rapidly. Thus two central assumptions of the micromagnetic model – a homogeneous magnetization and a slowly varying magnetization – are violated and the micromagnetic model hence fails to describe Bloch points accurately. This is especially important if switching is investigated since Bloch points are often involved in magnetization reversal processes [66].

2.4.3 Interface, Exchange, and Multilayer Effects

Experiments with magnetic materials often involve not only homogeneous samples, but sometimes very complex multilayered structures that give rise to many interfaces that can affect the magnetization. Even the interface between a sample and air can play a crucial role in magnetization dynamics. Since the micromagnetic model is derived on the basis of a homogeneous material in vacuum none of the following effects are taken into account.

Dzyaloshinskii-Moriya Interaction

The Dzyaloshinskii-Moriya-Interaction (DMI) [67, 68] is an antisymmetric exchange interaction that favors a certain sense of rotation of a spatially varying magnetization at an interface between different materials. Its impact at some interfaces is found to be stronger than the normal exchange interaction [69].

Spin Hall Effect

Especially in multilayers the spin Hall effect (SHE) is present [70]. If the layers of a stack exhibit unequal thicknesses this can result in a net spin current into a magnetic layer which can then be used to manipulate magnetic moments [71].

Orange-Peel Coupling

Another multilayer effect is the so-called orange-peel coupling first described by Néel [72]. If two magnetic layers that are separated by a non-magnetic layer have rough surfaces, the magnetic moments in both layers couple and want to align in parallel. In magnetic tunnel junction devices the coupling stabilizes the free layer and is hence an undesired effect [73].

Rudermann-Kittel-Kasuya-Yosida Interaction

An additional indirect exchange coupling that is mediated via conduction electrons is the Rudermann-Kittel-Kasuya-Yosida interaction [74–76]. Based on this effect multilayers with certain materials can be designed to couple ferromagnetically or antiferromagnetically – dependent on the layer thicknesses [77].

Surface Anisotropy

The anisotropy energy introduced earlier refers to a volume material, but actually the anisotropy has two contributions – a volume and a surface contribution [78]. This is particularly important if thin films are described or if multilayers are discussed, since the surface anisotropy is present at the interface between different materials as well. Hence the perpendicular magnetic anisotropy in multilayer structures is attributed to the surface anisotropy [79].

2.4.4 Applications

Although the description of magnetism on the basis of the micromagnetic model is limited and does not include the effects and phenomena mentioned above, it is a widely used model to calculate the magnetization and its dynamics in microstructures. In some special simplified cases it is possible to solve the effective field and the Landau-Lifshitz-Gilbert equation analytically, but in general this is the exception. However, the derived equations can be solved numerically with the aid of computers and hence today a main application of the micromagnetic model are micromagnetic simulations.

Simulations are a very powerful tool to reproduce experiments as well as analytical calculations and although they are based on a simplified model, extensions can be easily applied. In the case of micromagnetism this has been recently at least done for the spin Hall effect [71,80] and the Dzyaloshinskii-Moriya interaction [81,82]. Furthermore, simulations based on the micromagnetic model allow for the investigation of processes that involve Bloch points since these singularities become negligible in simulations [83]. In the next chapter micromagnetic simulations and the material system that is mainly investigated throughout this thesis are introduced in detail.

Chapter 3

Material System and Simulations

In the course of this thesis the main focus is the investigation of domain-wall dynamics in ferromagnetic nanowires by means of micromagnetic simulations. Nanowires form the basis of the famous concept for a new data-storage device known as racetrack memory [1,2] and thus gained a lot of interest in the recent years. Especially nanowires with perpendicular magnetic anisotropy are promising to realize the device since in contrast to soft magnetic nanowires much lower current densities are needed to drive a domain wall through them and much higher storage densities can be achieved [84,85].

A powerful tool to investigate micromagnetic structures are simulations based on the micromagnetic model. The enormous gain in computer power during the last decades enables to solve the underlying equations (see Chap. 2) for a constantly increasing complexity of the investigated system. Without much effort it is possible to undertake systematic studies of e.g. the magnetization configuration or the magnetization dynamics. The influence of several material parameters like the saturation magnetization M_s or the damping coefficient α as well as the geometry and strength of local modifications of the material parameters on these characteristics can be investigated without the necessity to prepare a new sample each time the parameters are changed. Thus simulations are not only time-saving and cost-efficient but also much easier to employ since the preparation of samples is a very error-prone process that requires a lot of expertise. However, simulations on the other hand usually describe ideal cases that are based on a physical model which only describes a limited part of reality (see Sec. 2.4) and include several simplifications. A profound knowledge of the underlying model, awareness of the applied simplifications, and a continuous comparison with experiments is necessary to assure the correctness of simulations. Assuming this, simulations can also be used to verify analytical calculations as well, since while calculations are usually limited to edge cases simulations take much more effects into account.

The following chapter deals with a basic description of the investigated material system and how it is used in simulations as well as experiments. The general functional

principle of simulations is discussed and necessary simplifications are explained.

3.1 Nanowires and Perpendicular Magnetic Anisotropy

In this section the investigated system is described in detail. Besides the general geometry of nanowires, materials that comprise perpendicular magnetic anisotropy are introduced. Furthermore, the intentional local modification of material parameters is discussed.

3.1.1 Nanowires

In general, a nanowire is a microstructure where one dimension exceeds the two remaining dimensions by orders of magnitude. Two types of nanowires are usually distinguished – the one-dimensional and the two-dimensional nanowire. While the one-dimensional nanowire has a round cross section and is hence rotation-symmetric, the two-dimensional nanowire is a flat structure with rectangular cross section. As the name implies, the diameter and accordingly the thickness of nanowires are in the regime of a few nanometers. As depicted in Figure 3.1 the width is in the order of hundreds of nanometers and the aspect ratio between length, width, and thickness is hence approximately 1000:100:10. Throughout this thesis all considerations are limited to two-dimensional nanowires.

The usual technique to prepare nanowires in experiments is a series of processes. At first a sacrificial layer on a substrate is prepared where the desired geometry of the nanowire is written in with electron-beam lithography. The illuminated parts are removed and subsequently the material for the nanowire is applied to the substrate by sputter deposition. Finally, the sacrificial layer is lifted off including the dispensable material leaving the single nanowire. Since this technique is used in computer industry to produce ICs and CPUs as well, the racetrack memory would be – once realized – appropriate for mass production.

3.1.2 Perpendicular Magnetic Anisotropy

The perpendicular magnetic anisotropy of ferromagnetic nanowires has its origin in an easy axis that is perpendicular to the plane of the nanowire as illustrated in Figure 3.1. The magnetic moments favor a parallel alignment with the easy axis and hence an out-of-plane orientation. However, the demagnetization energy is minimized for an in-plane orientation of the magnetization. The resulting interplay is usually expressed by the dimensionless ratio Q between both energies and in a thin magnetic film it is denoted

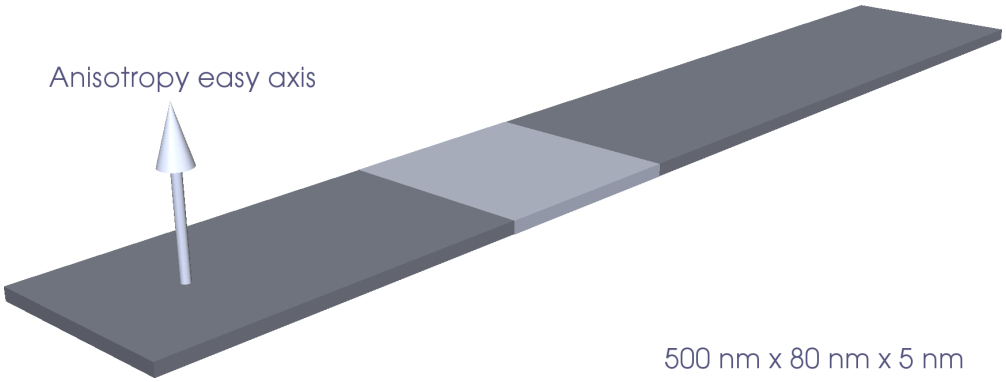

Figure 3.1: Depiction of a nanowire of the size $500 \times 80 \times 5$ nm^3. The anisotropy easy axis illustrates the perpendicular magnetic anisotropy resulting in an out-of-plane orientation of the magnetization. The lighter area indicates modified material parameters.

by

$$Q = \frac{U_\mathrm{K}}{U_\mathrm{demag}} = \frac{2K_1}{\mu_0 M_\mathrm{s}^2}. \tag{3.1.1}$$

For a ratio $Q > 1$ the crystalline anisotropy has a stronger impact on the magnetic moments than the shape anisotropy and thus the magnetization is oriented out-of-plane. For a ratio $Q < 1$ it is energetically favorable to avoid the stray field and the magnetization aligns with the plane of the nanowire. In the case of a thin film the Q-factor is solely determined by the saturation magnetization M_s and the anisotropy constant K_1, but in different geometries as e.g. cubes or spheres the demagnetization energy can be very different and Q can not be calculated that easily.

Multilayer

In general, there are two prominent material systems that are both suited for nanowires and comprise perpendicular magnetic anisotropy – multilayers and certain alloys. A multilayer is a material that consists of stacked alternating layers of usually two different materials, e.g. cobalt and platinum or cobalt and nickel. Although the magnetic materials themselves show a crystalline anisotropy, the idea of stacking several layers is to benefit from the surface anisotropy at the interfaces between the materials (for Co/Pt and Co/Pd multilayer [86–88]) or to benefit from magnetoelastic contributions (Co/Ni multilayer [89, 90]) to enhance the strength of the anisotropy. Furthermore, the composition of two different materials allows for the tailoring of material parameters as the saturation magnetization M_s [91]. To obtain an out-of-plane easy axis the growth direction of the multilayer is important as well. Cobalt, for instance, has an hcp-structure with an easy axis parallel to the c-axis and a nanowire containing cobalt has thus to be grown in the [111]-direction to exhibit a perpendicular magnetic anisotropy.

Alloy

The preparation of multilayers with very clean interfaces between the single layers and without any inclusions or structural defects is very challenging, but essential for the quality of the system properties. A different possibility to prepare nanowires with perpendicular magnetic anisotropy is to use so-called transition-metal rare-earth alloys [92]. A popular representative of such an alloy is Tb/Fe/Co [93]. Although the production of a magnetic layer of this material is unproblematic, the control of its magnetic properties is not and has to be enhanced by underlayers. Furthermore, the alloy is very sensitive to oxidation which results in nucleation and pinning centers [94,95]. Nevertheless, in recent years Tb/Fe/Co is subject to numerous studies concerning current-driven domain wall motion in nanowires with perpendicular magnetic anisotropy [96–98].

3.1.3 Local Modification of the Material Parameters

The result of the preparation process as sketched in Sec. 3.1.1 is usually a nanowire with almost homogeneous material parameters, minor imperfections cause only slight local variations. However, for the purpose of domain-wall creation and pinning a significant local modification of particular parameters is desired (see Secs. 4.2 and 4.4). In the case of perpendicular magnetic anisotropy in multilayered nanowires this parameter is the anisotropy constant K_1. Since it has the largest impact on the magnetic properties and magnetization dynamics of the nanowire even small changes can be sufficient to achieve the desired results. In contrast to this, for in-plane materials as permalloy the modified parameter would be the saturation magnetization M_s.

Ion Irradiation

The most prominent technique to manipulate the anisotropy constant in materials comprising PMA is ion irradiation. Especially nanowires made of multilayers are subject to this procedure that was first reported by C. Chappert et al. [38] and became very popular since then [99]. While Co/Pt nanowires where investigated in the first instance, the technique is also appropriate for the nowadays commonly used Co/Ni nanowires [39]. In both cases the irradiation results in a reduction of the anisotropy constant that can be applied globally by ion irradiation with He^+ ions or locally with a focused beam of Ga^+ ions (see Fig. 3.1). The irradiated ions do not remain in the magnetic layers, but only cause an intermixing of the atoms at the interfaces between the materials and thereby reduce the surface anisotropy and alter magnetoelastic properties. Other effects that influence the magnetization dynamics as surface roughness or defects do not occur, which is an important advantage. In alloys as e.g. permalloy it is also possible to change the magnetic properties, but in this case the ions are implanted which affects

other material parameters as the saturation magnetization M_s [36].

Electric Field

Another possibility to modify the material parameters in nanowires that has recently evolved is the application of an electric field, which is known as the magnetoelectric effect and is described in Refs. [100, 101]. Besides other magnetic properties as the saturation magnetization it is especially possible to alter the anisotropy constant K_1 [102]. Several underlying mechanisms can be identified to be responsible for the changed material parameters, e.g. strain [103], charge trapping [104], and migration of oxygen ions [105]. For the change of the anisotropy in nanowires the application of an electric field over interfaces between a ferromagnet and an oxide is suitable as well [19]. The electric field results in a decreased charge density at the interface in the ferromagnet, which causes a redistribution of electrons between different *d*-orbitals [106]. Since the charge-density distribution in orbitals is the origin of the anisotropy energy, the electric field can be used to decrease or increase the anisotropy constant. The main advantage of this technique is its reversibility meaning that an artificial pinning site due to a local modification of the material parameters can be switched on and off.

3.2 Simulations

As mentioned in the introduction of this chapter, the rapidly evolving computer power enables simulations of more and more complex problems. Since this is not only true for micromagnetism, but for many other scientific subjects, the importance of simulations is steadily growing. Besides the two classical approaches – analytical calculations and experiments – simulations advance to a third coequal possibility to resolve questions in science. However, up to now simulations are still based on theoretical models and the obtained results have to be discussed, bearing in mind the limitations a model usually comes along with (see Sec. 2.4). Nevertheless, micromagnetism is a prominent example how science can benefit from simulations. Since the underlying micromagnetic model is well-established nowadays, it is good practice in publications which concern a related topic to include micromagnetic simulations. This applies to both theoretical and experimental work.

3.2.1 General Functionality and Setup

The micromagnetic model seems to be predestined as basis for simulations. The central equation of the model – the Landau-Lifshitz-Gilbert equation – can be formulated in an explicit form, which means the change $\mathrm{d}\boldsymbol{M}/\mathrm{d}t$ of the magnetization depends on the current state of the system. So once an initial configuration of the magnetization is

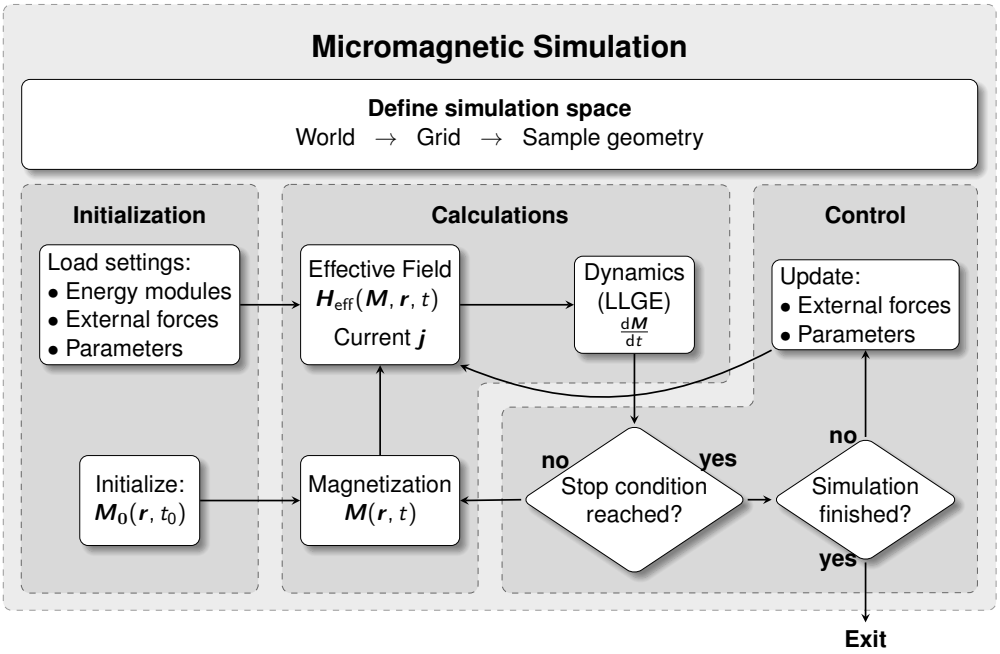

Figure 3.2: Flowchart of a micromagnetic simulation. At first a simulation space including the sample geometry on a certain grid within a world is defined. Then the energy modules, material parameters, and external influences are configured and a initial magnetization is set. Based on the magnetization and the settings the effective field is calculated and subsequently the evolution of the magnetic moments. If no stop condition is fulfilled the changes are applied to the magnetization and the simulation continues. Alternatively the settings can be updated before the simulation proceeds and if it is not ended.

defined, the solution to the equation can be calculated and applied to the initial state. If this is done iteratively the temporal evolution of the magnetic moments in a ferromagnet is reproduced. Since the model provides some exceptional cases that can be solved analytically, each simulator based on the micromagnetic model can be verified by reference calculations [107]. All results that have been obtained in the course of this thesis are based on simulations performed with MicroMagnum – a fast micromagnetic simulator for computations on CPU and GPU [42]. The general steps that are necessary to perform a simulation are discussed in the following.

Initialization

As depicted in the flowchart of Fig. 3.2 the first step of a simulation is usually the definition of a simulation space. Therefor an empty space is discretized by equidistant cells of a certain volume. On the resulting mesh it is then possible to define a sample geometry like a cylinder or a cuboid by assigning cells to the geometry. Each simulation cell holds the information of a magnetic moment $\boldsymbol{M}$ and the settings of the micromagnetic

model as material parameters and external forces. The stored values are the corresponding averages of a sample that are mapped on each cell. To resolve all possible magnetic phenomena the choice of the cell size is crucial. It is mandatory to set the edge length of the cells significantly shorter than the exchange length [108]

$$l_{\mathrm{ex}} = \sqrt{AK^{-1}}. \tag{3.2.1}$$

In in-plane materials without anisotropy, K is defined as $\mu_0 M_{\mathrm{s}}^2/2$ and thus the exchange length is for e.g. permalloy $l_{\mathrm{ex}} \approx 5.7$ nm. For thin films with perpendicular magnetic anisotropy $K = K_{\mathrm{eff}}$ holds and thus the exchange length can reduce to $l_{\mathrm{ex}} \approx 4.8$ nm for typical PMA material systems. Hence a cell size of 2.5×2.5 nm^2 is usually used in the simulations. Before the simulation can be started the energy modules and extensions to the Landau-Lifshitz-Gilbert equation that shall contribute to the effective field $\boldsymbol{H}_{\mathrm{eff}}$ and the magnetization dynamics have to be declared. For instance these are the anisotropy energy and a spin-polarized current, see Secs. 2.2 and 2.3. Furthermore, the initial magnetization and material parameters have to be set.

Calculations

Once the initialization is complete the simulation can be started and the actual calculations are performed. Based on the magnetization $\boldsymbol{M}$ and the considered energy terms an effective field $\boldsymbol{H}_{\mathrm{eff}}$ is calculated for each cell. Subsequently with $\boldsymbol{H}_{\mathrm{eff}}$ and other extensions to the micromagnetic model the Landau-Lifshitz-Gilbert equation is solved to obtain a local evolution of the magnetization $\mathrm{d}\boldsymbol{M}/\mathrm{d}t$. A multiplication with a discrete timestep $\mathrm{d}t$ yields the magnetization change $\mathrm{d}\boldsymbol{M}$, which is then added to the magnetic moment for each cell and an altered magnetization configuration is obtained as new starting point for the calculations. These steps are executed iteratively and in doing so a temporal evolution of the magnetization is simulated. During the simulation the timestep is adapted dynamically to achieve an optimal ratio between simulation speed and accuracy.

Control

To control the simulation, stop conditions can be defined. Usually this is a maximum change of the magnetization $\mathrm{d}\boldsymbol{M}_{\mathrm{max}}/\mathrm{d}t$, other control parameters are e.g. the simulated time or the velocity of a domain wall. If a certain value is underrun the magnetization is – in case of $\mathrm{d}\boldsymbol{M}_{\mathrm{max}}/\mathrm{d}t$ as stop condition – assumed to be relaxed and the calculation stops. If the simulation is not finished the parameters and external forces of the simulation can be updated and the calculation continues. This is an extremely useful feature if a simulation includes external influences, e.g. if a hysteresis is swept.

3.2.2 Simplifications and Assumptions

Unfortunately the computer power has not increased enough yet to perform atomistic simulations of sufficiently large samples. Hence a model is employed that does not include all physical effects and interactions, see Sec. 2.4. Nevertheless, micromagnetic simulations are well-established and can reproduce experimental results with high accuracy. In the following simplifications and assumptions and their impact on the comparability with experiments are discussed.

Temperature

In micromagnetic simulations temperature is usually not taken into account since it increases the complexity of the underlying equations significantly and the way how to accurately model temperature in micromagnetism is still under investigation [109, 110]. However, most experiments concerning magnetization dynamics in thin films are conducted at very low temperatures as well and to these the results obtained by simulations are fully comparable.

Effective Material Parameters

Although the material systems that are used in experiments can be very complex (e.g. multilayers) for the simulations it is basically only important which characteristics they have and which material parameters can be measured. Provided that no interactions are investigated that are derived directly from the inner structure of a sample, it is common in simulations of thin films to consider a homogeneous material with effective parameters [16, 111, 112]. The reason is that in thin films, where the thickness is in the range of the exchange length, the magnetic moments react homogeneously across the height of the nanowire, since they are strongly coupled – even in multilayer materials. Thus the inner structure has no influence on the magnetization dynamics. Furthermore, the actual origin of effects as the perpendicular magnetic anisotropy does not affect the simulation of magnetization dynamics as long as the effective parameters are adopted correctly from experiment. Under these assumptions it is possible to compare the results of micromagnetic simulations based on a homogeneous thin film comprising effective material parameters with the results of an experiment.

Two-dimensional Simulations

Due to the homogeneous reaction of magnetic moments in thin films it is sufficient to use only one cell in height with effective parameters. Since the typical thickness of a nanowire is in the range of the exchange length the deviation from an experiment

due to this approximation is negligible. Two-dimensional in this context means that the simulated mesh has only one cell in height, but the calculations of the simulation, especially the demagnetization field, are carried out in three dimensions. Thus the thickness of the nanowire still determines the influence of the demagnetization energy and thereby the nature of the shape anisotropy. To obtain results that are comparable with analytical calculations the thickness has to be small compared to the length and width of the nanowire to ensure the demagnetization tensor $\widetilde{\boldsymbol{N}}$ reduces to $\widetilde{N}_{zz} = 1$ (see Sec. 2.3.2) which usually holds true for nanowires.

Ideal System

Another simplification in micromagnetic simulations is the perfection of the described system. Real samples usually comprise imperfections, e.g. defects in the crystalline structure, grains with slightly different anisotropy easy axes, and rough edges. These imperfections result from a challenging preparation process and are hard to avoid. They can act as pinning and nucleation sites and can hence cause unexpected behavior of the magnetization. As a result especially the switching fields of experimental magnetic samples in comparison with theoretical calculations reveal deviations. These discrepancy has been formulated as Brown's paradox [13, 113–117]. However, since the imperfections are spatially limited they usually do not affect greater magnetic processes. Moreover, if the underlying mechanisms of the imperfections are understood, artificial modifications can be introduced into simulations and analytical calculations in order to manipulate the magnetization dynamics in a desired way (see Refs. [17, 18, 118]). Insights gained by micromagnetic simulations that take imperfections into account are thus in general qualitatively fully comparable to experimental findings, see especially Sec. 5.1.3.

Chapter 4

Domain Walls

A general principle in physics states that a system aspires to a configuration of minimal total energy. In the sense of magnetism this means the magnetic moments arrange in order to minimize the energy and align in parallel with the effective field (see Sec. 2.3). In extended thin films the demagnetization field is locally high enough to switch the orientation of the magnetization, which results in the formation of so-called magnetic domains. Domains are regions where the magnetic moments are aligned in parallel and in adjacent domains the orientation of the magnetization differs. Between the domains a boundary referred to as domain wall is formed where the magnetization performs a smooth transition of its orientation. Although this transition increases the anisotropy and exchange energy in thin films with perpendicular magnetic anisotropy the formation of domains significantly reduces the demagnetization energy, which is the dominant energy contribution in this geometry. In large samples the domain structure is remindful of a complex maze.

Nanowires on the other hand are too small to comprise a complicated domain structure meaning that a monodomain state is energetically stable. However, for the concept of the racetrack memory the presence of several domains and therewith domain walls is inevitable. Usually they are injected by a local switching of the magnetization by external influences as fields or currents. A state with several domains is a local minimum of the energy and hence stable as well, the domain walls do not move or vanish. Moreover, they can now be manipulated and driven through the nanowire by external forces.

In the following the predominant types of domain walls that occur in nanowires with perpendicular magnetic anisotropy are discussed. An approach how to locally switch the magnetization to inject domain walls and how to calculate the corresponding switching fields is presented. Furthermore, an analytical model to describe the movement of a domain wall in nanowires is introduced and finally a mechanism how to control the movement by means of pinning is demonstrated.

4.1 Domain-wall Charateristics

In nanowires with perpendicular magnetic anisotropy the magnetic moments in domains are oriented either up or down, thus the magnetization rotates from one domain to another by 180°. The predominant domain-wall type in a nanowire with relaxed magnetic configuration is the Bloch wall, although in very narrow nanowires Néel walls occur as well. Moreover, under external influences the structure of a domain wall can change between a Bloch and a Néel configuration. The analytical description of both domain-wall types is almost the same, but especially in nanowires the stray fields that result from the magnetic charges due to the domain walls are different, see Sec. 4.4.2.

In this section the Bloch wall and therewith the Néel wall is introduced in detail since they are important for further calculations. The wall profile is calculated and its width is defined.

4.1.1 Bloch Wall and Néel Wall

A basic type of domain wall in ferromagnets is the Bloch wall. It is characterized by the rotation of the magnetic moments by 180° parallel to the wall plane. This means the azimuthal angle φ, which is defined as the angle between the magnetic moment – projected on the nanowire plane – and the plane of the domain wall is $\varphi = 0, \pm\pi$ during rotation of the magnetization, see Fig. 4.1(a). The corresponding path of the magnetic moments in a Bloch wall is depicted in Fig. 4.1(b). Contrary to the Bloch wall, the Néel wall comprises an azimuthal angle of $\varphi = \pm\pi/2$ and thus the magnetization rotates perpendicular to the wall plane. A Bloch wall and a Néel wall in a nanowire with perpendicular magnetic anisotropy are shown in Figs. 4.2(a) and 4.2(b), respectively. From an energetically point of view and neglecting the stray field, the analytical description of both domain walls is identical and will be shown in the following.

4.1.2 Energy Density

The main energy contributions to a domain wall are the exchange energy and the anisotropy energy, because during the rotation within the wall adjacent magnetic moments are not aligned in parallel and they are not oriented along the easy axis. Furthermore, shape anisotropy has to be taken into account since the domain walls are described in thin magnetic films. Assuming the domain wall to be homogeneous in the *yz*-plane and the azimuthal angle φ to be constant during rotation, the energy density per unit area of a Bloch wall can be calculated by an integration over the energy contributions along a path through the wall. The following calculations are adopted from

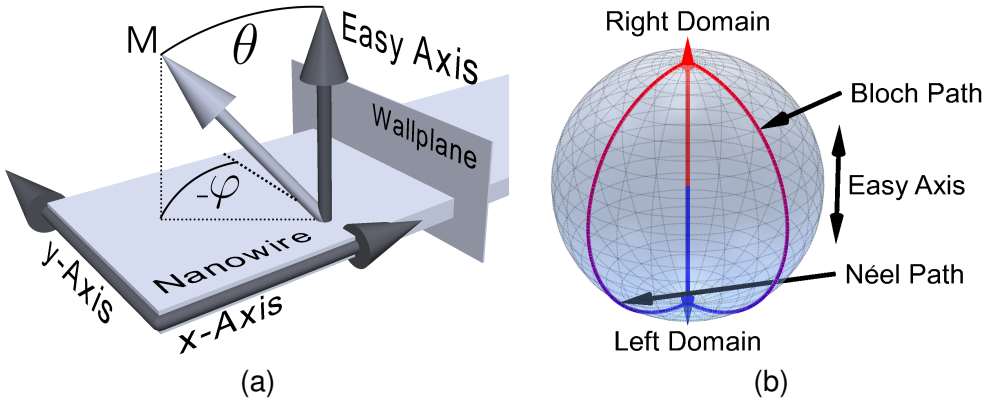

Figure 4.1: (a) Depiction of the coordinate system and how the magnetic moment ***M*** is related to its axes. The polar angle θ is defined as the angle between the magnetization and the anisotropy easy axis which is aligned in parallel with the z-axis. The azimuthal angle φ is described as the angle between the magnetic moment, projected on the nanowire plane, and the plane of the domain wall. In nanowires the wall plane is oriented in parallel with the y-axis, since then the domain-wall length and hence the energy cost due to the domain wall is minimal. (b) Within the domain wall the magnetization performs a rotation by 180° from the right to the left domain. While the Bloch wall is characterized by a helical rotation of the magnetization in parallel with the wall plane ($\varphi = 0, \pm\pi$), in a Néel wall the magnetic moments rotate perpendicular to the wall plane ($\varphi = \pm\pi/2$), as depicted by the Bloch and Néel path.

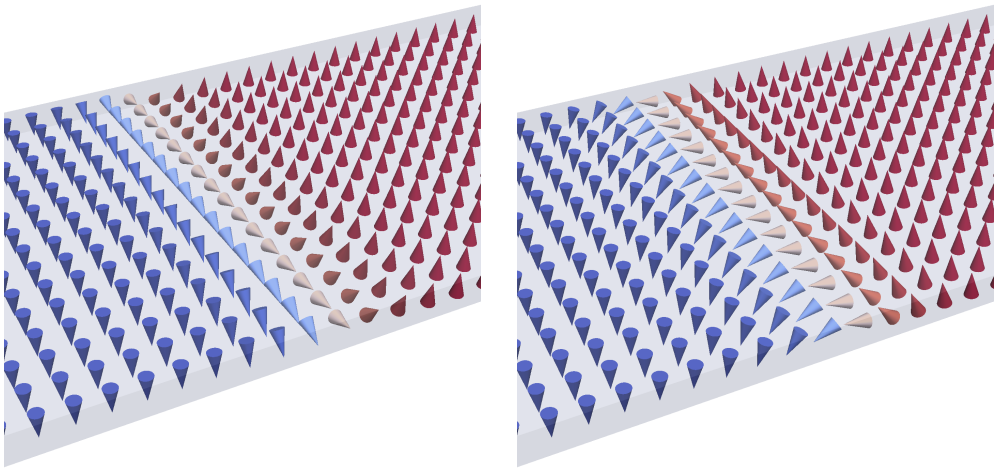

Figure 4.2: A Bloch wall (a) and a Néel wall (b) in a nanowire. While the magnetic moments within a Bloch wall rotate in parallel with the wall plane, within the Néel wall they rotate perpendicular to the wall plane.

Ref. [43]. In an infinitely extended thin film the energy density reads

$$U_{\mathrm{dw}} = \int \left(A \left(\frac{\partial \theta}{\partial x} \right)^2 + K_{\mathrm{eff}} \sin^2 \theta \right) \mathrm{d}x. \tag{4.1.1}$$

Here, the first term is the exchange energy density (see Eqn. 2.3.28) written in spherical coordinates and thus

$$A \left(\nabla \frac{\boldsymbol{M}}{M_{\mathrm{s}}} \right)^2 = A(\nabla\theta)^2 + A \sin^2\theta (\nabla\varphi)^2 = A(\nabla\theta)^2. \tag{4.1.2}$$

The latter transformation considers the azimuthal angle φ to be constant. The second term of the energy density corresponds to the effective anisotropy energy including the contributions due to the crystalline anisotropy and the shape anisotropy. The variation of the energy density functional with respect to the polar angle θ of the magnetization yields at equilibrium

$$2A \left(\frac{\partial^2 \theta}{\partial x^2} \right) = 2K_{\mathrm{eff}} \sin\theta \cos\theta. \tag{4.1.3}$$

Multiplication with $\partial\theta/\partial x$ and integration results in

$$A \left(\frac{\partial \theta}{\partial x} \right)^2 = K_{\mathrm{eff}} \sin^2 \theta \tag{4.1.4}$$

where constant terms have been omitted. Thus in the energetic equilibrium of the system the contributions of the exchange energy and the anisotropy energy to the domain wall are even. The magnetic configuration adjusts itself to an optimal relation between fast rotation (high exchange energy) and slow rotation (high anisotropy energy) resulting in a certain domain-wall width which depends on the material parameters. The change of the magnetization angle θ through a Bloch wall is obtained by solving Eqn. 4.1.4

$$\mathrm{d}x = \sqrt{\frac{A}{K_{\mathrm{eff}}}} \sin^{-1}\theta \, \mathrm{d}\theta. \tag{4.1.5}$$

Inserting Eqns. 4.1.4 and 4.1.5 into Eqn. 4.1.1 allows for the calculation of the energy density per unit area of the domain wall

$$U_{\mathrm{dw}} = 2\sqrt{AK_{\mathrm{eff}}} \int_0^{\pi} \sin\theta \, \mathrm{d}\theta = 4\sqrt{AK_{\mathrm{eff}}}. \tag{4.1.6}$$

The total energy due to a domain wall can now be obtained by a simple surface integration of the energy density over the cross section of the nanowire. The resulting energy for a Bloch wall and a Néel wall is apparently the same, since the energy density U_{dw} does not depend on the azimuthal angle φ.

4.1.3 Domain-wall Profile

The actual development of the magnetization angle θ in dependence on the position x inside the domain wall is referred to as domain-wall profile. It can be obtained from the change of the magnetization through a Bloch wall (see Eqn. 4.1.5). Therefor $\theta = \theta' + \pi/2$ is substituted and the equation is integrated

$$\int \mathrm{d}x = \sqrt{\frac{A}{K_{\mathrm{eff}}}} \int \frac{1}{\sin\theta}\,\mathrm{d}\theta = \sqrt{\frac{A}{K_{\mathrm{eff}}}} \int \frac{1}{\cos\theta'}\,\mathrm{d}\theta'. \tag{4.1.7}$$

With some transformations and reverse substitution of θ' this finally results in

$$\theta(x) = \arcsin\left(\tanh\left(\frac{x}{\sqrt{A/K_{\mathrm{eff}}}}\right)\right) + \frac{\pi}{2} \tag{4.1.8}$$

where the domain wall is assumed to be located at $x = 0$. The magnetization angle θ also known as the domain-wall profile describes the smooth transition of the magnetic moments within the domain wall from one domain to another. Since it does not depend on the azimuthal angle φ the wall profile is valid for both Bloch walls and Néel walls.

4.1.4 Domain-wall Width

Directly from the magnetization profile an important quantity to describe the domain wall is derived – the domain-wall width. Since the rotation of the magnetization occurs smoothly in the domain wall, there is no consistent description of its width in literature. A recent and common definition is the inverse of the magnetization slope in the center of the domain wall and thus its width is calculated by

$$a = \left(\frac{\partial\theta}{\partial x}(0)\right)^{-1} = \sqrt{\frac{A}{K_{\mathrm{eff}}}}. \tag{4.1.9}$$

As can be expected from energetic considerations an increasing exchange constant A, which results in a smoother rotation of the magnetization, increases the domain-wall width a, while a higher anisotropy constant K, which favors a faster rotation, decreases it.

4.2 Creation of Domain Walls

In order to use domain walls in a controlled manner in ferromagnetic nanostructures at first a reliable creation of domains and thereby domain walls is crucial. Since the size of the investigated nanostructures is small, a once saturated sample remains in a monodomain state unless a domain wall is injected. The usual way to create a domain

wall is to reverse the magnetization locally which can be a challenging task.

One possibility to rotate or switch the magnetization is the application of an external field. If this field is applied anti-parallel to a saturated sample with perpendicular magnetic anisotropy, the magnetization becomes unstable at a certain field strength and aligns in parallel to the external field. The onset of this irreversible rotation of the magnetization is referred to as nucleation and the corresponding field is subsequently called nucleation field. If the nucleation is spatially limited in the sample, a domain wall is created. Since in perfect samples the created domain wall propagates under the influence of the external field through the whole sample and the magnetization is completely switched, the nucleation field is also referred to as switching field.

In the following section the Stoner-Wohlfarth model is discussed shortly. Then a technique to determine the switching field with an incoherent rotation of the magnetization is introduced. Based on this the localized nucleation of the magnetization in a nanowire with perpendicular magnetic anisotropy is investigated and described analytically. Parts of this section have been published in Ref. [17].

4.2.1 Nucleation in the Stoner-Wohlfarth Model

The Stoner-Wohlfarth model is one approach to describe the switching of the magnetization [119]. It considers the rotation of a single-domain particle under the influence of an external field. Thus the switching field of a nanowire can only be calculated with the Stoner-Wohlfarth model if a coherent rotation of the magnetic moments is assumed. In this case the exchange energy can be omitted and the energy density of a nanowire with perpendicular magnetic anisotropy under the influence of an external Zeeman field H_{zee} in dependence on the magnetization angle θ reads

$$U(\theta) = K_{\mathrm{eff}} \sin^2(\theta - \theta_0) + \mu_0 M_{\mathrm{s}} H_{\mathrm{zee}} \cos(\theta - \theta_0) \tag{4.2.1}$$

where the oblique angle θ_0 is the result of an inclination of the external field from the plane normal of the nanowire. In general, the switching of the magnetization is the overcoming of an energy barrier between parallel and anti-parallel alignment of the magnetic moments with the external field due to the anisotropy. The application of the external Zeeman field opposite to the magnetization lowers this engery barrier and from the energy density it can be deduced that the barrier vanishes if the first derivative is $\mathrm{d}U/\mathrm{d}\theta = 0$ (further rotation costs no more energy) and the second derivative is $\mathrm{d}^2U/\mathrm{d}\theta^2 < 0$ (further rotation lowers the energy of the system) [119,120]. The magnetic moments rotate spontaneously and irreversible and the corresponding switching field can be calculated as

$$H_{\mathrm{s}}(\theta_0) = \left[(\cos\theta_0)^{2/3} + (\sin\theta_0)^{2/3}\right]^{-3/2} \cdot \frac{2K_{\mathrm{eff}}}{\mu_0 M_{\mathrm{s}}} = C_0 \frac{2K_{\mathrm{eff}}}{\mu_0 M_{\mathrm{s}}}. \tag{4.2.2}$$

However, the Stoner-Wohlfarth model is only appropriate for the description of coherent switching in an infinitely extended thin film where the magnetic moments are in parallel during rotation. In a confined geometry on the other hand, the nucleation is spatially limited and thus the magnetization does not switch coherently. Hence exchange coupled adjacent magnetic moments are not aligned in parallel during the switching process and give rise to exchange energy which is neglected in this model.

4.2.2 Nucleation described by Linearized Micromagnetic Equations

To take exchange energy into account the linearized micromagnetic equation is introduced as proposed by Aharoni [116] and rewritten by Skomski [121]. If the exchange constant A is assumed to be constant the linearized micromagnetic equation reads

$$-A\nabla^2\boldsymbol{m} + \left(C_0 K_{\text{eff}} - \frac{\mu_0 M_\text{s} H_\text{zee}}{2}\right)\boldsymbol{m} = 0 \tag{4.2.3}$$

where K_{eff} is the effective anisotropy constant, M_s is the saturation magnetization, A is the exchange constant, H_zee is an applied Zeeman field, and C_0 is a correction of the energy due to an oblique angle between the external field and the anisotropy easy axis. $\boldsymbol{m} = \boldsymbol{M} - M_\text{z}\boldsymbol{e}_\text{z}$ is a perpendicular deviation of the magnetization from the anisotropy easy axis $\boldsymbol{e}_\text{z}$ (the plane normal of the nanowire). Equation 4.2.3 has the same form as the Schrödinger equation and thus it is possible to solve switching problems based on the linearized micromagnetic equation via eigenmode analysis. The time independent Schrödinger equation reads

$$-\frac{\hbar^2}{2m}\nabla^2\psi + (V(\boldsymbol{r}) + E)\psi = 0 \tag{4.2.4}$$

where $V(\boldsymbol{r})$ is a potential related to the specific formulation of the problem. By comparing Eqn. 4.2.3 and Eqn. 4.2.4 it is possible to identify the terms

$$\frac{\hbar^2}{2m} = A, \quad E = C_0 K_{\text{eff}} - \frac{\mu_0}{2} M_\text{s} H_\text{zee} \quad \text{and} \quad \psi = \boldsymbol{m}. \tag{4.2.5}$$

Thus if $V(\boldsymbol{r})$ is adapted to a specific switching problem it is possible to calculate the eigenmodes and eigenvalues of $\boldsymbol{m}$. The eigenmode with the lowest eigenvalue is the so-called nucleation mode at which the magnetization switches [121]. The switching field can then be determined from its eigenvalue.

4.2.3 Nucleation at a Round Modification of the Anisotropy

As can be seen from Eqn. 4.2.2 the switching field is directly proportional to the effective anisotropy constant K_{eff}. Thus a modification of the material parameters as described in

Sec. 3.1.3 can be utilized to reduce the switching field. If the reduction of the anisotropy is spatially limited to a certain area as depicted in Fig. 5.1(a), the nucleation is usually located at such intentional modifications and thus they are referred to as nucleation sites.

The linearized micromagnetic equation can be used to describe the switching of the magnetization in a round nucleation site with reduced anisotropy K_1 analytically. Therefore the coordinate system is changed into two-dimensional polar coordinates. The linearized micromagnetic equation 4.2.3 then reads

$$-A\left(\frac{\mathrm{d}^2\boldsymbol{m}}{\mathrm{d}r^2}+\frac{1}{r}\frac{\mathrm{d}\boldsymbol{m}}{\mathrm{d}r}+\frac{1}{r^2}\frac{\mathrm{d}^2\boldsymbol{m}}{\mathrm{d}\varphi}\right)+(V(r)-C_0K_{\mathrm{eff}}+\frac{\mu_0}{2}M_{\mathrm{s}}H_{\mathrm{zee}})\boldsymbol{m}=0. \tag{4.2.6}$$

The area of nucleation is in general located at the nucleation site and the magnetization switches quasi coherently. Quasi coherent means that the switching of the magnetization is characterized by a uniform rotation direction of the magnetic moments. The rotation angle of the magnetization depends on the distance to the center of the nucleation site. Hence the deviation from the anisotropy easy axis reduces to $\boldsymbol{m}(\boldsymbol{r}) = m(r)\boldsymbol{e}_{\mathrm{m}}$ with $\boldsymbol{e}_{\mathrm{m}}$ being the rotation direction of the magnetization and the magnitude is given by $m(r) = |\boldsymbol{m}(\boldsymbol{r})|$ as described in Ref. [15]. Thus the linearized micromagnetic equation in polar coordinates reduces with some transformations to

$$\frac{\mathrm{d}^2m}{\mathrm{d}r^2}+\frac{1}{r}\frac{\mathrm{d}m}{\mathrm{d}r}+k^2m=0 \tag{4.2.7}$$

with

$$k^2=\frac{2V(r)+2C_{\mathrm{o}}K_{\mathrm{eff}}-\mu_0M_{\mathrm{s}}H_{\mathrm{zee}}}{2A} \tag{4.2.8}$$

The solutions of equation 4.2.7 are the well known Bessel functions $m(r) = j_0(kr)$ [122].

The round nucleation site with lowered anisotropy in the film can be described by a potential $V(r) = -C_0\Delta K$ inside the modification and $V(r) = 0$ outside the modification with $C_0\Delta K$ denoting the reduction of the anisotropy constant K_1 with the correction due to the oblique field. This leads to two regions with different k^2 in the thin film

$$k^2=\begin{cases}k_0^2=\frac{2C_0(K_{\mathrm{eff}}-\Delta K)-\mu_0M_{\mathrm{s}}H_{\mathrm{zee}}}{2A} & \text{for} \quad 0\le r\le R_{\mathrm{mod}},\\ \kappa^2=-\frac{2C_0K_{\mathrm{eff}}-\mu_0M_{\mathrm{s}}H_{\mathrm{zee}}}{2A} & \text{for} \quad r>R_{\mathrm{mod}}\end{cases} \tag{4.2.9}$$

where R_{mod} is the radius of the nucleation site. This is the same problem as the quantum mechanical finite round potential well (cf. Ref. [123]). To obtain allowed solutions of the nucleation mode $m(r)$, the Bessel functions for the two regions and their first derivative has to be equal at $r = R_{\mathrm{mod}}$. This can be combined to the transcendent equation

$$k_0\frac{\mathrm{d}}{\mathrm{d}z}\ln j_0(z)|_{z=k_0R_{\mathrm{mod}}}\overset{!}{=}i\kappa\frac{\mathrm{d}}{\mathrm{d}z}h_0(z)|_{z=i\kappa R_{\mathrm{mod}}} \tag{4.2.10}$$

where $z = kr$ and h_0 is the Hankel function which has to be used instead of the Bessel function j_0 to ensure an exponential decrease of the eigenfunctions in the classically forbidden region.

The switching field H_s is obtained from the lowest energy that solves Eqn. 4.2.10 for given $V(r)$ and R_{mod}. It has to be determined numerically because this is a transcendent equation and explicit solutions are not available.

4.3 One-dimensional Dynamics

Once domains are created within a sample like a nanowire the therewith associated domain walls are suitable for all kinds of manipulations as desired for new storage concepts. The usual ways to induce movement of domain walls is either an external field or to apply a current through the nanowire. To gain a better understanding of what happens if a domain wall is manipulated by these external forces an analytical description of the domain-wall dynamics is introduced. Tatara and Kohno [124], Thiaville et al. [125], and both Tretiakov et al. as well as Clarke et al. [126, 127] derived a set of equations of motion in different formalisms, all based on a collective-coordinate approach. The following calculations of the domain-wall dynamics in nanowires with perpendicular magnetic anisotropy will be only a summarized version of the actual calculations as for example carried out in [128]. While the original models are calculated for domain walls in soft magnetic materials, the approach is suitable for Bloch and Néel domain walls in PMA materials as well.

4.3.1 Collective-coordinate Approach

The general principle of the collective-coordinate approach is to reduce arbitrary degrees of freedom of a system to a certain set of variables that are sufficient to describe the system's temporal evolution. A nanowire with perpendicular magnetic anisotropy and a domain wall inside is perfectly suited for this method, since the change of magnetization during domain-wall motion is limited to the domain wall itself. The system can thus be described by only few collective coordinates C_i that characterize the domain wall and its motion. Thus the temporal evolution of the magnetization can be expressed by

$$\frac{\mathrm{d}\boldsymbol{M}(\boldsymbol{r},\boldsymbol{C})}{\mathrm{d}t} = \sum_i \frac{\partial \boldsymbol{M}(\boldsymbol{r},\boldsymbol{C})}{\partial C_i}\frac{\partial C_i}{\partial t}. \tag{4.3.1}$$

By inserting this collective-coordinate dependent time derivative of the magnetization into the implicit Landau-Lifshitz-Gilbert equation 2.2.10 and adding the spin-torque dependent terms from Eqn. 2.2.28, with some calculations a general equation of motion

of a magnetic configuration that depends on collective coordinates can be found [126]:

$$-\boldsymbol{F} = (\boldsymbol{G} + \alpha \boldsymbol{D}) \frac{\partial \boldsymbol{C}}{\partial t} + (\boldsymbol{A} + \xi \boldsymbol{N})\, b_\mathrm{j} \boldsymbol{j}. \tag{4.3.2}$$

Here, $\boldsymbol{F}$ is the force on the magnetization that denotes the change of the system energy in dependence on the collective coordinates. For the i-th coordinate it is given by

$$\boldsymbol{F}_\mathrm{i} = -\int \frac{\delta E}{\delta \boldsymbol{M}} \frac{\partial \boldsymbol{M}}{\partial C_\mathrm{i}} \,\mathrm{d}\boldsymbol{r} = -\frac{\partial E}{\partial C_\mathrm{i}} \tag{4.3.3}$$

where $\delta E / \delta M$ includes all energies that contribute to the effective field, see Sec. 2.3. Furthermore, the force $\boldsymbol{F}$ has to be in equilibrium with the evolution of the magnetization in dependence on the collective coordinates and the influence of an applied current, given by the right-hand side of Eqn. 4.3.2. The corresponding tensors are given by the gyro tensor

$$\boldsymbol{G}_\mathrm{ij} = \frac{\mu_0}{\gamma M_\mathrm{s}^2} \int \boldsymbol{M} \cdot \left(\frac{\partial \boldsymbol{M}}{\partial C_\mathrm{i}} \times \frac{\partial \boldsymbol{M}}{\partial C_\mathrm{j}} \right) \mathrm{d}\boldsymbol{r}, \tag{4.3.4}$$

the dissipation tensor

$$\boldsymbol{D}_\mathrm{ij} = -\frac{\mu_0}{\gamma M_\mathrm{s}} \int \frac{\partial \boldsymbol{M}}{\partial C_\mathrm{i}} \cdot \frac{\partial \boldsymbol{M}}{\partial C_\mathrm{j}} \,\mathrm{d}\boldsymbol{r}, \tag{4.3.5}$$

the adiabatic spin-torque tensor

$$\boldsymbol{A}_\mathrm{ij} = -\frac{\mu_0}{\gamma M_\mathrm{s}^2} \int \boldsymbol{M} \cdot \left(\frac{\partial \boldsymbol{M}}{\partial C_\mathrm{i}} \times \frac{\partial \boldsymbol{M}}{\partial \boldsymbol{r}_\mathrm{j}} \right) \mathrm{d}\boldsymbol{r}, \tag{4.3.6}$$

and the non-adiabatic spin-torque tensor

$$\boldsymbol{N}_\mathrm{ij} = \frac{\mu_0}{\gamma M_\mathrm{s}} \int \frac{\partial \boldsymbol{M}}{\partial C_\mathrm{i}} \cdot \frac{\partial \boldsymbol{M}}{\partial \boldsymbol{r}_\mathrm{j}} \,\mathrm{d}\boldsymbol{r}. \tag{4.3.7}$$

Thus Eqn. 4.3.2 describes how the magnetization evolves under internal and external forces as well as applied currents, while the system and the magnetization depends on a set of collective coordinates.

Since the tensors 4.3.3 – 4.3.7 are invariant under rotation, this approach to magnetization dynamics is suitable for different types of domain walls in different material systems. In the next step the general equation of motion for collective coordinates 4.3.2 is adapted to a Bloch and Néel wall in a nanowire with perpendicular magnetic anisotropy.

4.3.2 Equation of Domain-wall Motion

Once the general equation of motion is known, the set of equations to describe the domain-wall motion in dependence on the collective coordinates is straightforward. In

the case of a Bloch and Néel wall these coordinates will be the position q of the domain wall along the nanowire and the azimuthal angle φ which defines whether the domain wall is in Bloch or Néel configuration or somewhere in between. Since the domain wall is very rigid during motion and the azimuthal angle, also referred to as the rotation angle of the domain wall, has only a negligible influence on the magnetization profile of the domain wall, this one-dimensional description of the system is sufficient.

To calculate the domain-wall dynamics, the magnetization of the system is expressed in dependence on the collective coordinates. The magnetization in a nanowire can be easily adapted from the domain-wall profile – Eqn. 4.1.8 – and reads

$$\boldsymbol{M}(x, q, \varphi) = M_\mathrm{s} \begin{pmatrix} \sin(\varphi)\ \mathrm{sech}\left(\frac{x-q}{a}\right) \\ \cos(\varphi)\ \mathrm{sech}\left(\frac{x-q}{a}\right) \\ -\tanh\left(\frac{x-q}{a}\right) \end{pmatrix} \tag{4.3.8}$$

where the domain wall is a Bloch wall for $\varphi = 0, \pm\pi$ and a Néel wall for $\varphi = \pm\pi/2$. From the magnetization it is then possible to determine the single parts of the tensors that comprise the general equation of motion. Calculation of Eqns. 4.3.3 – 4.3.7 for the different combination of the collective coordinates and inserting into Eqn. 4.3.2 then yields with some transformations

$$\begin{pmatrix} \frac{\alpha}{a} & -1 \\ 1 & \alpha a \end{pmatrix} \begin{pmatrix} \dot{q} \\ \dot{\varphi} \end{pmatrix} = -\frac{\gamma}{2S\mu_0 M_\mathrm{s}} \begin{pmatrix} \frac{\partial E}{\partial q} \\ \frac{\partial E}{\partial \varphi} \end{pmatrix} - \begin{pmatrix} \frac{\xi}{a} \\ 1 \end{pmatrix} b_\mathrm{j} j \tag{4.3.9}$$

where S is the cross section of the nanowire. To obtain the final result, it is crucial to know how the energy of the system depends on the collective coordinates.

4.3.3 Energy of the System in Collective Coordinates

The energy of the system is not only a result of the magnetic configuration, but it also depends on external influences, the geometry of the nanowire, and other possible perturbations as pinning centers. Thus at this point the equation of domain-wall motion can be significantly influenced. In the case of a nanowire with perpendicular magnetic anisotropy the total energy of the system reads (cf. Secs. 2.3 and 4.1.2)

$$E = \int_\mathrm{V} \left(A \left(\frac{\partial \theta}{\partial x} \right)^2 + \left(K_\mathrm{eff} + K_\perp \sin^2 \varphi \right) \sin^2 \theta - \mu_0 M_\mathrm{s} H_\mathrm{ext} \cos \theta \right) \mathrm{d}\boldsymbol{r} + E_\mathrm{pin}(q) \tag{4.3.10}$$

where the third term is correlated with the finite geometry of the nanowire that results in a stray field caused by the domain walls at the edges and is expressed as an additional anisotropy energy (see Sec. 4.4.2) with the corresponding anisotropy constant $K_\perp$. Furthermore, an external field $\boldsymbol{H}_\mathrm{ext}$ is taken into account as well as an arbitrary energy E_pin to model any kind of pinning. Inserting the domain-wall profile from Eqn. 4.1.8 and

integrating then yields the derivative of the system energy with respect to the collective coordinates

$$\frac{\partial E}{\partial q} = 2S\mu_0 M_s H_{ext} + \frac{\partial E_{pin}}{\partial q} \tag{4.3.11}$$

and

$$\frac{\partial E}{\partial \varphi} = 2SaK_\perp \sin(2\varphi). \tag{4.3.12}$$

Inserting both derivatives into Eqn. 4.3.9 yields the equations that will be used in the following to describe the domain-wall dynamics in a nanowire with perpendicular magnetic anisotropy and they read

$$\frac{\alpha \dot{q}}{a} - \dot{\varphi} = -\gamma H_{ext} - \frac{\xi u}{a} + \frac{\gamma}{2\mu_0 M_s}\frac{\partial V_{pin}}{\partial q} \tag{4.3.13}$$

and

$$\frac{\dot{q}}{a} + \alpha\dot{\varphi} = -\frac{\gamma}{\mu_0 M_s} K_\perp \sin(2\varphi) - \frac{u}{a} \tag{4.3.14}$$

where $u = b_j j$ is the applied current and $V_{pin} = E_{pin}/S$ is an arbitrary energy surface density that can be used to model pinning potentials for the domain wall along the nanowire. It has to be noted that S. Zhang and Z. Li [53] derived a slightly different term u for the current used here than e.g. G. Tatara and H. Kohno [124] which is widely used in literature as well. However, due to their minimal difference they will be used equivalently, since

$$u_{ZL} = \frac{jP\mu_B}{eM_s(1+\xi^2)} \approx \frac{jPg\mu_B}{2eM_s} = u_{TK} \quad \text{for} \quad \xi \ll 1 \tag{4.3.15}$$

which is the case in the simulations throughout this thesis.

4.4 Pinning of Domain Walls

In the context of domain-wall dynamics in nanowires related to the racetrack memory the control of the domain-wall motion is a crucial point. Reliable pinning sites are necessary in order to achieve a high data stability but their creation is a still demanding challenge. The basic principle of controlled pinning is rather simple. An imperfect nanowire comprises defects of the crystal structure, inclusions, or indentation at the edges that affect the domain wall and its energy. Thus the domain wall is propagating through an energy landscape meaning that the system energy depends on the domain-wall position. Based on these findings it is therefore logical to tailor the energy landscape by adapting these imperfections in order to create artificial pinning sites.

A very promising technique to pin domain walls which will be discussed in detail in the following is the local modification of the anisotropy constant. As pointed out in Sec. 3.1.3 this can be achieved for example by ion irradiation or the application of electric

fields. In this section the pinning potential that arises from the interplay of a domain wall with an area of reduced anisotropy is described. Furthermore, another potential that can interrupt the domain-wall movement and that is a consequence of the domain wall's stray field is introduced. Parts of this section have been published in Ref. [35].

4.4.1 Pinning at an Anisotropy Boundary

As exemplarily depicted in Fig. 3.1 the mainly investigated system is a nanowire comprising a local modification of the anisotropy constant. An anisotropy boundary is then defined as the transition from the modified area to the remaining part of the nanowire and thus it is basically a step in the anisotropy constant. If K_1^{red} is assumed to be a reduced anisotropy constant in the intentional modification then the step has the height

$$\Delta K = K_1 - K_1^{\mathrm{red}}, \tag{4.4.1}$$

where K_1 is the unmodified anisotropy constant in the rest of the nanowire. The anisotropy boundary is accordingly also referred to as K-step of the height ΔK.

Now a domain wall is assumed that propagates through the nanowire. The energy of the system changes as a domain wall passes such a K-step and enters or leaves the modified area, since the energy density of a domain wall depends on the anisotropy constant at its position as it directly appears from Eqn. 4.1.6. In the case of a reduced anisotropy constant in the modified area, the system energy decreases as the domain wall is located inside the modification. Thus a propagating domain wall gets pinned at the K-step and a certain force has to be applied on the wall to depin it, meaning to push the domain wall beyond the anisotropy boundary and thereby increase the energy of the system. The corresponding pinning potential V_{pin} will be derived in the following.

The energy density of a nanowire with a domain wall inside at a position x can be calculated from Eqn. 4.1.1 by inserting the domain-wall profile from Eqn. 4.1.8, cf. [17, 32]. The calculation is comparable to the calculation of the system energy in Sec. 4.3.3, but no external field and no finite geometry is taken into account. If the domain-wall center is located at position q the energy density reads

$$U_{\mathrm{dw}}(x, q) = \left(\frac{A}{a^2} + K_{\mathrm{eff}}(x) \right) \operatorname{sech}^2 \left(\frac{x - q}{a} \right) \tag{4.4.2}$$

where a is the domain-wall width, which is assumed to be invariant, although the anisotropy constant might change along the nanowire. $K_{\mathrm{eff}}(x) = K_1(x) - \mu_0 M_{\mathrm{s}}^2/2$ is the effective anisotropy constant of a thin film and it depends on the position x due to the K-step.

To obtain the energy density of the domain wall which corresponds to the pinning potential V_{pin}, an integration along the nanowire has to be carried out. If the K-step is

assumed to be at $x = b$ the integration is

$$\begin{aligned} V_{\text{pin}}(q) &= \int_{-\infty}^{b} U_{\text{dw}}(x,q)\,\mathrm{d}x + \int_{b}^{+\infty} U_{\text{dw}}(x,q)\,\mathrm{d}x \\ &= \frac{2A}{a} + 2aK_{\text{eff}} - a\Delta K\left(1 - \tanh\left(\frac{b-q}{a}\right)\right). \end{aligned} \tag{4.4.3}$$

For the one-dimensional model that is employed to describe the domain wall motion along a nanowire only the change in the potential V_{pin} with respect to a domain wall movement is relevant. Thus constant terms are irrelevant and as the domain wall passes a K-step at $b = 0$ the change of the system energy is given by

$$\frac{\partial V_{\text{pin}}}{\partial q} = \Delta K \operatorname{sech}^2\left(\frac{q}{a}\right). \tag{4.4.4}$$

The pinning potential has its maximum slope and thereby its maximum force on the domain wall if the center of the wall is located directly at the K-step, meaning $q = 0$ and $\partial V_{\text{pin}}/\partial q = \Delta K$. This conclusion holds true for arbitrary widths of the domain wall.

Due to its possibly artificial origin and its independence of the potential from the magnetic configuration of the system this kind of pinning is also referred to as extrinsic pinning. To overcome the extrinsic potential barrier that is caused by the K-step a certain force has to be applied. The forces are usually either an external field or a current through the nanowire. The calculation of the threshold values that are needed to depin the domain wall are a main topic of this thesis and will be part of the next chapter.

4.4.2 Stray Field of Domain Walls in Nanowires

As introduced in Sec. 2.2.4 a current that flows through a nanowire with a domain wall inside has two impacts on the wall: On the one hand it results in a displacement of the domain wall along the nanowire and on the other hand it distorts the domain wall. In the case of a Bloch or Néel wall inside a nanowire with perpendicular magnetic anisotropy the distortion means a tilting of the magnetic moments inside the wall and hence a rotation of the domain wall. With regard to the one-dimensional model, that is used to describe the temporal evolution of the domain wall, the impacts correspond to a change of the domain-wall position q and the rotation angle φ of the domain wall.

The rotation angle gives rise to another energy term in the micromagnetic description of a system with a domain wall inside a nanowire as already mentioned in Eqn. 4.3.10. The different magnetic configurations of a Bloch ($\varphi = 0, \pm\pi$) and a Néel wall ($\varphi = \pm\frac{\pi}{2}$) results in different stray-field configurations caused by the domain walls. But, the stray field of a Bloch wall in nanowires of the investigated dimensions (see Fig. 3.1) has a lower energy than the stray field of a Néel wall. As depicted in Fig. 4.3(a) at the edge of the nanowire, where the Bloch wall is located, surface charges occur, which cause

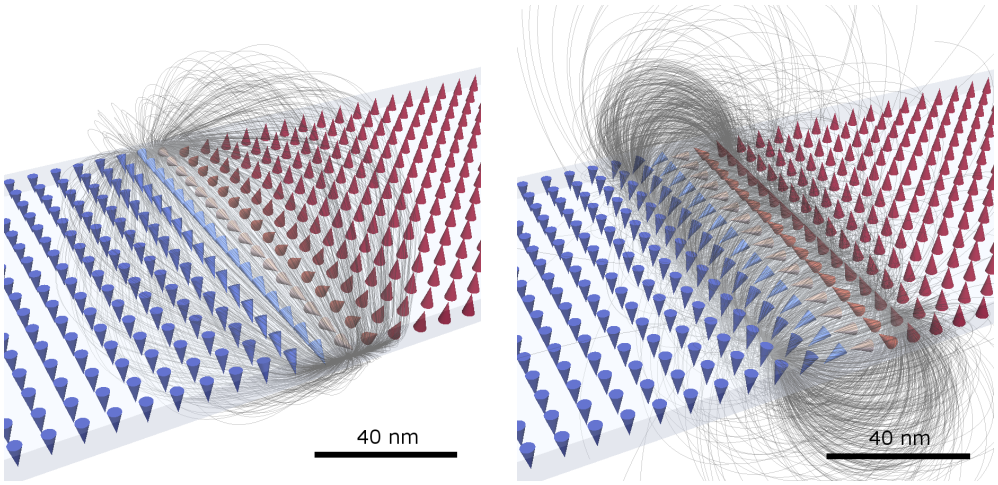

Figure 4.3: Stray field of (a) a Bloch and (b) a Néel wall. While the Bloch wall causes surface charges at the edge of the nanowire the Néel wall causes volume charges inside the nanowire. The energy difference of the stray fields of both configurations results in an effective anisotropy.

a stray field whose energy is proportional to the width of the domain wall. A Néel wall does not induce surface charges but volume charges (see Fig. 4.3(b)) and their amount is proportional to the width of the nanowire. Thus a Bloch wall is energetically favorable in the described nanowire and a restoring force occurs that prevents a rotation of the magnetic moments of the domain wall and thereby a transition from the Bloch into a Néel wall.

Hence, the transformation of a Bloch wall into a Néel wall under the influence of a current increases the energy of the system due to the different stray fields. Thus an additional energy barrier in dependence on the collective coordinate φ has to be overcome to rotate the domain wall. Due to its characteristic this barrier can be modeled like a rotation anisotropy energy U_{rot} as has been done in Eqn. 4.3.10 and reads

$$U_{\text{rot}} = K_{\perp} \sin^2 \varphi. \tag{4.4.5}$$

The rotation anisotropy is mainly determined by the effective rotation anisotropy constant $K_{\perp}$ and in literature it is often expressed by the corresponding restoring field $H_{\perp} = 2K_{\perp}/\mu_0 M_s$. For the calculation of this barrier the determination of the effective rotation anisotropy $K_{\perp}$ is a crucial prerequisite. According to [129] the rotation anisotropy constant is defined by the difference in the stray fields that arises from the domain walls:

$$K_{\perp} = K_y - K_x \tag{4.4.6}$$

where K_y corresponds to the stray-field energy of a Bloch wall and K_x to a Néel wall.

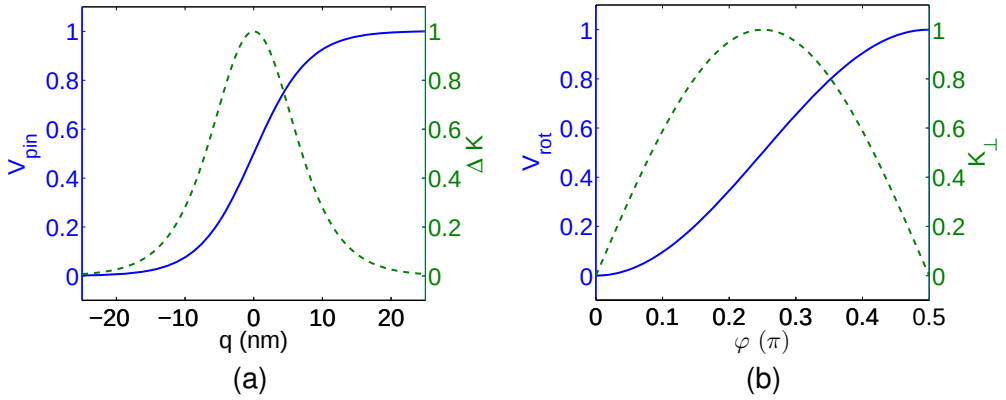

Figure 4.4: (a) Pinning potential V_{pin} (solid line) and its derivative (dashed line) in dependence on the position q of a 8 nm wide domain wall. A K-step with the height ΔK at $x = 0$ is assumed. The maximum repelling force acts on the domain wall if it is directly located at the K-step. (b) Rotation potential V_{rot} (solid line) and its derivative (dashed line) in dependence on the rotation angle φ of the domain wall. The restoring force is maximal if the domain wall has a rotation angle of $\varphi = \pi/4$ and is neither Bloch wall nor Néel wall but a mixed wall. Note that all plots are normalized to their maximum value.

The effective anisotropy constants are calculated by

$$K_{\text{i}} = -\frac{\mu_0 M_{\text{s}}^2}{4Sa} \iint N_{\text{ii}}(\boldsymbol{r} - \boldsymbol{r}') \operatorname{sech}\left(\frac{x}{a}\right) \operatorname{sech}\left(\frac{x'}{a}\right) \mathrm{d}\boldsymbol{r}\, \mathrm{d}\boldsymbol{r}' \tag{4.4.7}$$

where S is the cross section of the nanowire and N_{ii} is the demagnetization tensor. The factor $\operatorname{sech}\left(\frac{x}{a}\right)$ is equivalent to the deviation of the magnetic moments from the anisotropy easy axis inside the domain wall and accounts for the occurrence of magnetic charges. In the case of a Bloch wall, only interactions of the magnetic y-components (N_{yy}) are considered and thus the stray field of surface charges at the edge of the nanowire is calculated. For a Néel wall the x-components (N_{xx}) are considered and thus the stray field due to the volume charges is calculated. The demagnetization tensor and therewith the wall-rotation anisotropy constant $K_\perp$ can only be calculated numerically, e.g. following Newell et al. [130]. The domain-wall width a can be taken from two-dimensional micromagnetic simulations.

If the anisotropy constant is known, the additional energy barrier due to a transition from a Bloch wall to a Néel wall can be calculated, see Sec. 4.3.3. The corresponding surface energy density is referred to as rotation potential V_{rot} and reads

$$V_{\text{rot}} = \frac{1}{S} \int U_{\text{rot}}\, \mathrm{d}\boldsymbol{r} = 2aK_\perp \sin^2 \varphi, \tag{4.4.8}$$

and is depicted in Fig. 4.4(b). In the one-dimensional model that is employed to de-

scribe the domain-wall dynamics only the change of this anisotropy energy with respect to the rotation angle of the domain wall is relevant (see Eqn. 4.3.12) since it corresponds to the force on the domain wall. The restoring force on the domain wall is maximal if the wall is neither Bloch wall nor Néel wall but a mixed wall, meaning $\varphi = \pi/4 \pm n\pi$ and thus $\partial V_{\text{rot}}/\partial\varphi = K_{\perp}$. If the barrier is overcome the domain wall starts to perform whole rotations at a certain frequency.

Chapter 5

Simulation Results

After a substantial theoretical basis has been established in the preceding chapters, in the following the results of specific simulations will be discussed in detail. In general, an initial magnetic configuration is manipulated, either by an external field or a current, in order to determine a certain quantity as the switching field or the depinning current. The data obtained by simulations is then consequently compared with the theoretical models and furthermore the actual dynamics of the magnetic moments are described.

Two main topics are investigated – the creation of domain walls and their pinning at a step in the anisotropy constant. Thus in a first section the switching of the magnetization by a round modification of the anisotropy constant is discussed. The concept of an altered switching field as a result of a modified anisotropy constant can be transferred to nanowires with a tip end, which means the end of the nanowire is not flat but triangular-shaped like a tip. In a second section the pinning of a field- and current-driven domain wall in a nanowire, comprising a step-like change in the anisotropy constant K_1, is investigated. The corresponding depinning fields and currents are determined. The last section of this chapter deals with the interaction of the domain wall with the K-step.

5.1 Creation of Domain Walls

As already discussed at the beginning of Sec. 4.2 the reliable creation of domain walls is a crucial prerequisite to use them in a controlled manner as in the context of new storage concepts. In order to obtain domain walls that can be manipulated, the switching of the magnetization has to be limited to a certain area. If the magnetic moments are reversed by the application of an external field – as in the following – this can be a very challenging task. In experiments involving domain-wall motion in soft-magnetic nanowires the local switching can be achieved by modifying the geometry of

the wire. So-called nucleation pads are attached to the end of the nanowire to locally reduce the switching field with the help of local stray fields [4].

But here the localized switching of the magnetization in nanowires with perpendicular magnetic anisotropy is investigated. This opens up the possibility to use a different approach to limit the nucleation area – namely the local reduction of the anisotropy constant (cf. Sec. 4.2.3). As described in the following, the technique is utilized to obtain the desired switching behavior and to significantly reduce the switching fields. The knowledge gained from the simulations is then used to explain experiments where an unexpected reversal of the magnetization in nanowires with tip ends has been observed. Parts of this section have been published in Refs. [17] and [18].

5.1.1 Switching in Modified Areas

The switching at a round intentional modification with reduced anisotropy constant K_1, referred to as nucleation site, is investigated. According to previous analytical calculations (see Sec. 4.2.3) at a certain reduction of the anisotropy constant and certain size of the nucleation site, the nucleation is assumed to take place in the modified area. Thus an element of a homogeneous material with perpendicular magnetic anisotropy and a length and width of 640 nm is considered. The material parameters are the saturation magnetization M_s = 500 $\times$ 10^3 Am^{-1}, the anisotropy constant K_1 = 400 $\times$ 10^3 Jm^{-3}, the exchange constant A = 30 $\times$ 10^{-12} Jm^{-1}, and the Gilbert damping parameter α = 0.2. Inside the nucleation site the anisotropy constant K_1 is reduced homogeneously between 10% and 40% in steps of 5%. The radius R_{mod} of the nucleation site is changed between 5 nm and 100 nm in steps of 2.5 nm. An example of a nucleation site in a nanowire is shown in Fig. 5.1(a). Simulations are performed to determine the switching field H_s of nanowires with a round nucleation site. Therefor an external field is applied anti-parallel to the magnetization under an inclination of 3° to break the symmetry. The field is then increased stepwise until the magnetization switches. The obtained data is compared to analytical calculations as described in Sec. 4.2.3.

Results of the Simulation

As expected, the simulated switching field H_s strongly depends on the radius R_{mod} of the nucleation site and the reduction of the anisotropy constant K_1, as can be seen in Fig. 5.2. But at small radii R_{mod} up to 15 nm the influence of the nucleation site nearly vanishes. The local modification is too small to act as nucleus. It must have at least twice the size of the domain-wall width. Thus the nucleation is delocalized as depicted in Fig. 5.1(b). Nevertheless, a slight reduction of the switching field H_s can be observed, because the anisotropy constant K_1 has to be averaged over the sample

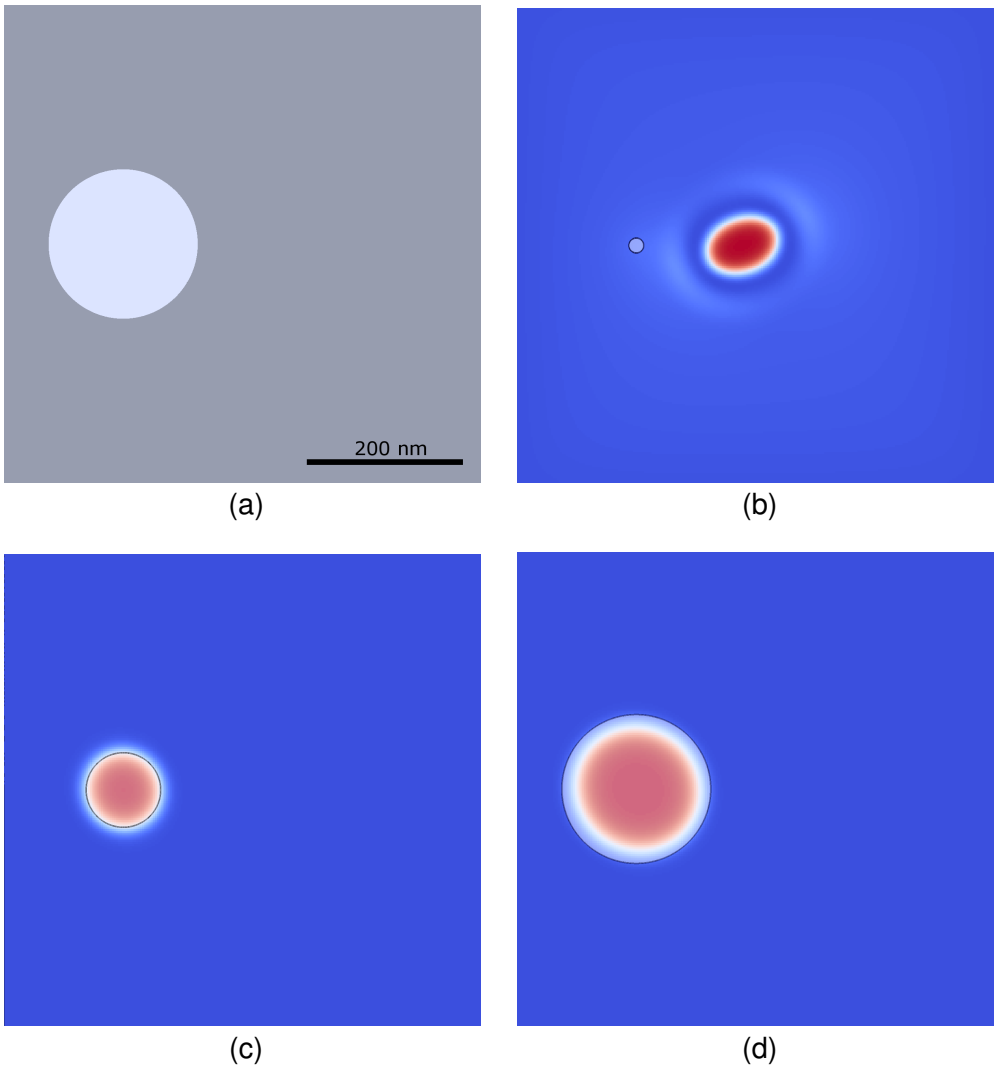

Figure 5.1: (a) Example of a nanowire for the simulation of switching in a round nucleation site. The modification (lighter area) has a radius of R_{mod} = 100 nm. For (b)-(d) the lighter areas with a black border mark the positions of the modification in the nanowire. The orientation of the magnetization is indicated by blue for downward pointing and red for upward pointing. (b) Delocalized nucleation in a nanowire with a radius R_{mod} = 10 nm of the nucleation site and a reduction of the anisotropy constant K_1 by 10%. (c) Localized nucleation in a nucleation site with R_{mod} = 50 nm and a reduction of K_1 by 40%. (d) Localized nucleation in a large nucleation site with R_{mod} = 100 nm and a reduction of K_1 by 40%.

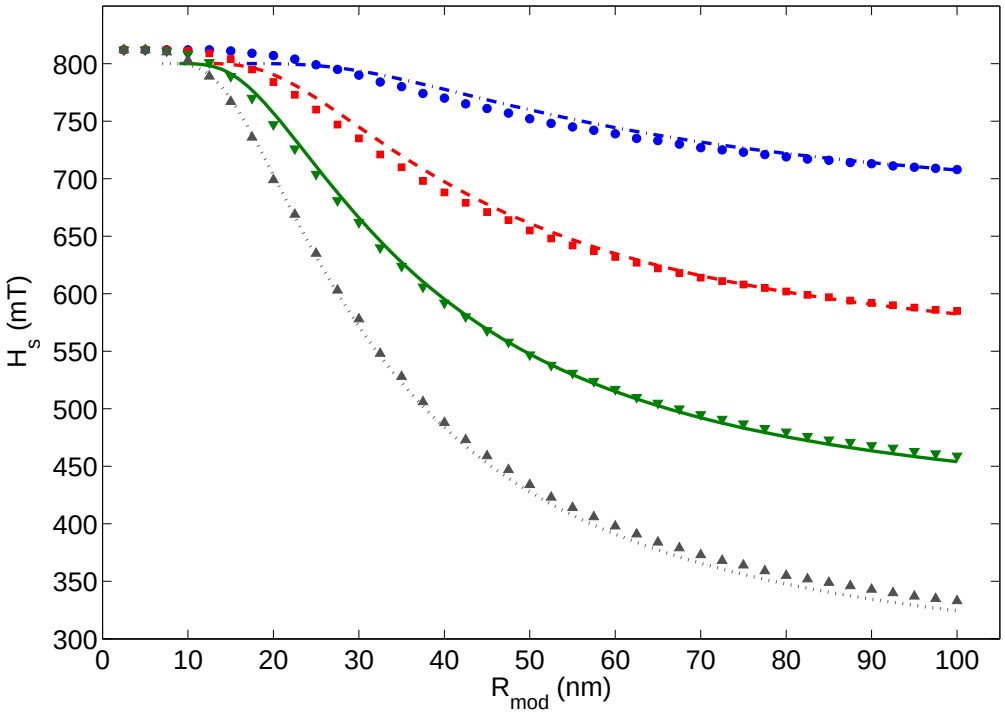

Figure 5.2: Switching field H_s of nanowires with a round nucleation site in dependence on the reduction of the anisotropy constant K_1 and the radius R_{mod} of the modification. The dash-dotted (blue), dashed (red), solid (green), and dotted (gray) lines represent the analytical solutions for a reduction of K_1 by 10%, 20%, 30%, and 40%. The circular (blue), square (red), triangular-down (green), and triangular-up (gray) symbols are corresponding simulated values.

including the nucleation site [15]. With larger radii R_{mod} the nucleation is located inside the modification as shown in Fig. 5.1(c). To switch the magnetization an energy barrier has to be overcome. The barrier increases with the length of the domain wall around the nucleation area whereas it decreases with the size of the nucleation area. The domain-wall length is proportional to the radius of the local modification and the nucleation area depends quadratically on the radius of the local modification. Thus the energy barrier and hence the switching field H_s depends reciprocally on the radius R_{mod} of the nucleation site, if the nucleation is located at the local modification.

Comparison between Simulation and Theory

The onset of the theoretical curves of the switching field H_s in Fig. 5.2 is determined by the first solution of the transcendent equation 4.2.10. At small and medium radii R_{mod} discrepancies occur between the theoretical and the simulated switching fields. For small nucleation sites the nucleation is delocalized (see Fig. 5.1(b)) meaning that the nucleation is extended over the bulk of the nanowire. A confined geometry like the nanowire results in general in an increased switching field H_s (not shown here, cf.

reference [121]). The influence of the finite geometry is not included in the analytical calculation because it is limited to the round nucleation site. Thus the theoretical switching field differs from the simulated coercive field until the modification is large enough to embed the nucleation as shown in Fig. 5.1(c). At medium radii R_{mod} (around 30-50 nm) the simulated switching fields H_{s} are smaller than the calculated fields and the deviation depends on the reduction of the anisotropy constant K_1. In the analytical model the potential is defined by an abrupt change of the anisotropy constant, but as described in Sec. 4.4.1 the potential is smooth due to the domain-wall profile. Especially for low reductions of the anisotropy with a flat slope of the potential this results in an effectively larger nucleation site and hence a smaller simulated switching field H_{s}. With larger radii R_{mod} the boundary of the nucleation site approaches the edges of the nanowire (see Fig. 5.1(d)). Although the distance is still quite large, the nucleation is then influenced by the finite size of the nanowire accordingly. The smaller the distance between nucleation site and edge of the nanowire, the more is the switching field increased. Thus the deviation between theoretical and simulated switching field decreases (for reductions of 10% and 20%) and increases (for reductions of 30% and 40%) continuously with increasing radius R_{mod}, but it would further increase for larger radii.

Conclusion

Methods from quantum mechanics have been used to calculate a micromagnetic problem. The agreement between analytical solution and simulation is excellent and if the nucleation sites would be embedded in infinitely large nanowires the increased switching field due to the interaction with the edges of the nanowire would vanish. Introducing intentional modifications with reduced anisotropy constant K_1 is a promising approach to reliably create domain walls in nanowires. By introducing a nucleation site with a radius of 60 nm and a reduction of the anisotropy by 40% it is possible to reduce the coercive field to half of the value in a nanowire without nucleation site. Nevertheless, it is not uncommon that theory predicts a switching field H_{s}, which is ten times larger than the values obtained by experiment. This is in general a result of surface effects and defects inside the nanowire. The switching of the magnetization by more localized techniques as perpendicular currents or Oersted fields can still benefit from the results.

5.1.2 OOMMF versus MicroMagnum

In contrast to the work published in Ref. [17] all simulations for this thesis are performed with MicroMagnum [42] and not with the well-known micromagnetic framework OOMMF [44]. Thus all simulations for the last section have been repeated. Since the previous results show an increased switching field due to the interaction of the rotating

magnetization with the edges of the nanowire, in the newly performed simulations the nucleation site has been embedded in a much larger sample. The general development of the switching field in dependence on the radius of the intentional modification is the same, but the obtained values are slightly lower. These results confirm the reduced influence of the confined geometry which is still present, though. However, the agreement between theoretical calculations and simulations is still excellent and the correctness of both results remains.

The simulations in larger nanowires are only possible in a reasonable time, because MicroMagnum is used which provides some significant advantages over OOMMF. At first the usability is to be mentioned. Although MicroMagnum has a similar core module like OOMMF that is written in C++ and does the actual mathematical time-consuming calculations, the setup of a simulation is easier in MicroMagnum. While the simulation script that fulfills this task has to be written in Tcl/Tk [131] for OOMMF, MicroMagnum makes use of the well-established and modern scripting language Python [132]. Not only the simulation description, but the micromagnetic solver (controls the actual simulation as depicted in Fig. 3.2) and the micromagnetic modules (energies that contribute to the magnetization dynamics, cf. Sec. 2.3) are written in Python. Thus and due to its object-oriented design, MicroMagnum can be easily extended by the user. For example, to create a cylinder with reduced anisotropy in MicroMagnum only a simple shape class that defines which points in space belong to the cylinder has to be written once. It can then be used without any effort in the simulation script to define a nucleation site with reduced anisotropy. On the contrary in OOMMF for each simulation a picture with a gray cylinder – similar to Fig. 5.1(a) – has to be created that is analyzed by OOMMF. The material parameters of the grid point are then set by the user corresponding to the gray scale value of the picture.

A further and much more important advantage of MicroMagnum is its speed. In contrast to OOMMF it is capable of simulating on graphical processing units (GPUs) which feature a large number of computational cores. The algorithms of MicroMagnum are particularly designed to compute in parallel and thus a large number of cores accelerates the computation speed significantly. For comparable structures as the nanowire the simulation is roughly about 20 times faster. This allows not only for more simulations in less time, but opens up the possibility to simulate more complex or larger systems – still in less time. While an original simulation of Sec. 5.1.1 took about 4 hours, a single simulation with MicroMagnum took 1 hour – including a 4 times larger nanowire.

For further information on the design and development of the GPU-accelerated micromagnetic simulator MicroMagnum see Ref. [133].

5.1.3 Switching in Wires with Tip Ends

To switch the magnetization of soft-magnetic nanowires and therewith inject a domain wall usually a lateral extension referred to as nucleation pad is used. To suppress the nucleation at the opposite end of the nanowire these are tip-shaped to close the magnetic flux. The same has been tried in experiments with equally designed nanowires (with nucleation pad and tip end) made of Co/Pt and thus with perpendicular magnetic anisotropy. In contrast to the previous experience with soft-magnetic nanowires, the wires with perpendicular magnetic anisotropy show a completely different behavior. The nucleation does not take place in the pad as expected, but the switching starts at the tip end of the nanowire. Moreover, the switching fields can be tuned by the opening angle of the tip.

In the following the samples used in the experiment are described and the results of the measurements are discussed. Then, micromagnetic simulations are employed to verify possible explanations for the unexpected switching behavior.

Samples in the Experiment

The samples for the experiment are prepared by electron-beam lithography, sputter deposition of the Co/Pt multilayer, and lift-off processing of the resist as illustrated in Fig. 5.3(a). During the process a Pt(5.0 nm)/[Co(0.7 nm)/Pt(2.0 nm)]$\times$4 thin-film stack was deposited on the previously prepared resist mask. After the lift-off only the nanowires made of this material stack remain. As depicted in Fig. 5.3(b) each nanowire is prepared with a tip end that is characterized by its opening angle ϕ and the corresponding length d. The design with a tip end of the nanowire in combination with the sputter process results in an unexpected wire geometry – a reduced thickness of the nanowire at the tip end as shown in Fig. 5.3(c). During the multilayer growth the Co/Pt stack was sputter deposited onto the resist mask ($\approx$ 160 nm thick). Since for magnetron sputtering the diameter of the source is comparable to its distance to the sample, shadowing by the sample morphology has to be taken into account. In case of the bottom-up approach used, the amount of deposited material locally varies and depends on the lateral distance to the edges of the resist mask. In particular, at the tip end less material is deposited compared to the straight wire segment resulting in a reduced thickness.

The magnetic properties of the nanowire are then determined from a hard-axis remagnetization curve probed with magneto-optical Kerr-effect [55] yielding a saturation magnetization of M_S = 1.4 $\times$ 10^6 Am^{-1} and an anisotropy constant of K_1 = 1.58 $\times$ 10^6 Jm^{-3}. The switching process of the nanowires is then imaged by transmission soft X-ray microscopy.

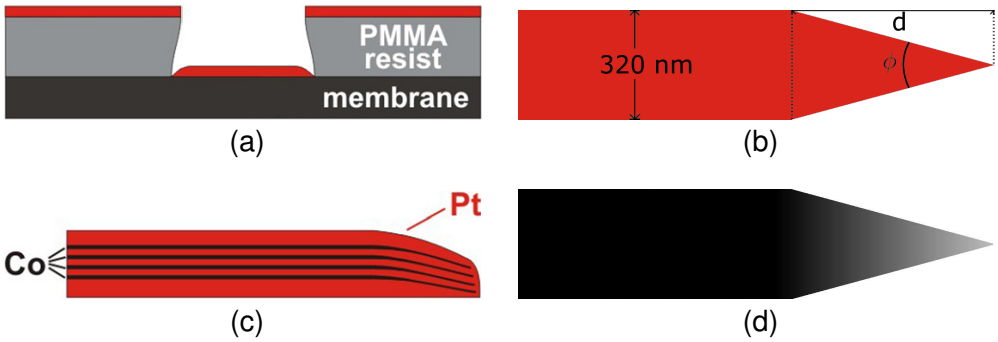

Figure 5.3: (a) Illustration of the sample preparation for the experiment. The resist mask defines the geometry of the nanowire and the needlessly sputtered material is removed together with the resist in a further preparation step. The remaining metal film is the nanowire. (b) Side view of the nanowire. Due to shadowing by the resist mask during sputter deposition of the metal film, less material is deposited at the tip end of the wire, resulting in a reduced thickness. (c) Scheme of the nanowire with tip end that is used in the experiment and in the simulations. The tip is characterized by its length d and its opening angle ϕ. (d) Top view of the nanowire. The color gradient in the tip indicates a reduced thickness and therewith a gradually reduced anisotropy constant.

Nucleation in the Experiment

In Fig. 5.4(a) an image of the investigated Co/Pt nanowire and the corresponding differential images of the magnetization switching are depicted. The tip end is located at the bottom, while the nucleation pad (not completely visible) is located at the top. After saturation of the structure with a field of -200 mT a reverse field is applied. At an external field of +11.8 mT the reversal starts (first differential image). Surprisingly the nucleation does not take place in the pad, but in the tip end of the nanowire. The therewith injected domain wall propagates through the nanowire and gets pinned twice before the entire magnetization is reversed at +12.1 mT.

The observed nucleation behavior can be attributed to a variation of the local anisotropy as a result of the above mentioned shadowing effects during the preparation, due to the following reasons. Since Co and Pt are deposited at the same angle towards the sample surface and from the same distance under the same conditions, the ratio of Co and Pt thicknesses in the multilayer stack is unaffected by the reduction of film thickness towards the tip end of the wire. It can be assumed that the saturation magnetization M_s remains basically constant down to very thin layer thicknesses [134, 135]. What is left as a changing property is the crystalline anisotropy constant K_1 which for the present system mainly originates from interface contributions. Thus a continuous reduction of the anisotropy constant K_1 towards the end of the tip as depicted in Fig. 5.3(d) is considered to be the origin for the reduction of the nucleation field. These explanation

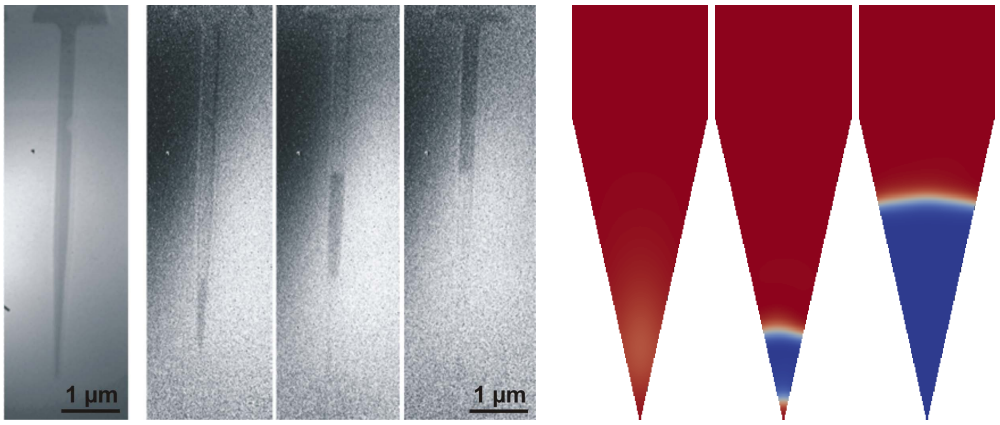

Figure 5.4: Exemplary switching process in nanowires with tip ends. The nucleation takes place in the tip and proceeds subsequently through the nanowire. (a) Absolute image (left) and corresponding differential images of the reversal process of the magnetization in the experiment. The nucleation starts at a field of 11.8 mT and during its propagation the domain wall gets pinned twice before the entire magnetization is reversed at 12.1 mT. (b) Reversal process in the simulation. The domain wall does not get pinned and the external field is held constant. Nevertheless, the nucleation and the switching process is the same as in the experiment.

is based on the findings made in Sec. 5.1.1. In other regions, where less material is deposited, the anisotropy constant might be reduced as well.

There are two reasons for the reduction of the anisotropy of the Co/Pt multilayer due to shadowing effects. The first reason is the gradual reduction of the thickness t_{Co} of the Co layer as the first order anisotropy constant K_1 decreases with decreasing t_{Co} [136]. This behavior is in accordance with other studies, see e.g. Refs. [86, 137]. The second reason for the gradual reduction of the anisotropy constant is connected with the thickness t_{Pt} of the Pt interlayer. When it falls below a certain thickness, a decrease of the anisotropy for the investigated multilayer system is observed [55]. This is in agreement with previous results [138, 139]. Consequently, a gradual reduction in the perpendicular magnetic anisotropy occurs in the regions where the Co- and Pt-layer thicknesses are gradually reduced due to shadowing effects.

Switching Fields in the Experiment

Figure 5.5 depicts the average switching field H_s as a function of the tip-opening angle ϕ determined from nine field sweeps for each data point. For all three wire widths, the same behavior is observed. The switching fields of wires with a flat end (ϕ = 180°) scatter around (+18.5 $\pm$ 0.5) mT. For decreasing angle ϕ, the switching field decreases to a value of (+7.9 $\pm$ 0.6) mT for ϕ = 2.5°. This corresponds to a reduction of the

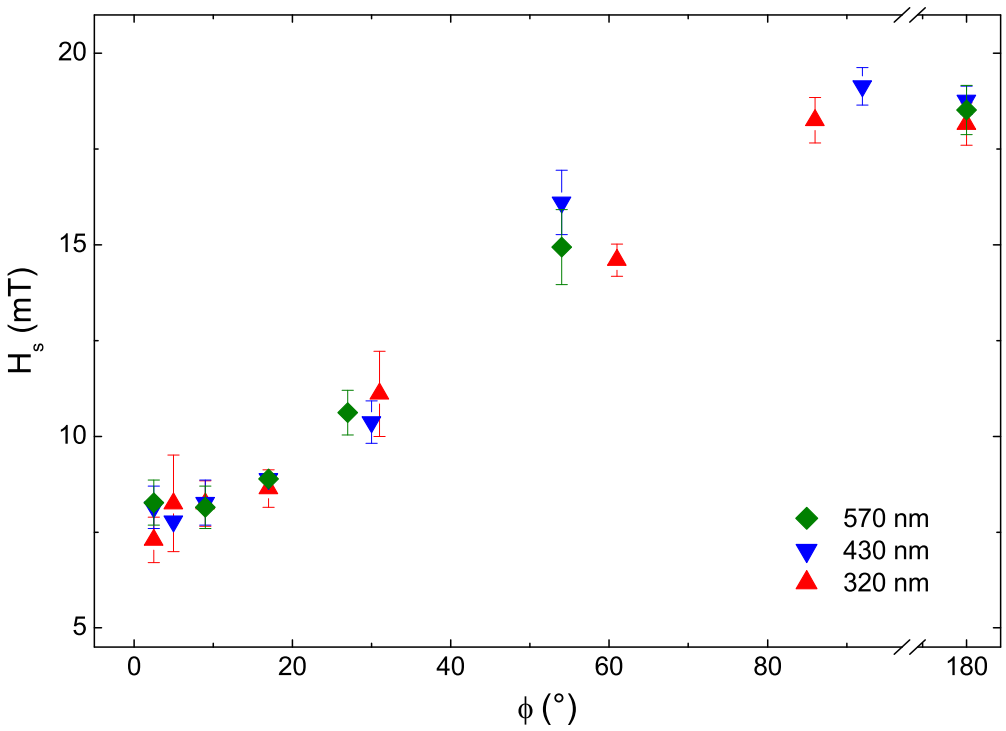

Figure 5.5: Switching field H_s in dependence on the tip opening angle ϕ determined in the experiment for three different wire widths. Up to an angle of 90° the switching field increases linearly with the opening angle whereas it stays constant for obtuser angles. The wire width has no influence on the switching field.

nucleation field by (57±5)%. Between 2.5° and 90° the switching field depends linearly on the tip-opening angle and remains constant for higher angles. The fact that there is no influence of the wire width on the switching field indicates that nucleation takes place in a volume of the tip end that is provided independently of the tip's length, which increases with increasing width of the wires. That the nucleation takes place in the tip area is in complete agreement with the images presented in Fig. 5.4(a). As stated above, the reduction of the nucleation field is assumed to originate from a decrease of the local anisotropy constant in the tip area due to shadowing during sputter deposition of the multilayer.

Setup of the Simulation

To verify the explanation for the experimental findings and to study both the anisotropy variation and the tip geometry on the switching field, micromagnetic simulations are performed – again with MicroMagnum [42]. The width of the wires in the simulations is taken as 320 nm in accordance with one type of wires studied in the experiment. The thickness of the simulated wires is 0.7 nm according to the thickness of one Co layer in the actual sample, and the multilayer structure of the Co/Pt film is not taken into

account as mentioned in Sec. 3.2.2. The simulation parameters are consistent with the material parameters of the Co/Pt multilayer, resulting in a saturation magnetization of M_s = 1.4 $\times$ 10^6 Am^{-1} and an anisotropy constant of K_1 = 1.58 $\times$ 10^6 Jm^{-3} which yields an effective anisotropy constant of K_{eff} = 350 $\times$ 10^3 Jm^{-3}. A Gilbert damping parameter of α = 0.1 is chosen, since the actual magnetization dynamics are not investigated. The external magnetic field is applied at an angle of 3° to the surface normal. This symmetry breaking is required to enable domain nucleation since the simulations are performed for zero temperature and other fluctuations are neglected. In case fluctuations and imperfections are not considered, there is usually an offset between the simulated values for the critical fields and the experimental results. This effect is known as Brown's paradox [13] and thus the data can only be compared qualitatively. The local anisotropy constant in the tip area is reduced linearly from the maximum value K_1 in the rest of the nanowire to K_{red} at the very end of the tip. The total reduction of the local anisotropy constant is varied between zero (K_{eff} = 350 $\times$ 10^3 Jm^{-3}) and 20% (K_{eff} = 34 $\times$ 10^3 Jm^{-3}). At an anisotropy reduction of 22%, the spin-reorientation transition to in-plane anisotropy occurs.

Switching Fields in the Simulation

Figure 5.6 depicts the switching field simulated for wires with tip-opening angles ϕ between 10° and 175°. For a homogeneous anisotropy constant (zero reduction, black diamonds), the geometry does not influence the switching field. This demonstrates that the reduction of the nucleation field reported above cannot be explained via the different opening angles of the tips. Assuming a local reduction of the anisotropy constant in the range of the tips results in a reduction of the switching field with decreasing tip-opening angle ϕ – as observed in the experiment. This dependence is most pronounced for the highest reduction of K_1. It is thus the amount of material with reduced anisotropy that determines the switching field H_s. For an angle ϕ = 10°, the maximum value of the switching field (that is H_s^{max} = 415 mT for flat wire ends) is reduced by 12%, 29%, 48%, and 67% for anisotropy reductions of 5%, 10%, 15%, and 20%, respectively. The simulated curves vary not only in the absolute reduction of the switching fields but also in the critical tip-opening angle at which the reduction sets in. While for a reduction of 5% the switching field stays constant down to ϕ = 130°, it drops below the maximum value already at ϕ = 155° for a reduction of 10%. The experimental values depicted in Fig. 5.5 stay constant for large angles as well and start to decrease somewhere between ϕ = 85° and ϕ = 75°. While this behavior corresponds to a reduction of the local anisotropy constant at the wire end of less than 5%, the relative decrease of the nucleation field in the experimental samples rather implies a reduction of about 18%.

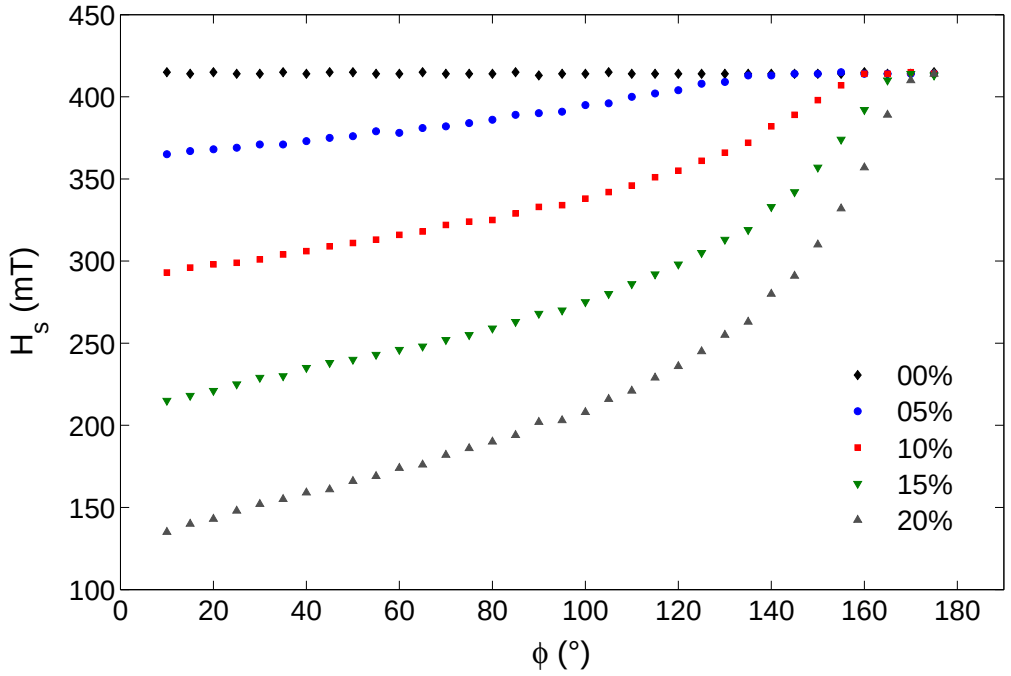

Figure 5.6: Simulated switching field H_s in dependence on the tip opening angle ϕ and the reduction of the anisotropy constant K_1 in the tip. Up to an angle of about 100° the switching field shows the same linear dependence on the opening angle as in the experiment. The higher the reduction of the anisotropy is, the lower are the switching fields. It remains constant if the anisotropy is not reduced.

Comparison of Experiment and Simulation

The experimental data show a nearly perfect linear dependence on the tip-opening angle ϕ up to 90° in accordance with the simulations. For higher angles, the experimental nucleation field remains constant, while a strengthened increase is found in the simulations. A possible explanation for this discrepancy is that shadowing effects during sputter deposition lead to a continuous reduction of the film thickness at all edges of the wires, while in the simulation abrupt edges are assumed. The gradual decay of the film thickness at the wire edges means that there is a gradual reduction of the anisotropy constant for all wires independent of the tip-opening angle. At sharp tips, the regions of both edges where the anisotropy decreases can overlap causing an anisotropy reduction in the whole tip area. For blunt tips, this effect is strongly reduced and the influence on the switching field is fading away. The experimental results therefore indicate that the reduction of the anisotropy constant is localized at the edges in contrast to the simulations where the anisotropy is reduced in the whole tip region. This probably leads to a “saturation” of the increase of the nucleation field at $\phi = 90°$ in the experiment, since the gradual reduction of the film thickness at all edges has the same effect as the gradual reduction of the film thickness in the tip ends when the tip-opening angle exceeds a critical value.

Nucleation Volume

To further investigate the influence of the wire's geometry on the nucleation field, additional simulations have been performed. Instead of having one tip-shaped end, nanowires were designed with two flat ends. Nevertheless, the anisotropy constant was reduced linearly at one end of the wire. Thereby the distance *d* over which the anisotropy decreases, corresponds to the length of a tip with a certain opening angle. The resulting switching fields show the same dependencies, but are stronger reduced in comparison to the switching fields of nanowires with tip ends. This finding qualitatively shows that nucleation depends on the total area with reduced anisotropy constant, as in nanowires with flat ends this area is much larger than in nanowires with tip ends. In particular, the region at the wire end, where the anisotropy constant is lowest, is significantly reduced in nanowires with tip ends. Rectangular wires with a comparable linear reduction of the local anisotropy constant over the same decrease length *d* (and the corresponding tip-opening angle ϕ) thus provide a larger area for a certain nucleation volume to reverse and consequently have lower switching fields. With the same arguments, it can be explained why the switching field depends on the opening angle ϕ in wires with triangular-pointed ends: the smaller ϕ, the larger is the tip area available for nucleation.

Conclusion

The critical field for the nucleation and injection of domain walls in nanowires with perpendicular magnetic anisotropy can be tuned and significantly reduced compared to the switching field of rectangular-shaped wires by designing tip-shaped wire ends. The reasoning is based on the reduction of the perpendicular magnetic anisotropy within the tip region that is caused by shadowing effects during sputter deposition of the multilayer. As confirmed by micromagnetic simulations the reduction of the local anisotropy constant accompanied by an increase of the nucleation area in sharper tips accounts for the effect observed. A low nucleation field is a necessary prerequisite for the preparation of domain walls at comparably weak pinning sites as it is of interest for fundamental studies and applications.

5.2 Pinning of Domain Walls at an Anisotropy Boundary

In the last section the creation of domain walls in nanowires with perpendicular magnetic anisotropy has been discussed. As described at the beginning of Sec. 4.3 these domain walls can now be manipulated by fields or currents and act as information carrier in the context of new storage concepts. The analytical basis to describe the domain-wall dynamics has been introduced in the same section. But to obtain a fully functional storage devices, reliable pinning sites have to be taken into account. As dis-

cussed in Sec. 4.4 in nanowires with perpendicular magnetic anisotropy pinning can be realized by steps in the anisotropy. Bringing both the one-dimensional model and the pinning potentials for the domain wall together, results in a description of the field- or current driven domain-wall dynamics at an anisotropy boundary in a nanowire. Exactly this will be investigated in the following section. Micromagnetic simulations are performed to determine the fields and currents that are needed to depin the domain wall from the step in the anisotropy. The obtained data is subsequently compared to analytical calculations. Parts of this section have been published in Refs. [17] and [35].

The initial state of the simulation that is used as basis for determining the depinning field or current is characterized by two equal domains that are delimited by a Bloch wall as depicted in Fig. 5.7(a). The wall is thereby located in the center of an area of reduced anisotropy in a nanowire that is similar to Fig. 3.1. A small external field or current is then applied to drive the domain wall towards the K-step at the boundary between modified area and the rest of the nanowire, see Fig. 5.7(b). If the domain wall is pinned at the anisotropy boundary the field or current density is gradually increased until the domain wall is depinned.

The dimensions of the nanowire are $1280 \times 80 \times 5$ nm^3 and the area of reduced anisotropy has a length of 120 nm. It is extended across the whole width of the nanowire and along the length it is arranged centrally. One cell is $2.5 \times 2.5 \times 5$ nm^3 large and thus there is one cell in z-direction. The saturation magnetization is set to $M_s = 410 \times 10^3$ Am^{-1}, the anisotropy constant is $K_1 = 660 \times 10^3$ Jm^{-3}, and an exchange constant of $A = 30 \times 10^{-12}$ Jm^{-1} is chosen. All parameters are adopted from existing experimental material systems [140].

5.2.1 Field-driven Depinning of Domain Walls

In a first step the field-driven depinning of a domain wall from an anisotropy step is investigated. The above described nanowires and their initial setup are used and the Gilbert damping parameter is set to $\alpha = 0.2$. If a domain wall is driven by an external field it gets rotated, meaning the domain wall is transforming from a Bloch wall into Néel wall. But the rotation potential described in Sec. 4.4.2 counteracts the rotation due to the applied field leading to a steady motion of the domain wall with a certain azimuthal angle φ. At a critical external field – better known as Walker field [141] – the potential due to a rotation of the domain wall is overcome and the wall starts to fulfill full rotations. It then proceeds through the nanowire with a precessional motion, constantly transforming between a Bloch and a Néel wall. The velocity of the rotating domain wall is significantly lower than in the case of a steady motion.

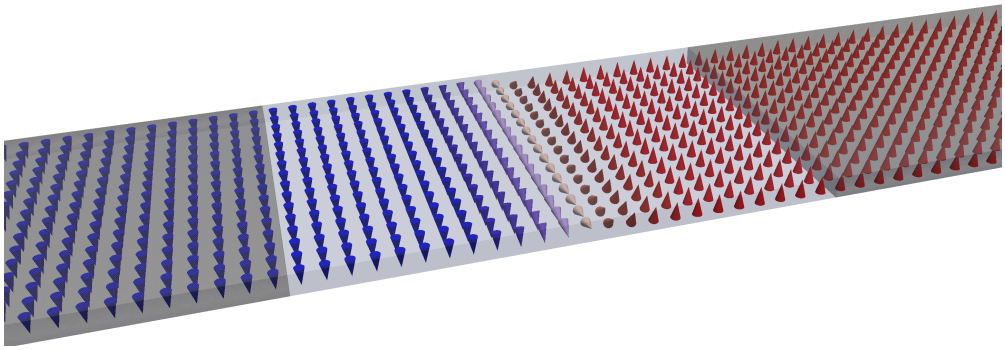

(a)

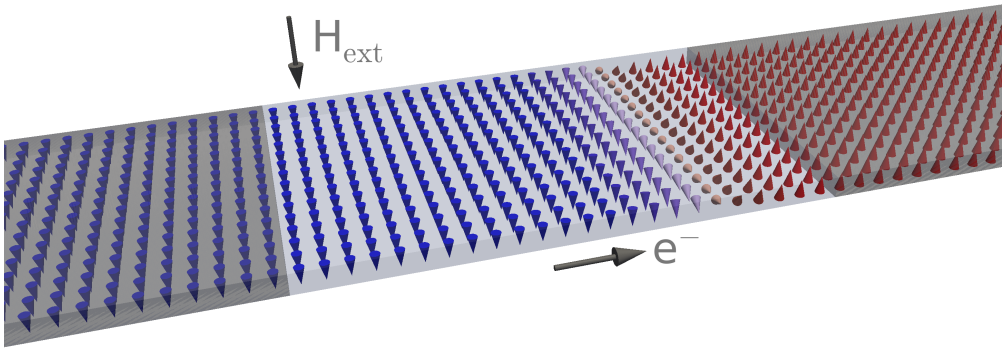

(b)

Figure 5.7: (a) In the initial setup a Bloch domain wall is located at the center of an area of reduced anisotropy (lighter area). (b) The applied field H_{ext} or the current density j drives the domain wall towards the right edge of the modified area where the anisotropy constant changes step-like (K-step). In addition the external forces induce a rotation of the domain wall.

Analytical Calculation of the Depinning Field

During the first approach of the domain wall to the K-step the applied fields are small and thus no rotational motion is observed. The high damping is hence justified and furthermore the domain wall can be assumed to be in rest prior to depinning. It is important to mention, that in contrast to the current-driven case, the deflection of the domain wall in the field-driven case depends on the domain-wall velocity and not on the applied field. To obtain an equation for the calculation of the depinning field it is hence reasonable to assume that the velocity and the precession are set to zero ($\dot{q} = 0, \dot{\varphi} = 0$). Since no current is applied ($u = 0$), inserting these assumptions and the potential due to the K-step given by Eqn. 4.4.4 into Eqn. 4.3.13 yields

$$H_{\text{ext}} = \frac{\Delta K}{2\mu_0 M_{\text{s}}} \operatorname{sech}^2\left(\frac{q}{a}\right) \tag{5.2.1}$$

where q is the position of the domain wall with respect to the anisotropy boundary and a is the wall's width. To determine the depinning field only the maximum values have to

be accounted for. Since this is the case if the domain-wall center is directly located at the K-step ($q = 0$) the depinning field is given by

$$H_{\text{dep}} = \frac{\Delta K}{2\mu_0 M_s}. \tag{5.2.2}$$

Exactly the same result has been obtained by H. Kronmüller and D. Goll using a simpler approach which neglects any kind of dynamics in the first place and describes the problem from an energetical point of view [142].

Depinning Field in the Simulation

The depinning field is investigated in dependence on the height ΔK of the anisotropy boundary the domain wall is depinned from. The height of the K-step is varied between 1% and 50% of the anisotropy constant in steps of 1% and the results of the analytical calculations and the simulations are depicted in Fig. 5.8. As can be seen and as expected from Eqn. 5.2.2 the depinning field depends linearly on the height ΔK. The agreement between the data obtained by simulations and the calculated values is very good. However, for an increasing height of the K-step the simulated depinning field tends to slightly higher values. A possible reason might be the stop criterion for the simulation, since it depends on the dynamics of the system. If the domain wall is pinned in front of a very steep potential barrier, a small increase of the external field might not induce enough dynamics to overcome the stop criterion. The simulation does not continue until the external field has been further increased. This explanation is confirmed by the fact that the difference between simulation and theory increases with increasing height of the K-step and hence with increasing steepness of the pinning potential. Nevertheless, the deviation is small and the results are in good agreement.

Potential during Depinning

Figure 5.9 depicts an exemplary potential energy E of the system as the domain wall passes an anisotropy boundary with the height $\Delta K = 20\%$ of the anisotropy constant K_1, obtained from simulations and by analytical calculations, see Eqn. 4.4.3. An energy offset is chosen such that the system with a relaxed Bloch wall in front of the K-step has zero energy. Hence it is possible to determine the increase of the system's energy during domain-wall depinning directly from the figure. The agreement between the energy obtained from simulation and the analytically determined energy is very good. The domain-wall width for the calculations has been taken from simulations.

Nevertheless, after the domain wall is depinned, the energies differ for $q > 10$ nm. Since the stray field is analytically calculated for a homogeneously magnetized sample without a domain wall, the resulting energy can be different from the simulated energy.

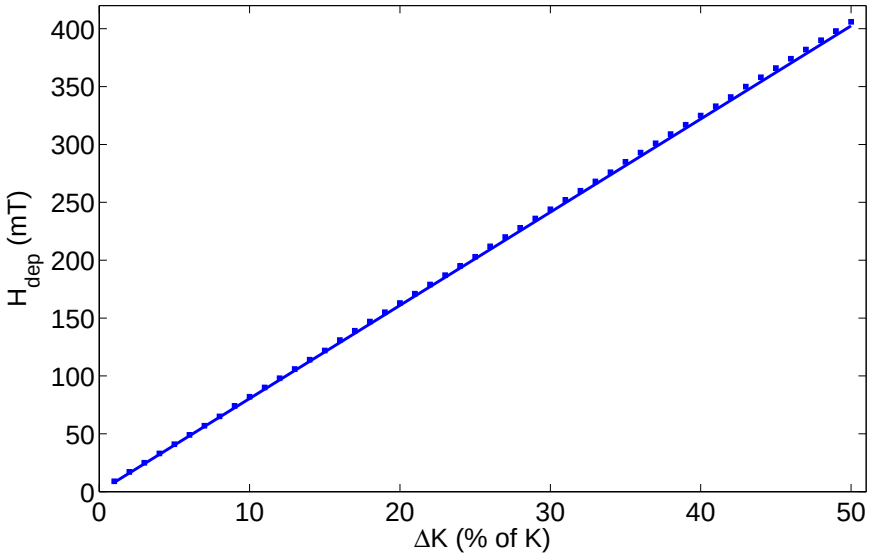

Figure 5.8: Depinning field H_{dep} of a Bloch domain wall in dependence on the height ΔK of a step in the anisotropy the wall is depinned from. The solid line represents the analytical solution of the depinning field whereas the symbols are the corresponding simulated values.

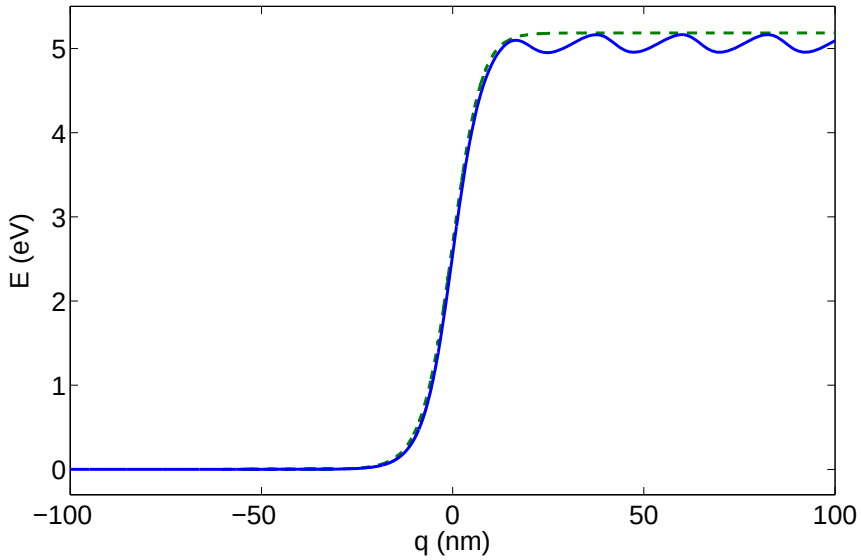

Figure 5.9: Exemplary potential energy E of the system in dependence on the domain wall position q as the wall passes a K-step of the height ΔK = 20%. An energy offset is chosen such that a relaxed Bloch wall in front of the anisotropy boundary has zero energy. The solid line represents the energy taken from the simulation whereas the dashed line is the analytically calculated energy.

Moreover, the dynamics of the system are not included in the analytical calculations. After the domain wall is depinned from the boundary, the applied external field is higher than the Walker field. Hence the domain wall is moving with a precessional motion through the nanowire which has an influence on the energy as well. This is indicated by the undulating characteristics of the energy obtained from simulations. However, for the description of the domain-wall dynamics with the one-dimensional model as introduced in Sec. 4.3 only the derivation of the potential energy with respect to the domain-wall position is of interest. And the agreement of the energies at $q = 0$ is excellent.

Conclusion

The one-dimensional model that is used to describe the field-driven depinning of a domain wall from a step in the anisotropy is perfectly suited for this task, the depinning fields are accurately determined. Depending on the height of the K-step high depinning fields can be achieved. Since they are even higher than the switching fields in round nucleation sites (cf. Fig. 5.2) for comparable reductions of the anisotropy constant this opens up the possibility to inject domain walls without switching the whole nanowire. However, in experiments the anisotropy would not change abruptly as assumed in the simulation but fade smoothly. As a result the slope of the pinning potential would be less steeper and hence the depinning fields would be lower. Aside from the depinning fields, the potential that is used to describe the pinning models the development of the energy of the system as the domain wall passes the K-step accurately. Thus it is suited to calculate the domain-wall dynamics at an anisotropy boundary with the one-dimensional q-φ-model.

5.2.2 Current-driven Depinning of Domain Walls

In the second part of the section the current-driven depinning of a domain wall that is pinned at an anisotropy boundary is investigated. As in the field-driven case, the nanowire and the initial setup described in the introduction of this section is used. In contrast to Sec. 5.2.1 a lower Gilbert damping parameter $\alpha = 0.02$ is set in order to reproduce the full magnetization dynamics, since it plays an important role during the depinning of the domain wall. Under the influence of a current flowing through the nanowire, the domain wall gets tilted as depicted in Fig. 5.7(b). Usually the applied currents that are needed to drive the domain wall in nanowires without pinning sites are small and result in a steady motion with a certain, constant rotation angle φ of the wall. For a critical current density the domain wall is subject to the well-known Walker breakdown as in the field-driven case. However, the current densities applied during the simulations are not the only reason for a rotational motion of the domain wall. There are other mechanisms as the interaction with a pinning potential that result in a rotation

of the domain wall as well, see Sec. 5.3. In the following the focus is on the current densities that are needed to depin the domain wall from a K-step.

Analytical Calculation of the Depinning Current

With the knowledge of the two contributions to the total energy barrier as described in Sec. 4.4 – the K-step, resulting in the pinning potential V_{pin}, and the rotation potential V_{rot} – it is possible to determine a threshold current density that is needed to depin the domain wall and drive it through the nanowire. During this process the barrier due to the anisotropy boundary only depends on the position q of the domain wall and is not affected by the rotation angle φ, whereas the potential that arises from the revolution of the domain wall is only rotation angle dependent and is not directly influenced by the domain wall position.

To calculate both threshold current densities $j_{\text{dep}}^{\text{rot}}$ and $j_{\text{dep}}^{\text{pos}}$ that are needed to depin the domain wall from the corresponding potentials it is feasible to assume that the wall is at rest prior to depinning and thus $\dot{q}(t) = 0$. Again, the one-dimensional q-φ-model introduced in Sec. 4.3 is used. Inserting Eqns. 4.3.15 and 4.4.4 into Eqns. 4.3.13 and 4.3.14 and substituting the domain-wall velocity $\dot{q} = 0$, the external field $H_{\text{ext}} = 0$, the current polarization $P = 1$, and the Landé factor $g = 2$ all together yields

$$\dot{\varphi} = \frac{\beta j \mu_{\text{B}}}{aeM_{\text{s}}} - \frac{\gamma \Delta K}{2\mu_0 M_{\text{s}}} \operatorname{sech}^2\left(\frac{q}{a}\right) \tag{5.2.3}$$

$$-\alpha\dot{\varphi} = \frac{\gamma K_{\perp}}{\mu_0 M_{\text{s}}} \sin 2\varphi + \frac{j\mu_{\text{B}}}{aeM_{\text{s}}}. \tag{5.2.4}$$

Combining both equations by inserting $\dot{\varphi}(t)$ from Eqn. 5.2.3 in Eqn. 5.2.4 results in

$$j = \frac{ae\gamma}{\mu_0 \mu_{\text{B}}(1+\alpha\beta)} \left(\frac{\alpha \Delta K}{2} \operatorname{sech}^2\left(\frac{q}{a}\right) - K_{\perp} \sin(2\varphi) \right). \tag{5.2.5}$$

Thus two different terms that contribute to the current density can be distinguished:

$$j^{\text{I}}(\varphi) = -\frac{ae\gamma}{\mu_0 \mu_{\text{B}}(1+\alpha\beta)} K_{\perp} \sin(2\varphi) \tag{5.2.6}$$

$$j^{\text{II}}(q) = \frac{ae\gamma\alpha}{2\mu_0 \mu_{\text{B}}(1+\alpha\beta)} \Delta K \operatorname{sech}^2\left(\frac{q}{a}\right). \tag{5.2.7}$$

The first term $j^{\text{I}}(\varphi)$ is correlated with the revolution of the domain wall and only depends on the rotation angle φ. If no K-step is present it determines the current density that has to be applied to rotate up to a certain angle and will be referred to as rotation current density $j^{\text{rot}}(\varphi)$. Likewise, the second term is called position current density $j^{\text{pos}}(q)$ and defines how far the domain wall can be moved at a certain current density while no revolution of the magnetic moments is taken into account.

The depinning current densities that have to be applied to overcome the two corresponding energy barriers can be determined if the values that result in a maximum slope of the potential are known. For $\partial V_{\text{rot}}/\partial\varphi$ this is the case for $\varphi = -\pi/4$ and inserting into Eqn. 5.2.6 yields

$$j_{\text{dep}}^{\text{rot}} = \frac{ae\gamma}{\mu_0\mu_{\text{B}}(1+\alpha\beta)}K_{\perp}. \tag{5.2.8}$$

The resulting depinning current density $j_{\text{dep}}^{\text{rot}}$ depends linearly on the effective rotation anisotropy $K_{\perp}$ that stems from the different stray fields of a Bloch and a Néel wall. Once the energy barrier is overcome the domain wall rotates continuously.

Since the slope $\partial V_{\text{pin}}/\partial q$ of the position-dependent energy barrier is maximal if the domain wall is located at $q = 0$, the current density that is needed to depin the domain wall from the step in the anisotropy constant K_1 can be calculated by

$$j_{\text{dep}}^{\text{pos}} = \frac{ae\gamma\alpha\Delta K}{2\mu_0\mu_{\text{B}}(1+\alpha\beta)}. \tag{5.2.9}$$

Again, a linear behavior of the depinning current density $j_{\text{dep}}^{\text{pos}}$ on the height ΔK of the K-step can be observed. Thus in experiments the pinning potential can be tailored to achieve a desired depinning current density. If the domain wall is depinned it proceeds undisturbed through the rest of the nanowire.

Depinning Current in the Simulations

During the simulations a domain wall is placed inside an area of reduced anisotropy. Then a current is applied and the domain wall is driven towards a K-step where it gets pinned. The current density is gradually increased until the domain wall depins and the so determined depinning current density j_{dep} has its origin in the two different potential barriers. The barrier due to the rotation of the domain wall stems from the different stray field energies of the magnetic configuration of a Bloch and a Néel wall. Since this is an intrinsic characteristic of the investigated system this kind of pinning is referred to as intrinsic pinning. In addition to the intrinsic energy barrier the domain wall gets pinned at the anisotropy boundary that is of artificial origin. Thus this type of pinning is called extrinsic pinning.

As depicted in Fig. 5.10 the analytically obtained depinning current density coincides almost perfectly with the simulated values. Up to a height $\Delta K = 40\%$ of the K-step, intrinsic pinning is dominant. The rotation depinning current density j_{dep}^{rot} that is needed to overcome the rotation potential is higher than the K-step depinning current density $j_{\text{dep}}^{\text{pos}}$ that is needed to overcome the anisotropy boundary. For higher K-steps with $\Delta K > 40\%$ the extrinsic pinning is predominant. In the intrinsic regime the depinning current density j_{dep} decreases with increasing height ΔK of the K-step. An explanation

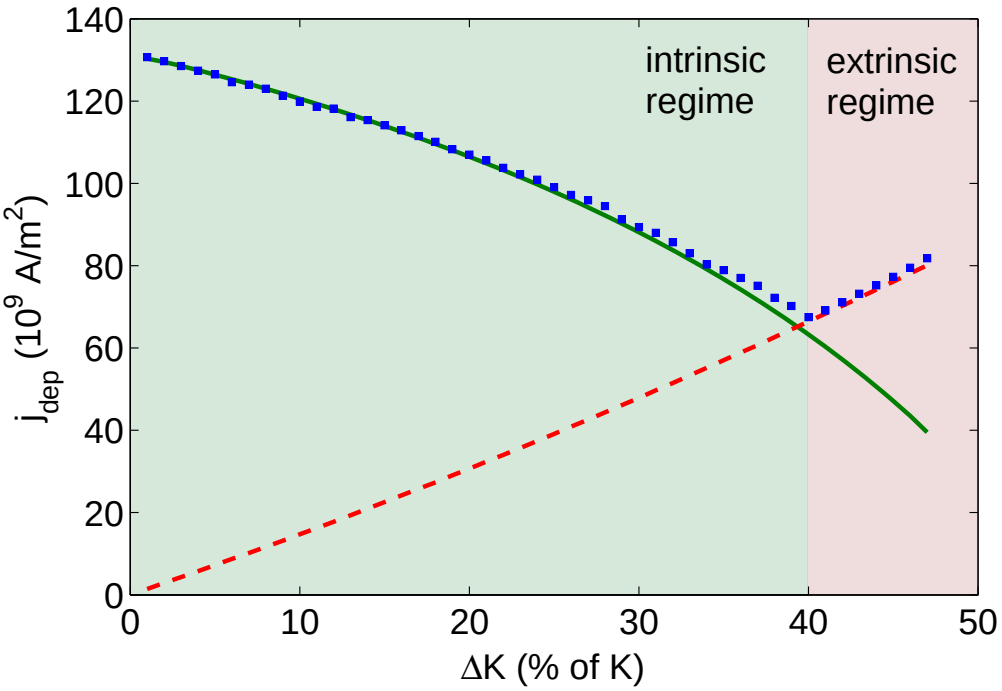

Figure 5.10: Depinning current density j_{dep} in dependence on the height ΔK of the step in the anisotropy constant (blue symbols – micromagnetic simulations). Up to ΔK = 40% the depinning current density is dominated by the intrinsic pinning due to the rotation-energy barrier (solid green line – analytical calculation). Thereby j_{dep} decreases slightly with increasing height ΔK. For a K-step higher than 40% of the anisotropy constant the depinning current density j_{dep} is determined by the extrinsic pinning due to the anisotropy boundary and depends linearly on the boundary height ΔK (dashed red line – analytical calculation).

for this dependence is the reduction of the anisotropy constant K_1 in the modified area to increase ΔK. Since the width a of the Bloch wall, which is initially placed here, is increased with lower anisotropy the energy due to the stray field of a Bloch wall increases as well. This in turn reduces the energy barrier due to the transition from a Bloch to a Néel wall, which results in a lowered effective rotation anisotropy $K_\perp$. In the extrinsic regime the depinning current density j_{dep} depends almost linearly on the height ΔK of the K-step as described in Eqn. 5.2.9. A slight deviation from the linearity is observed and can be explained with the increased domain-wall width a, since j_{dep}^{pos} is linear in a as well.

Figure 5.10 also reveals that both regimes seem to be decoupled, because there is a very sharp transition between both regimes. To explain this behavior it is necessary to determine the position q of the domain wall when it is pinned due to the rotation potential. From the q-φ-model it can be deduced that the rotation angle φ not only depends on the applied current but on the potential barrier of the K-step as well, see Sec. 5.3. Interestingly the impact due to the barrier on the rotation angle is significantly higher

than the impact due to the current density j. Far from the anisotropy boundary the domain wall gets tilted up to a certain angle and moves steadily through the nanowire due to the initially applied small current. Once the wall approaches the anisotropy boundary and starts to barely feel the potential, the rotation angle φ has to increase drastically which forces the domain wall into rotation. In the intrinsic regime the initially applied current might be large enough to push the domain wall into and even above the K-step but it is not large enough to overcome the rotation barrier. The domain wall is thus pinned at a large distance from the anisotropy boundary and the potential due to the K-step has only a minor influence and can be neglected to calculate the depinning current density. If the height ΔK of the K-step is increased and the transition region between intrinsic and extrinsic regime is investigated ($\Delta K = 30\% - 40\%$), the pinning position of the domain wall is moved slightly towards the K-step. The potential due to the boundary is not negligible anymore and adds to the rotation potential. Thus the simulated depinning current densities j_{dep} slightly deviate from the analytically determined values – they are a little higher.

In the extrinsic regime the rotation barrier already has been overcome and the applied current density is $j > j_{\text{dep}}^{\text{rot}}$. The domain wall is rotating with a certain frequency $f_{\text{rot}} > 0$ and energy is only transferred between the stray-field energy (static) and the rotation energy of the domain wall (dynamic). The influence of the rotation potential reduces with an increasing rotation frequency of the domain wall since the relative height of the static energy barrier gets negligible in comparison with the dynamic rotation energy. For high frequencies f_{rot} in the order of several GHz – which is the usual case in the extrinsic regime – it is then feasible to consider the time average of the rotation:

$$\langle \sin(2\varphi) \rangle = \frac{1}{T} \int_0^T \sin(2\varphi)\, \mathrm{d}t \approx 0. \tag{5.2.10}$$

Thus in the extrinsic regime the influence of the rotation potential vanishes and the depinning-current density is only determined by the potential due to the K-step. As can be seen in Fig. 5.10 there is a perfect agreement between simulated and calculated values for the depinning current density.

Conclusion

The depinning of a current-driven domain wall with an anisotropy boundary in a nanowire with perpendicular magnetic anisotropy has been investigated by micromagnetic simulations and analytical calculations. It has been found that the depinning-current density depends on the height ΔK of the K-step and two regimes of pinning can be distinguished. In the intrinsic regime up to $\Delta K = 40\%$ of the anisotropy constant in the nanowire the domain wall is pinned at a barrier due to a difference in the stray-field energy of the magnetic configurations of a Bloch and a Néel wall. In the extrinsic regime

the depinning-current density is determined by the height ΔK of the anisotropy boundary and thus the height of the resulting potential barrier. Since the positions q where the domain wall gets pinned are spatially decoupled for both regimes, there is a very sharp transition between both regimes. A very good accordance between analytical calculations based on the q-φ-model and micromagnetic simulations performed with MicroMagnum are achieved.

5.3 Interaction of the Domain Wall with the Boundary

In the preceding section it has been noted, that the applied current is not the only reason leading to a rotation of the domain wall. Although the current is the driving force behind the domain-wall movement, its characteristic is also determined by an interaction between the domain wall and the anisotropy boundary in the nanowire. This interaction not only has an influence on the rotation frequency of the domain wall, but results in higher excitations of certain parameters of the wall as well. However, these characteristics can be made use of to create e.g. spin-torque nano-oscillators [143]. In the following the interaction of domain wall and K-step will be discussed in detail.

5.3.1 Rotation of the Domain Wall

In the intrinsic pinning regime as described in Sec. 5.2.2 the domain wall gets pinned due to a prevention of rotation at the rotation potential V_{rot}. The actual reason for the rotation of the domain wall is not obvious. As will be deduced in the following from the one-dimensional model that is employed to describe the domain-wall dynamics, the pinning potential due to the anisotropy step is responsible for the rotation of the domain wall.

Analytical Calculation of the Rotation Angle

To determine the impact of the anisotropy boundary on the domain wall, the q-φ-model is used to determine the rotation angle φ and the rotation frequency $f_{\text{rot}} = \dot{\varphi}/2\pi$ of the wall in dependence on the applied current density j. Therefor the wall velocity $\dot{q}$ from Eqn. 4.3.13 is substituted in Eqn. 4.3.14 which yields the differential equation

$$A + B\sin(2\varphi) + C\dot{\varphi} = 0 \tag{5.3.1}$$

with

$$A = (\alpha - \beta)\frac{j\mu_B}{aeM_s} + \frac{\gamma\Delta K}{2\mu_0 M_s}\text{sech}^2\left(\frac{q}{a}\right) \quad (5.3.2)$$

$$B = \frac{\alpha\gamma K_\perp}{\mu_0 M_s} \quad (5.3.3)$$

$$C = 1 + \alpha^2. \quad (5.3.4)$$

Regime of Steady Domain Wall Movement

For an applied current with a density $j < j_{dep}^{rot}$ (see Eqn. 5.2.8) the domain wall does not rotate. Hence in this steady regime of movement the angular velocity $\dot{\varphi}$ can be assumed to be zero. The rotation angle of the current-driven domain wall in the nanowire is thus described by

$$\varphi = -\frac{1}{2}\arcsin\left(\frac{(\alpha - \beta)j\mu_0\mu_B}{ae\alpha\gamma K_\perp} + \frac{\Delta K}{2\alpha K_\perp}\text{sech}^2\left(\frac{q}{a}\right)\right). \quad (5.3.5)$$

As already pointed out in Sec. 5.2.2, far from the anisotropy boundary the domain wall gets tilted up to a certain angle and moves steadily through the nanowire due to the initially applied small current. In this case the rotating force due to the current is in equilibrium with the restoring force due to the rotation potential V_{rot} and the rotation frequency is $f_{rot} = 0$. But once the wall approaches the anisotropy boundary and starts to barely feel the potential, the rotation angle φ has to increase drastically which forces the domain wall into rotation, since

$$\frac{(\alpha - \beta)j\mu_0\mu_B}{ae\alpha\gamma K_\perp} \ll \frac{\Delta K}{2\alpha K_\perp}\text{sech}^2\left(\frac{q}{a}\right), \quad (5.3.6)$$

even for small steps in the anisotropy and for a large distance of the wall from the boundary, compared to the domain-wall width. The wall thus gets pinned until higher currents are applied.

Regime of Rotational Domain-Wall Movement

If currents with a density $j > j_{dep}^{rot}$ are applied to depin the domain wall from the rotation potential V_{rot}, the wall is in a rotational motion and precesses with a certain frequency $f_{rot} > 0$. As discussed at the end of Sec. 5.2.2 in this regime the influence of the energy barrier due to the different stray-field energies of the domain walls can be neglected. The temporal evolution of the rotation angle φ is then very close to a sinusoidal evolution resulting in $\langle\sin(2\varphi)\rangle \approx 0$ (see Eqn. 5.2.10). Thus if the time average is investigated for a rotating domain wall the differential equation 5.3.1 reduces to

$$A + C\dot{\varphi} = 0. \quad (5.3.7)$$

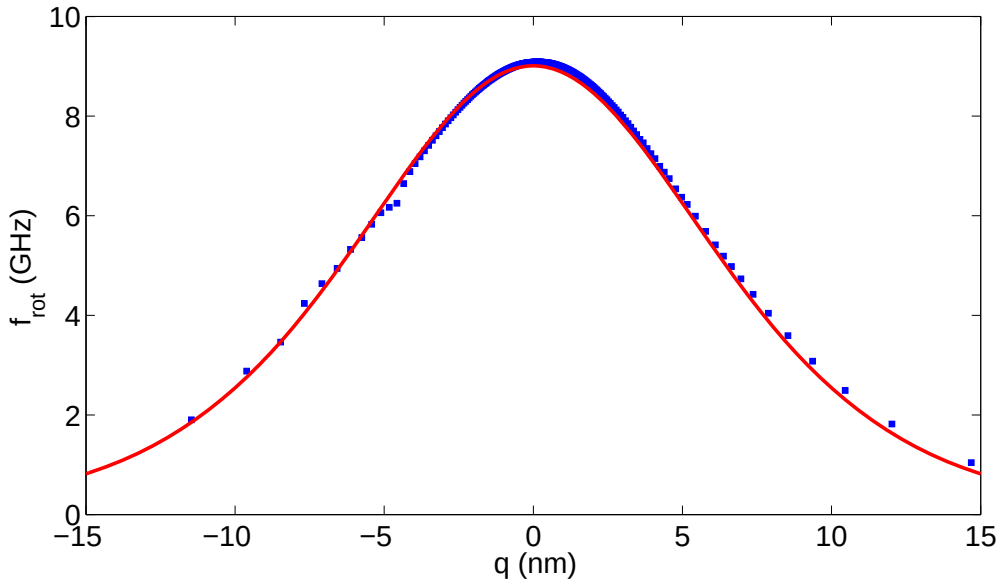

Figure 5.11: Exemplary rotation frequency f_{rot} in dependence on the domain-wall position q. The step in the anisotropy constant is located at $q = 0$ and has a height of $\Delta K = 40\%$ of the anisotropy constant K_1. The red solid line represents the analytically obtained data, while the blue symbols are the corresponding simulated values.

From this equation the rotation frequency $f_{\mathrm{rot}} = \dot{\varphi}/2\pi$ can be determined for a given position q of the domain wall:

$$f_{\mathrm{rot}} = \frac{(\alpha - \beta)\frac{j\mu_{\mathrm{B}}}{aeM_{\mathrm{s}}} + \frac{\gamma \Delta K}{2\mu_0 M_{\mathrm{s}}}\mathrm{sech}^2\left(\frac{q}{a}\right)}{2\pi(1+\alpha^2)}. \tag{5.3.8}$$

If the applied current density j is in the order of the current densities used in the simulations and in comparable experiments ($j \approx 10^{11}$ Am^{-2}, cf. Ref. [140]), the rotation frequency f_{rot} of the domain wall is in the vicinity of the anisotropy step dominated by its position, because

$$(\alpha - \beta)\frac{j\mu_{\mathrm{B}}}{aeM_{\mathrm{s}}} \ll \frac{\gamma \Delta K}{2\mu_0 M_{\mathrm{s}}}\mathrm{sech}^2\left(\frac{q}{a}\right), \tag{5.3.9}$$

meaning the influence of the current on the frequency is negligible in comparison with the influence of the anisotropy boundary. Note, that the sole existence of the anisotropy boundary is sufficient to cause a rotation of the domain wall and that the torque due to the non-adiabaticity of the current only plays a minor role for the frequency. Nevertheless, the rotation frequency is indirectly controlled by the applied current via the domain-wall position.

Rotation Frequency in the Simulations

Simulations performed for the determination of the current-driven domain-wall depinning have been analyzed with respect to the rotation frequency f_{rot} in dependence

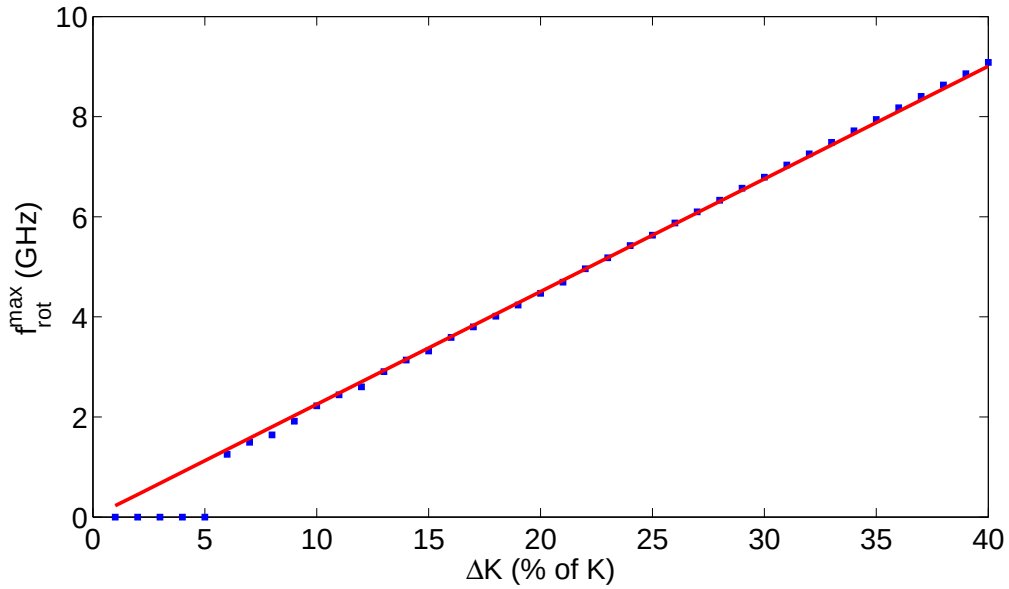

Figure 5.12: Maximum rotation frequency f_{rot}^{max} in dependence on the height ΔK of the K-step. The domain wall rotates with maximum frequency if it is located directly at the anisotropy boundary at $q = 0$. For very small boundary heights there are too few revolutions of the domain wall to determine a reasonable value for the rotation frequency. The red solid line represents the analytically obtained data, while the blue symbols are the corresponding simulated values.

on the position q of the domain wall. As exemplarily depicted in Fig. 5.11 the frequencies follow the development of the derivative of the pinning potential $\partial V_{pin}/\partial q = \Delta K \mathrm{sech}^2(q/a)$ as expected from Eqn. 5.3.8. An influence on the rotation due to the current is not noticeable.

The rotation frequency has its maximum value when the domain wall is directly located at the center of the anisotropy boundary at $q = 0$. From Eqn. 5.3.8 thus a linear dependence of the maximum rotation frequency f_{rot}^{max} on the height ΔK of the K-step is expected and Fig. 5.12 affirms the expectations to be true. Only for small steps in the anisotropy constant no rotation frequencies can be obtained from the simulation, since too few rotations occur to determine reasonable values. Aside from that, all the values obtained from the simulations are in very good agreement with the analytical calculations for both, the rotation frequency f_{rot} and the maximum rotation frequency f_{rot}^{max} if the domain wall is located at the center of the K-step.

Conclusion

The anisotropy boundary forces the domain wall to rotate and results in the existence of two depinning regimes. Without this interaction the depinning currents would be linear in the height ΔK of the K-step and the domain wall would only undergo a rotational

motion for $\Delta K > 40\%$ of the anisotropy constant. The interaction results in a domain-wall rotation with rather high frequencies, that depend on the maximum slope of the pinning potential V_{pin}. Again, the one-dimensional q-φ-model is employed to accurately describe the dynamics of a domain wall at an anisotropy boundary.

5.3.2 Higher Excitations of the Domain Wall

As described in the last section the domain wall is rotating with a certain frequency f_{rot} while it is driven through the energy barrier, see Eqn. 5.3.8, and the frequency mainly depends on the distance of the domain wall to the step in the anisotropy constant. During its rotation the domain wall is constantly transforming between a Bloch and a Néel wall. The stray-field configurations and therewith the stray-field energy of both wall types are different. While the energy due to a Bloch wall is determined by surface charges at the edge of the nanowire, the stray-field energy of a Néel wall depends on corresponding volume charges inside the nanowire. Since the amount of surface charges of a Bloch wall depends linearly on the domain-wall width a, the energy of the system is minimized, if the domain-wall width of a Bloch wall is decreased. In contrast, for the Néel wall a smoother transition of the magnetization and thus a wider domain-wall results in less volume charges and thereby less stray-field energy. Hence in the same nanowire a Bloch wall has a smaller domain-wall width then a Néel wall. The constant transformation of the domain-wall type thus results in an oscillating domain-wall width as well. Based on Eqn. 4.1.9 the domain-wall width can be estimated as

$$a = \sqrt{\frac{A}{K_{\text{eff}} - K_{\perp} \sin^2 \varphi}}. \tag{5.3.10}$$

The oscillation of the domain-wall width is a direct consequence of the rotation of the domain wall. The resulting frequency f_{width} of the width oscillation thus equals the rotation frequency of the domain wall, meaning $f_{\text{width}} = f_{\text{rot}}$. Furthermore, the width oscillation and the domain-wall rotation are in phase.

Doubled Frequency of the Width Oscillation

Figure 5.13 depicts an extract of an ongoing simulation in the extrinsic regime ($\Delta K =$ 45% of the anisotropy constant K_1). The width a and the position q of an already rotating domain wall are shown with respect to the simulation time. The applied current density is held constant during this extract. Due to the applied current the domain wall is driven towards the K-step at $q = 0$ and as known from the Walker breakdown it is moving slightly back and forth as it rotates. The corresponding domain-wall width-oscillation is absolutely in phase with the wall rotation. If the applied current density j exceeds a certain value, the domain wall gets into a higher excitation. In this special

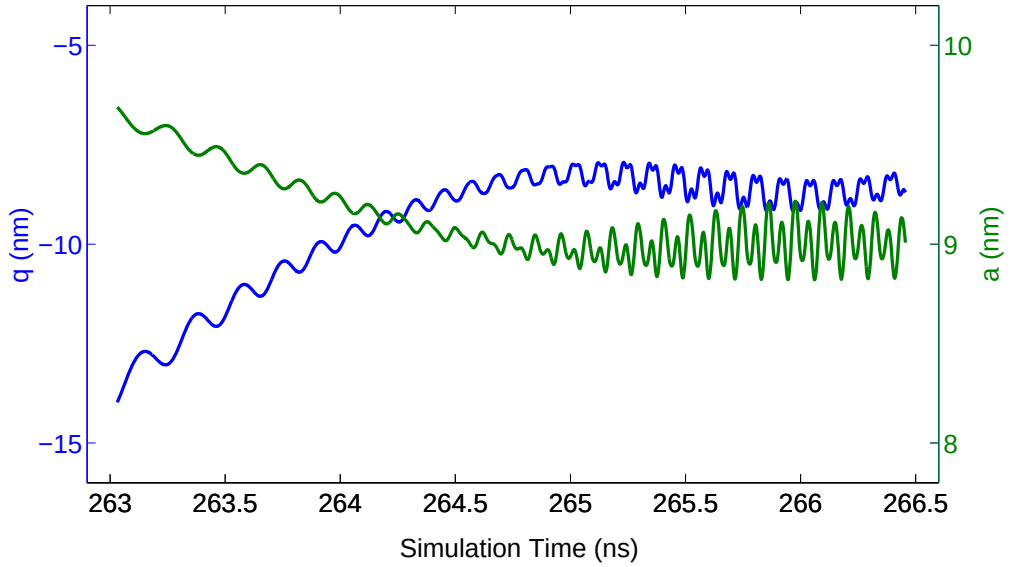

Figure 5.13: Domain-wall position q (blue line) and the domain-wall width a (green line) during an extract of an ongoing simulation in the extrinsic regime. The applied current density j is held constant over the shown extract. If it is high enough, the domain wall gets into a higher excitation and the width starts to oscillate with a doubled frequency $f'_{\mathrm{width}} = 2 \cdot f_{\mathrm{width}}$ while the rotation frequency f_{rot} remains. Due to this behavior the domain wall gets pinned.

case this is expressed by the fact, that the domain-wall width starts to oscillate with a doubled frequency $f'_{\mathrm{width}} = 2 \cdot f_{\mathrm{width}} = 2 \cdot f_{\mathrm{rot}}$ as depicted in Fig. 5.13. In contrast, the rotation frequency f_{rot} of the domain wall does not change. Moreover, the domain wall stops moving forward – and gets pinned.

Pinning of the Domain Wall

This pinning is illustrated in Fig. 5.14. The development of the domain-wall position q and the rotation frequency f_{rot} is shown after the domain wall has started to rotate during a simulation. The applied current density is gradually increased during the depicted extract. After the domain wall starts to rotate it is moving with a rather high domain-wall velocity (which is connected with an increasing rotation frequency, see Sec. 5.3.1). About 8 nm in front of the anisotropy boundary the domain wall gets pinned. Although the current is increased during the ongoing simulation, the domain wall does not move and the rotation frequency f_{rot} does not change as well, whereas the frequency f_{width} of the width oscillation is doubled due to the higher excitation of the domain wall. The actual frequency of the domain-wall width-oscillation f_{width} before and after the pinning is depicted in Fig. 5.15. A Fourier transformation has been performed to characterize the width oscillation. Before the pinning of the domain wall at $q \approx -8$ nm the width oscillates in the first harmonic in phase with the domain-wall rotation. After the pinning

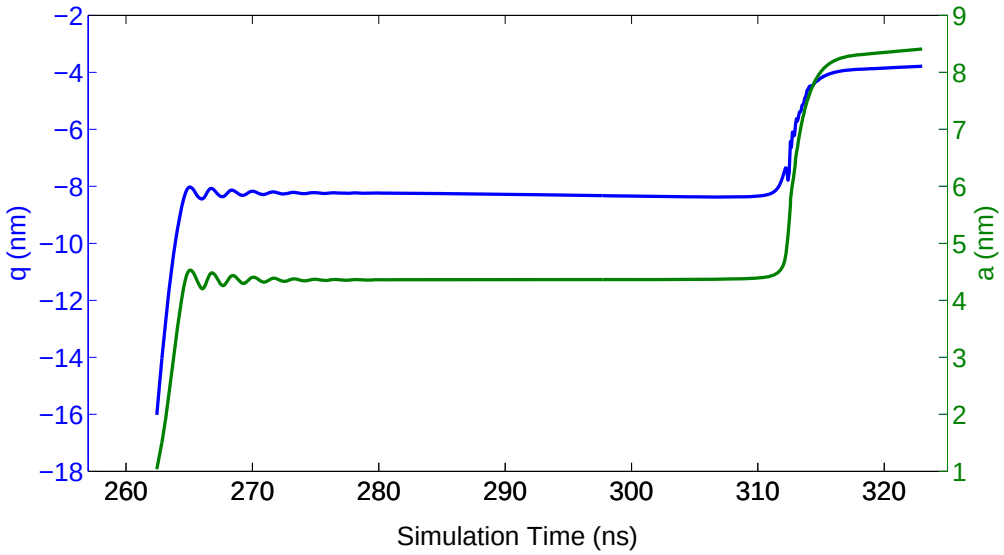

Figure 5.14: Average domain-wall position q (blue line) and the rotation frequency f_{rot} of the domain wall (green line) during an ongoing simulation. The domain wall gets pinned about 8 nm in front of the anisotropy boundary and while it is pinned, the rotation frequency f_{rot} remains constant whereas the width-oscillation frequency f_{width} doubles. The applied current is increased during the ongoing simulation and it has to be increased drastically in order to depin the domain wall again. This results in a significant jump in the position and frequency of the domain wall.

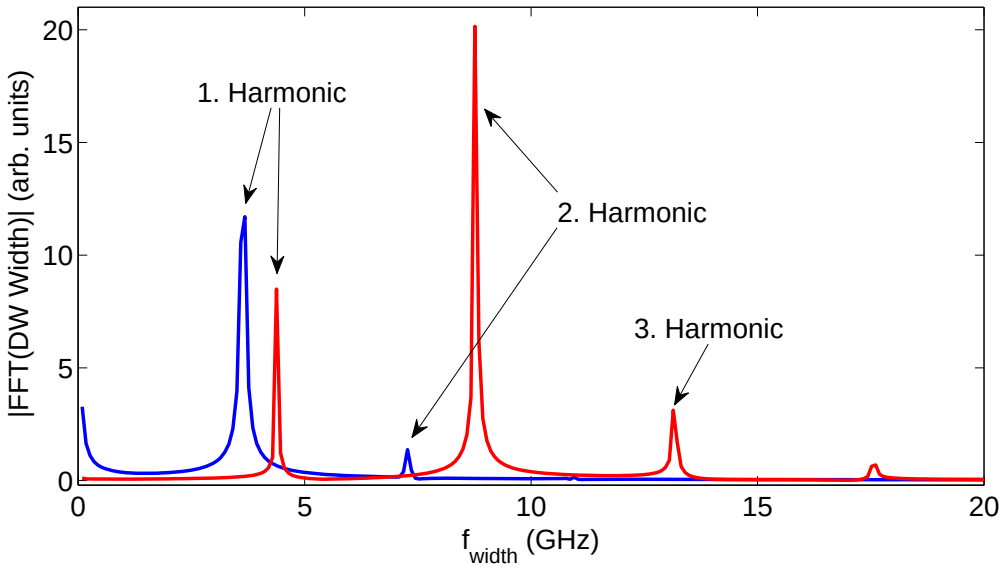

Figure 5.15: Fourier-transformed signal of the domain-wall width-oscillation in dependence on the oscillation frequency. Before the domain wall gets pinned (blue line) the domain-wall width oscillates in phase with the rotation angle of the domain wall. After the domain wall gets pinned about 8 nm in front of the anisotropy boundary (red line) the domain-wall width oscillates with doubled frequency $f'_{\text{width}} = 2 \cdot f_{\text{width}} = 2 \cdot f_{\text{rot}}$ and is hence in a higher excitation indicated by the second harmonic.

(and after a slight increase of the first harmonic frequency due to the domain-wall displacement) the domain-wall width oscillates mainly in the second harmonic and thus with doubled frequency $f'_{\text{width}} = 2 \cdot f_{\text{width}} = 2 \cdot f_{\text{rot}}$. But the rotation frequency f_{rot} of the domain wall remains constant, see Fig. 5.14. The pinning of the domain wall is hence correlated with the higher excitation that is expressed in the doubled frequency of the width-oscillation.

Depinning from the Frequency Blockade

To depin the domain wall from this additional pinning state the current density has to be drastically increased. As depicted in Fig. 5.14 the depinning results in a significant jump of the domain-wall position q and thereby an increase of the rotation frequency f_{rot} to about a doubled rotation frequency $f'_{\text{rot}} = 2 \cdot f_{\text{rot}}$. This indicates the reason for the pinning can be found in a blockade of the development of the rotation frequency. Usually an increasing current density pushes the domain wall further into the K-step, leading to an increased frequency of the rotation. However, the rotation of the domain wall has to be in phase with the wall-width oscillation, which is the case if the rotation frequency is a multiple of the width-oscillation frequency $f_{\text{rot}} = n \cdot f_{\text{width}}$ or vice versa. Due to the higher excitation of the domain wall the width oscillation has a doubled frequency f'_{width}. Thus the rotation frequency does not increase and is blocked until the applied current density is high enough to push the wall instantaneously to a position with doubled rotation frequency $f'_{\text{rot}} = 2 \cdot f_{\text{rot}}$, which results in the jump of q and f_{rot} in Fig. 5.14. The jump overcomes the frequency blockade – the width oscillation and the domain-wall rotation are in phase again with the frequencies $f'_{\text{width}} = f'_{\text{rot}}$. The wall is then further driven through the K-step with a normally evolving rotation frequency as depicted in Fig. 5.11. The frequency blockade only occurs for high steps in the anisotropy ($\Delta K \gtrsim 45\%$ of K_1) since then the achieved current densities are high enough to excite the domain wall.

Conclusion

Aside from the rotation of the domain wall due to the anisotropy boundary there is more interaction of the wall with the K-step. Although the doubled frequency of the wall-width oscillation and thereby the frequency blockade is a result of the high current densities applied through the nanowire, it is the dependence of the rotation frequency f_{rot} on the pinning potential V_{pin} at the domain-wall position q – and hence the step in the anisotropy constant – that causes this interesting behavior. However, the simulation describes an ideal case with a perfect nanowire. In experiments the applied currents are expected to be smaller due to a smoother transition of the anisotropy constant across the boundary.

Chapter 6

Summary and Outlook

After a detailed theoretical basis in form of the micromagnetic model with its central equation – the Landau-Lifshitz-Gilbert equation extended by spin polarized currents – is established, the investigated material system and micromagnetic simulations are introduced in detail. Domain walls and its fundamental characteristics in nanowires with perpendicular magnetic anisotropy are discussed. On this basis theoretical models that are suited for the description of the domain-wall creation and its dynamics in nanowires with intentional modifications of the anisotropy constant are developed. To calculate the switching fields in artificial nucleation sites the linearized micromagnetic equations are introduced and eigenmode analysis is employed. The one-dimensional q-φ-model, which is based on the collective coordinates domain-wall position q and azimuthal angle φ is derived to describe the field- and current-driven domain-wall motion in a nanowire. The specific potentials that are connected with the domain-wall dynamics and hence with the collective coordinates are calculated. These are the pinning potential V_{pin} at the anisotropy boundary and the rotation potential V_{rot} due to the difference in the stray-field energies of a Bloch and Néel wall.

Micromagnetic simulations are performed in order to compare the analytical calculations with a system that takes the full magnetization dynamics into account. In a first part of the comparison the creation of domain walls is discussed. Both analytical calculations and simulations show with an excellent agreement that the switching field of a nanowire can be significantly decreased by the introduction of a nucleation site with reduced anisotropy constant. Based on these findings simulations are performed to investigate an unexpected switching behavior in experiments involving nanowires with perpendicular magnetic anisotropy. It turns out that in wires with tip ends the nucleation takes place in the tip which can be explained – in accordance with simulations – by the reduction of the anisotropy constant during the preparation process. In the second part the field- and current-driven depinning from an anisotropy boundary is discussed. For the field-driven case analytical calculations deduced from the one-dimensional q-

φ-model reveal depinning fields that are in perfect agreement with the corresponding values obtained by simulations. The calculated pinning potential is absolutely conform with the energy barrier observed during simulations. The depinning of the domain wall in the current-driven case is more complex – the two different potentials result in two pinning regimes with very different depinning current densities. However, calculations based on the q-φ-model yield the same results as can be obtained from the simulations. As the domain wall is driven through the anisotropy boundary by current, it interacts with the pinning potential which is discussed in a last part of this chapter. The frequency of the domain-wall rotation directly depends on the slope of the pinning potential due to the K-step at the domain-wall position q. The frequencies obtained by simulations perfectly coincide with the values of analytical calculations. Another interesting interaction that can be observed is the domain-wall pinning due to a frequency blockade of the rotation due to a higher excitation of the domain-wall width-oscillation.

Altogether the theoretical work and the simulations performed in the course of this thesis contribute to the investigation of the crucial prerequisites that have to be resolved to realize a new kind of storage device. In this context the material system of nanowires with perpendicular magnetic anisotropy and a local intentional modification of the anisotropy constant is investigated. It is shown that the approach of reducing the anisotropy constant in order to create artificial nucleation and pinning sites is perfectly suited to manipulate the domain-wall dynamics. The switching fields are reduced and the nucleation is localized. Furthermore, reliable pinning sites can be created by controllable preparation techniques. Although experiments on the field-driven depinning of domain walls from a step in the anisotropy have been recently conducted, investigations on the interaction of a current-driven domain wall with the anisotropy boundary in real samples are still pending. In the opinion of the author, especially the reduction of the anisotropy by the application of electric fields, which would enable a switch for the pinning sites, is a very promising approach to realize the racetrack memory.

Appendix A

Further Investigations

During the work for this thesis nanowires with perpendicular magnetic anisotropy were not the only material system that has been investigated. The pinning of field-driven domain walls in permalloy nanowires has been studied, too. Although permalloy does not comprise a particular anisotropy, the energy landscape that a moving domain wall feels can be tailored as well. This is achieved by a local modification of the saturation magnetization referred to as magnetic soft spots. However, this topic is not included in the thesis since a different material system demands for a quite different discussion of the results and that would be beyond the scope of the presented work. Nevertheless, the investigations on domain-wall motion in permalloy resulted in the following publication:

"Field- and current-induced domain-wall motion in permalloy nanowires with magnetic soft spots",

A. Vogel, S. Wintz, T. Gerhardt, L. Bocklage, T. Strache, M.-Y. Im, P. Fischer, J. Fassbender, J. McCord, and G. Meier,

Appl. Phys. Lett. **98**, 202501 (2011).

The numbers by which citations are referenced in the following article are only valid within the article.

APPLIED PHYSICS LETTERS **98**, 202501 (2011)

Field- and current-induced domain-wall motion in permalloy nanowires with magnetic soft spots

Andreas Vogel,[1,a)] Sebastian Wintz,[2] Theo Gerhardt,[1] Lars Bocklage,[1] Thomas Strache,[2] Mi-Young Im,[3] Peter Fischer,[3] Jürgen Fassbender,[2] Jeffrey McCord,[2] and Guido Meier[1]

[1]*Institut für Angewandte Physik und Zentrum für Mikrostrukturforschung, Universität Hamburg, 20355 Hamburg, Germany*

[2]*Institut für Ionenstrahlphysik und Materialforschung, Helmholtz-Zentrum Dresden-Rossendorf, 01314 Dresden, Germany*

[3]*Center for X-ray Optics, Lawrence Berkeley National Laboratory, Berkeley, California 94720, USA*

(Received 5 April 2011; accepted 21 April 2011; published online 16 May 2011)

We study field- and current-induced domain-wall motion in permalloy nanowires containing a square-shaped magnetically softened region. Implantation of chromium ions is used to induce pinning sites via a local reduction in the saturation magnetization. Micromagnetic simulations, magnetic transmission soft x-ray microscopy, and electrical measurements are employed to characterize the pinning potential which significantly differs for transverse and vortex walls. Reliable domain-wall depinning from a so-called magnetic soft spot by single current pulses is observed. This demonstrates the suitability of these pinning sites for applications. © *2011 American Institute of Physics*. [doi:10.1063/1.3590267]

Recent concepts of high-density and ultrafast nonvolatile data storage devices involve the controlled motion of magnetic domain walls (DWs) in nanowires.[1–3] To realize such a device, reproducible and reliable pinning sites for individual DWs are required. Geometric constrictions are widely used to create local confining potentials that act as pinning sites for individual DWs.[4–10] As an alternative, the local modification of magnetic properties by ion irradiation is suitable to induce pinning sites.[11] In this case, a variation in the wire geometry on the nanoscale is not required. Implantation of chromium ions into permalloy ($Ni_{80}Fe_{20}$) is known to cause alloying and structural defects which lead to a reduction in the Curie temperature, the saturation magnetization M_S, and the magnetic anisotropy as well as to a change in the exchange constant and the damping parameter.[12–14] Field-driven pinning and depinning of a DW at these so-called magnetic soft spots has been directly observed by magnetic transmission soft x-ray microscopy (MTXM).[11] The strength of the pinning potential can be tuned by the chromium ion fluence applied to induce the soft spots.

Potential storage devices, e.g., the racetrack memory[2] necessitate to move a series of DWs. Neighboring head-to-head and tail-to-tail DWs in a nanowire move in opposite directions under application of uniform magnetic fields and annihilate each other. However, these DWs can be moved in the same direction via transfer of spin-angular momentum by spin-polarized currents.[15] In the absence of an external magnetic field, the DWs are displaced in the direction of the electron flow.[2,4,16,17]

Here, we study the field- and current-induced depinning of DWs from a square-shaped magnetic soft spot in permalloy nanowires. Micromagnetic simulations, high resolution MTXM, and electrical measurements of the anisotropic magnetoresistance (AMR) are employed to characterize the pinning potential. Depinning probabilities are determined for different amplitudes of single current pulses driven through the wire.

Micromagnetic simulations of the propagation of a DW driven by an external magnetic field are performed using the Object Oriented MicroMagnetic Framework (OOMMF).[18] We consider a 200 nm wide and 15 nm thick nanowire containing a transverse wall and a 400 nm wide and 30 nm thick nanowire containing a vortex wall. A saturation magnetization $M_S = 8.6 \times 10^5$ A m^{-1}, an exchange constant $A = 13 \times 10^{-12}$ J m^{-1}, and an anisotropy constant $K = 0$ are assumed. The Gilbert damping parameter is set to $\alpha = 0.5$ which leads to a smooth propagation of the DW through the wire during the calculations and, in this way, enables to evaluate the potential. The saturation magnetization in the irradiated region is set to 80% of the original value[19] whereas the other material parameters are not changed. Figures 1(a) and 1(b) show different potentials for transverse and vortex walls. The total energy $E_{tot} = E_d + E_{ex}$ associated with the transverse wall is locally reduced (potential well) and a position of the DW at the magnetic soft spot is thus energetically favorable in comparison to the environment. For a vortex wall, the total energy also decreases approaching the soft spot but the soft spot itself represents a potential barrier for the DW. The insets indicate that the vortex structure is pinned at the border of the spot. Note that, in both cases, the relative contribution of the exchange energy E_{ex} to the total energy is about 14%. A change in the exchange constant in the soft magnetic region is not considered and the decrease in E_{ex} in Fig. 1 is attributed to a change in the structure of the DW, compare insets of Figs. 1(a) and 1(b).

Nanowires with a width of 400 nm are fabricated using electron-beam lithography and lift-off processing. Polycrystalline permalloy with a thickness of 30 nm is thermally evaporated onto 100 nm thin silicon nitride membranes and silicon substrates with a 300 nm thick silicon oxide coating. A magnetic soft spot is induced by 15 kV chromium ion irradiation at a fluence of 1.5×10^{16} cm^{-2} through a poly-

[a)]Electronic mail: andreas.vogel@physnet.uni-hamburg.de.

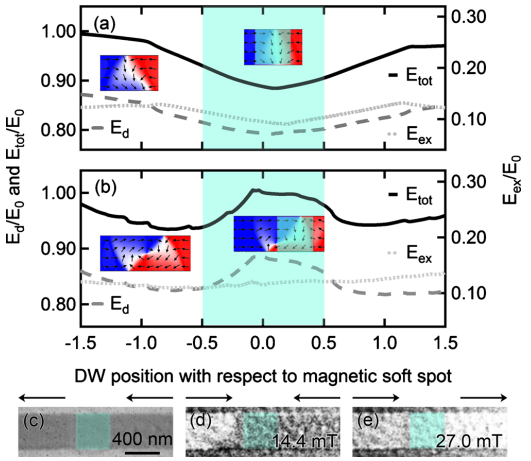

FIG. 1. (Color online) Micromagnetic simulation of the position-dependent total energy E_{tot} (solid line) for a (a) transverse and (b) vortex wall in a nanowire. The soft magnetic region is marked by the light-colored shadow. The dashed line (left axis) represents the demagnetization energy E_d and the dotted line (right axis) represents the exchange energy E_{ex}. Insets show the DW structure in the corresponding regions. The position of the DW is given in units of the size of the soft spot. Energy values are normalized to $E_0 = E_{tot}(-2)$. [(c)–(e)] Successive differential x-ray micrographs of the magnetization configuration under application of a magnetic field aligned parallel to the nanowire. Arrows indicate the magnetization direction.

methylmethacrylate (PMMA) electron-beam resist shadow mask. Before irradiation, the shadow mask is covered with 3 nm chromium to reduce sputtering effects.

MTXM enables to directly image the position of a DW. Measurements are performed at beamline 6.1.2 of the Advanced Light Source in Berkeley, CA, USA (Ref. 20) using the sample design with a rectangular nucleation pad described in Ref. 11. The sample is mounted under an angle of 60° with respect to the beam propagation direction. Magnetic contrast is provided via the x-ray magnetic circular dichroism at the Ni L_3-absorption edge (852.7 eV).[21] Figure 1(c) shows a MTXM micrograph in the saturated state. A magnetic field aligned parallel to the nanowire is successively reversed. Differential images with respect to the saturated state are shown in Figs. 1(d) and 1(e) for two characteristic magnetization configurations. White contrast in Fig. 1(d) reveals that at 14.4 mT a DW is pinned at the boundary of the magnetic soft spot as anticipated from the micromagnetic simulations for a vortex wall. Note that for the given wire geometry, the presence of a vortex wall is energetically favorable.[9,22] In Fig. 1(e), the DW is depinned at nominally 27.0 mT which is significantly higher than the typical depinning fields from intrinsic pinning sites.[11] To further characterize the pinning potential, electrical measurements with a high repetition rate are performed.

Pinning and depinning of DWs can be electrically detected by a change in the AMR.[9] For this purpose, nanowires as shown in Fig. 2 are contacted via two gold leads. By applying an external magnetic field of 120 mT under an angle of $\varphi = -100°$ with respect to the x axis, a tail-to-tail DW is prepared in the curvature of the wire. The field is switched off and then applied along the x axis to move the DW toward the soft spot. Figure 3(a) shows measurements of the resistance of the wire for a field swept in positive x

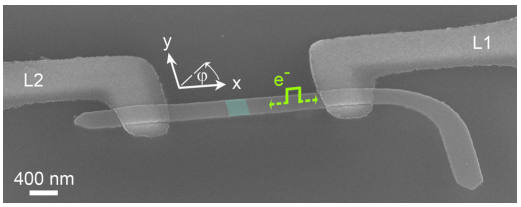

FIG. 2. (Color online) Scanning-electron micrograph of a 400 nm wide permalloy nanowire with gold contacts L1 and L2. The position of the magnetic soft spot is marked by a light-colored shadow. The current pulse and the field angle φ are indicated.

direction. At 2.4 mT, the DW enters the region between the contacts and is pinned at the soft spot, detected as a drop of the AMR signal of about 160 mΩ. The DW is depinned at 11 mT where the resistance again increases. To characterize the pinning potential, the DW is moved to the soft spot using a field of 8 mT. Subsequently, the magnetic field is swept in both directions along the x axis starting from zero field. Figures 3(b) and 3(c) reveal that the depinning field is significantly lower when the DW is pushed back toward the curvature. This indicates a potential barrier and coincides with the micromagnetic simulations for a vortex wall and the results of the MTXM measurements where the DW is pinned at one side of the soft spot, compare Fig. 1(d). Repeated measurements reveal a narrow depinning field distribution which indicates that the same DW type is reproducibly achieved. In Figs. 3(d)–3(f) measurements for a head-to-head DW are shown. In this case, the DW is prepared by applying the field under an angle of $\varphi = 82°$. The absolute depinning fields are almost equal to the fields observed for the tail-to-tail DW.

To investigate the current-driven depinning, single 10 ns voltage pulses with a rise time of 2 ns are driven through the wire between the contacts L1 and L2. The AMR is measured (i) after creation of the DW in the curvature, (ii) after moving

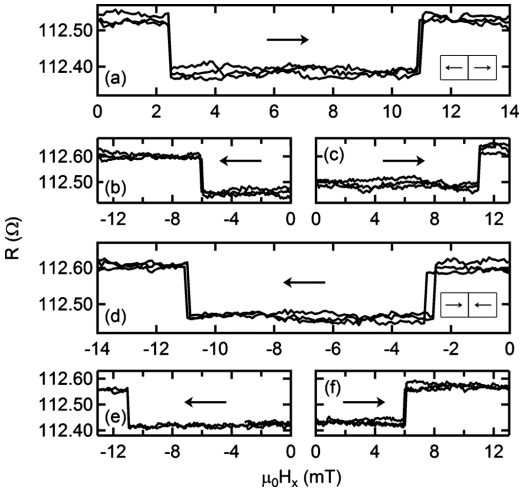

FIG. 3. Dependence of the resistance of a nanowire between the contacts L1 and L2 on a magnetic field in x direction. The arrow indicates the sweep direction of the magnetic field. [(a)–(c)] Tail-to-tail or [(d)–(f)] head-to-head DWs have been prepared in the curvature of the wire prior to the field sweep.

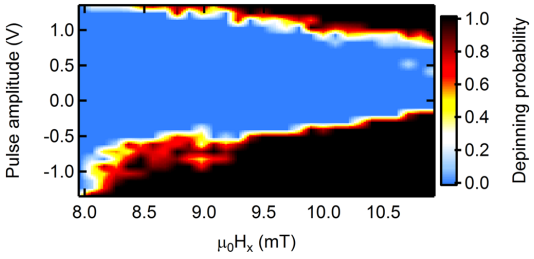

FIG. 4. (Color online) Depinning probability of a tail-to-tail DW for different amplitudes of a 10 ns current pulse and different magnetic background fields (11 070 measurements).

the DW toward the soft spot, and (iii) after application of the pulse. Figure 4 shows the depinning probability of a tail-to-tail DW for pulses of different amplitudes at magnetic background fields between 8 and 11 mT. Measurements have been repeated ten times for each set of parameters. Events where no DW was pinned at the spot before application of the pulse are not taken into account to calculate the depinning probability. A negative pulse amplitude corresponds to an electron flux in the direction of the DW motion given by the background field. Above a certain threshold value, the DW is depinned by the resulting current pulse. For smaller background fields, higher current densities are required. At a pulse amplitude of $V_0 = \pm 1.3$ V, a maximum current density of $j \approx 1 \times 10^{12}$ A m^{-2} is achieved. Here, the critical current density is higher when the direction of the electron flux opposes the direction of the DW motion. Note that doping has been reported to affect the spin polarization and the nonadiabaticity parameter in the ferromagnetic material.[23] It would be interesting to determine the influence of chromium implantation on these parameters in a future study.

In summary, we have demonstrated field-induced DW pinning and depinning as well as reliable depinning by single current pulses in a permalloy nanowire containing a square-shaped magnetic soft spot. Micromagnetic simulations show different shapes of the pinning potential for transverse and vortex walls. Experimental results reveal the presence of a potential barrier which coincides with the expectations from simulations for a vortex wall. The local modification of magnetic properties by irradiation with chromium ions is suitable to induce pinning sites. Lower requirements on the lithography in comparison to geometric constrictions on the nanoscale, a smaller distribution of properties due to parallel processing during implantation, and fine tunability of the pinning potential via the chromium ion fluence make the magnetic soft spots a promising candidate for applications.

We thank Ulrich Merkt for fruitful discussions and continuous support as well as Michael Volkmann and Ingolf Winkler for superb technical assistance. Financial support of the Deutsche Forschungsgemeinschaft via Grant Nos. FA314/3-2 and MC9/7-2, the Sonderforschungsbereich 668 and the Graduiertenkolleg 1286 as well as of the Forschungs- und Wissenschaftsstiftung Hamburg via the Exzellenzcluster "Nano-Spintronik" is gratefully acknowledged. Operation of the x-ray microscope is supported by the Director, Office of Science, Office of Basic Energy Sciences, of the U.S. Department of Energy under Contract No. DE-AC02-05-CH11231.

[1]D. A. Allwood, G. Xiong, C. C. Faulkner, D. Atkinson, D. Petit, and R. P. Cowburn, Science **309**, 1688 (2005).
[2]S. S. P. Parkin, M. Hayashi, and L. Thomas, Science **320**, 190 (2008).
[3]T. Ono, H. Miyajima, K. Shigeto, K. Mibu, N. Hosoito, and T. Shinjo, Science **284**, 468 (1999).
[4]C. K. Lim, T. Devolder, C. Chappert, J. Grollier, V. Cros, A. Vaurès, A. Fert, and G. Faini, Appl. Phys. Lett. **84**, 2820 (2004).
[5]M. Kläui, C. A. F. Vaz, J. A. C. Bland, W. Wernsdorfer, G. Faini, E. Cambril, L. J. Heydermann, F. Nolting, and U. Rüdiger, Phys. Rev. Lett. **94**, 106601 (2005).
[6]M. Hayashi, L. Thomas, C. Rettner, R. Moriya, X. Jiang, and S. S. P. Parkin, Phys. Rev. Lett. **97**, 207205 (2006).
[7]L. K. Bogart, D. Atkinson, K. O'Shea, D. McGrouther, and S. McVitie, Phys. Rev. B **79**, 054414 (2009).
[8]M.-Y. Im, L. Bocklage, P. Fischer, and G. Meier, Phys. Rev. Lett. **102**, 147204 (2009).
[9]L. Bocklage, B. Krüger, T. Matsuyama, M. Bolte, U. Merkt, D. Pfannkuche, and G. Meier, Phys. Rev. Lett. **103**, 197204 (2009).
[10]D. Djuhana, H.-G. Piao, S.-H. Lee, D.-H. Kim, S.-M. Ahn, and S.-B. Choe, Appl. Phys. Lett. **97**, 022511 (2010).
[11]A. Vogel, S. Wintz, J. Kimling, M. Bolte, T. Strache, M. Fritzsche, M.-Y. Im, P. Fischer, G. Meier, and J. Fassbender, IEEE Trans. Magn. **46**, 1708 (2010).
[12]J. Fassbender, J. von Borany, A. Mücklich, K. Potzger, W. Möller, J. McCord, L. Schultz, and R. Mattheis, Phys. Rev. B **73**, 184410 (2006).
[13]L. Folks, R. E. Fontana, B. A. Gurney, J. R. Childress, S. Maat, J. A. Katine, J. E. E. Baglin, and A. J. Kellock, J. Phys. D **36**, 2601 (2003).
[14]J. Fassbender and J. McCord, J. Magn. Magn. Mater. **320**, 579 (2008).
[15]S. Zhang and Z. Li, Phys. Rev. Lett. **93**, 127204 (2004).
[16]A. Yamaguchi, T. Ono, S. Nasu, K. Miyake, K. Mibu, and T. Shinjo, Phys. Rev. Lett. **92**, 077205 (2004).
[17]G. Meier, M. Bolte, R. Eiselt, B. Krüger, D.-H. Kim, and P. Fischer, Phys. Rev. Lett. **98**, 187202 (2007).
[18]OOMMF User's Guide http://math.nist.gov/oommf/.
[19]Broadband ferromagnetic resonance measurements on 30 nm thick permalloy films irradiated with a chromium fluence of 1.5×10^{16} cm^{-2} at 15 kV reveal a reduction in M_S of about 20%.
[20]P. Fischer, D.-H. Kim, W. Chao, J. A. Liddle, E. H. Anderson, and D. T. Attwood, Mater. Today **9**, 26 (2006).
[21]C. T. Chen, F. Sette, Y. Ma, and S. Modesti, Phys. Rev. B **42**, 7262 (1990).
[22]Y. Nakatani, A. Thiaville, and J. Miltat, J. Magn. Magn. Mater. **290–291**, 750 (2005).
[23]S. Lepadatu, J. S. Claydon, C. J. Kinane, T. R. Charlton, S. Langridge, A. Potenza, S. S. Dhesi, P. S. Keatley, R. J. Hicken, B. J. Hickey, and C. H. Marrows, Phys. Rev. B **81**, 020413(R) (2010).

Bibliography

[1] D. A. Allwood, G. Xiong, C. C. Faulkner, D. Atkinson, D. Petit, and R. P. Cowburn, "Magnetic domain-wall logic", *Science* **309**, 1688 (2005). 1, 25

[2] S. S. P. Parkin, M. Hayashi, and L. Thomas, "Magnetic domain-wall racetrack memory", *Science* **320**, 190 (2008). 1, 25

[3] K. Shigeto, T. Shinjo, and T. Ono, "Injection of a magnetic domain wall into a submicron magnetic wire", *Appl. Phys. Lett.* **75**, 2815 (1999). 1

[4] R. P. Cowburn, D. A. Allwood, G. Xiong, and M. D. Cooke, "Domain wall injection and propagation in planar Permalloy nanowires", *J. Appl. Phys.* **91**, 6949 (2002). 1, 54

[5] D. Atkinson, D. A. Allwood, G. Xiong, M. D. Cooke, C. C. Faulkner, and R. P. Cowburn, "Magnetic domain-wall dynamics in a submicrometre ferromagnetic structure.", *Nat. Mater.* **2**, 85 (2003). 1

[6] D. McGrouther, S. McVitie, J. N. Chapman, and A. Gentils, "Controlled domain wall injection into ferromagnetic nanowires from an optimized pad geometry", *Appl. Phys. Lett.* **91**, 022506 (2007). 1

[7] A. Yamaguchi, T. Ono, S. Nasu, K. Miyake, K. Mibu, and T. Shinjo, "Real-Space Observation of Current-Driven Domain Wall Motion in Submicron Magnetic Wires", *Phys. Rev. Lett.* **92**, 077205 (2004). 1

[8] M. Hayashi, L. Thomas, C. Rettner, R. Moriya, X. Jiang, and S. S. P. Parkin, "Dependence of current and field driven depinning of domain walls on their structure and chirality in permalloy nanowires", *Phys. Rev. Lett.* **97**, 207205 (2006). 1, 2

[9] G. Meier, M. Bolte, R. Eiselt, B. Krüger, D.-H. Kim, and P. Fischer, "Direct Imaging of Stochastic Domain-Wall Motion Driven by Nanosecond Current Pulses", *Phys. Rev. Lett.* **98**, 187202 (2007). 1

[10] F.-U. Stein, L. Bocklage, M. Weigand, and G. Meier, "Time-resolved imaging of nonlinear magnetic domain-wall dynamics in ferromagnetic nanowires", *Sci. Rep.* **3**, 7 (2013). 1

[11] F.-U. Stein, L. Bocklage, M. Weigand, and G. Meier, “Direct observation of internal vortex domain-wall dynamics”, *Phys. Rev. B* **89**, 024423 (2014). 1

[12] J. D. Livingston, “A review of coercivity mechanisms (invited)”, *J. Appl. Phys.* **52**, 2544 (1981). 1

[13] H. Kronmüller, “Theory of Nucleation Fields in Inhomogeneous Ferromagnets”, *Phys. Status Solidi B* **144**, 385 (1987). 1, 33, 63

[14] R. Skomski, “Nucleation in Inhomogeneous Permanent Magnets”, *Phys. Status Solidi B* **174**, K77 (1992). 1

[15] R. Skomski, “Micromagnetic localization”, *J. Appl. Phys.* **83**, 6503 (1998). 1, 42, 56

[16] J. M. Shaw, M. Olsen, J. W. Lau, M. L. Schneider, T. J. Silva, O. Hellwig, E. Dobisz, and B. D. Terris, “Intrinsic defects in perpendicularly magnetized multilayer thin films and nanostructures”, *Phys. Rev. B* **82**, 144437 (2010). 1, 32

[17] T. Gerhardt, A. Drews, and G. Meier, “Controlled pinning and depinning of domain walls in nanowires with perpendicular magnetic anisotropy.”, *J. Phys. Condens. Matter* **24**, 024208 (2012). 1, 2, 33, 40, 47, 54, 57, 66

[18] J. Kimling, T. Gerhardt, A. Kobs, A. Vogel, S. Wintz, M.-Y. Im, P. Fischer, H. P. Oepen, U. Merkt, and G. Meier, “Tuning of the nucleation field in nanowires with perpendicular magnetic anisotropy”, *J. Appl. Phys.* **113**, 163902 (2013). 1, 33, 54

[19] J. H. Franken, Y. Yin, a. J. Schellekens, A. van den Brink, H. J. M. Swagten, and B. Koopmans, “Voltage-gated pinning in a magnetic domain-wall conduit”, *Appl. Phys. Lett.* **103**, 102411 (2013). 1, 2, 29

[20] J. Grollier, P. Boulenc, V. Cros, A. Hamzić, A. Vaurès, A. Fert, and G. Faini, “Switching a spin valve back and forth by current-induced domain wall motion”, *Appl. Phys. Lett.* **83**, 509 (2003). 1

[21] C. Burrowes, D. Ravelosona, C. Chappert, S. Mangin, E. E. Fullerton, J. A. Katine, and B. D. Terris, “Role of pinning in current driven domain wall motion in wires with perpendicular anisotropy”, *Appl. Phys. Lett.* **93**, 172513 (2008). 1

[22] M. Kläui, H. Ehrke, U. Rüdiger, T. Kasama, R. E. Dunin-Borkowski, D. Backes, L. J. Heyderman, C. A. F. Vaz, J. A. C. Bland, G. Faini, E. Cambril, and W. Wernsdorfer, “Direct observation of domain-wall pinning at nanoscale constrictions”, *Appl. Phys. Lett.* **87**, 102509 (2005). 2

[23] L. Bocklage, B. Krüger, T. Matsuyama, M. Bolte, U. Merkt, D. Pfannkuche, and G. Meier, "Dependence of magnetic domain-wall motion on a fast changing current", *Phys. Rev. Lett.* **103**, 197204 (2009). 2

[24] L. Bogart, D. Atkinson, K. O'Shea, D. McGrouther, and S. McVitie, "Dependence of domain wall pinning potential landscapes on domain wall chirality and pinning site geometry in planar nanowires", *Phys. Rev. B* **79**, 054414 (2009). 2

[25] M.-Y. Im, L. Bocklage, P. Fischer, and G. Meier, "Direct observation of stochastic domain-wall depinning in magnetic nanowires", *Phys. Rev. Lett.* **102**, 147204 (2009). 2

[26] D. Djuhana, H.-G. Piao, S.-H. Lee, D.-H. Kim, S.-M. Ahn, and S.-B. Choe, "Asymmetric ground state spin configuration of transverse domain wall on symmetrically notched ferromagnetic nanowires", *Appl. Phys. Lett.* **97**, 022511 (2010). 2

[27] T. Koyama, G. Yamada, H. Tanigawa, S. Kasai, N. Ohshima, S. Fukami, N. Ishiwata, Y. Nakatani, and T. Ono, "Control of Domain Wall Position by Electrical Current in Structured Co/Ni Wire with Perpendicular Magnetic Anisotropy", *Appl. Phys. Express* **1**, 101303 (2008). 2

[28] S.-B. Choe, "Depinning field from notches on Co/Pd multilayer nanowires with perpendicular magnetic anisotropy", *Phys. Status Solidi C* **4**, 4433 (2007). 2

[29] T. Suzuki, S. Fukami, N. Ohshima, K. Nagahara, and N. Ishiwata, "Analysis of current-driven domain wall motion from pinning sites in nanostrips with perpendicular magnetic anisotropy", *J. Appl. Phys.* **103**, 113913 (2008). 2

[30] K.-J. Kim and S.-B. Choe, "Analytic theory of wall configuration and depinning mechanism in magnetic nanostructure with perpendicular magnetic anisotropy", *J. Magn. Magn. Mater.* **321**, 2197 (2009). 2

[31] A. Vogel, S. Wintz, J. Kimling, M. Bolte, T. Strache, M. Fritzsche, M.-Y. Im, P. Fischer, G. Meier, and J. Fassbender, "Domain-Wall Pinning and Depinning at Soft Spots in Magnetic Nanowires", *IEEE Trans. Magn.* **46**, 1708 (2010). 2

[32] J. H. Franken, M. Hoeijmakers, R. Lavrijsen, and H. J. M. Swagten, "Domain-wall pinning by local control of anisotropy in Pt/Co/Pt strips", *J. Phys. Condens. Matter* **24**, 024216 (2011). 2, 47

[33] A. Vogel, S. Wintz, T. Gerhardt, L. Bocklage, T. Strache, M.-Y. Im, P. Fischer, J. Fassbender, J. McCord, and G. Meier, "Field- and current-induced domain-wall motion in permalloy nanowires with magnetic soft spots", *Appl. Phys. Lett.* **98**, 202501 (2011). 2

[34] J. H. Franken, H. J. M. Swagten, and B. Koopmans, “Shift registers based on magnetic domain wall ratchets with perpendicular anisotropy”, *Nat. Nanotechnol.* **7**, 499 (2012). 2

[35] T. Gerhardt, A. Drews, and G. Meier, “Current-driven domain wall depinning from an anisotropy boundary in nanowires”, *J. Phys. Condens. Matter* **26**, 206001 (2014). 2, 47, 66

[36] J. Fassbender, J. von Borany, A. Mücklich, K. Potzger, W. Möller, J. McCord, L. Schultz, and R. Mattheis, “Structural and magnetic modifications of Cr-implanted Permalloy”, *Phys. Rev. B* **73**, 184410 (2006). 2, 29

[37] J. Fassbender, T. Strache, M. O. Liedke, D. Markó, S. Wintz, K. Lenz, A. Keller, S. Facsko, I. Mönch, and J. McCord, “Introducing artificial length scales to tailor magnetic properties”, *New J. Phys.* **11**, 125002 (2009). 2

[38] C. Chappert, H. Bernas, J. Ferré, V. Kottler, J.-P. Jamet, Y. Chen, E. Cambril, T. Devolder, F. Rousseaux, V. Mathet, and H. Launois, “Planar Patterned Magnetic Media Obtained by Ion Irradiation”, *Science* **280**, 1919 (1998). 2, 28

[39] D. Stanescu, D. Ravelosona, V. Mathet, C. Chappert, Y. Samson, C. Beigné, N. Vernier, J. Ferré, J. Gierak, E. Bouhris, and E. E. Fullerton, “Tailoring magnetism in CoNi films with perpendicular anisotropy by ion irradiation”, *J. Appl. Phys.* **103**, 07B529 (2008). 2, 28

[40] J.-M. L. Beaujour, A. D. Kent, D. Ravelosona, I. Tudosa, and E. E. Fullerton, “Ferromagnetic resonance study of Co/Pd/Co/Ni multilayers with perpendicular anisotropy irradiated with helium ions”, *J. Appl. Phys.* **109**, 033917 (2011). 2

[41] D. Chiba, S. Fukami, K. Shimamura, N. Ishiwata, K. Kobayashi, and T. Ono, “Electrical control of the ferromagnetic phase transition in cobalt at room temperature.”, *Nat. Mater.* **10**, 853 (2011). 2

[42] “MicroMagnum”, URL: http://micromagnum.informatik.uni-hamburg.de/. 2, 30, 57, 62

[43] A. Hubert and R. Schäfer, “Magnetic Domains: The Analysis of Magnetic Microstructures”, *Berlin/Heidelberg: Springer-Verlag* (1998). 3, 38

[44] M. J. Donahue and D. G. Porter, “OOMMF User’s Guide”, *Gaithersburg: US Department of Commerce, Technology Administration, National Institute of Standards and Technology* (1999). 3, 57

[45] L. Landau and E. Lifshits, “On the Theory of Dispersion of Magnetic Permeability in Ferromagnetic Bodies”, *Phys. Z. Sowjetunion* **8**, 153 (1935). 5, 7

[46] T. L. Gilbert, “A Lagrangian formulation of the gyromagnetic equation of the magnetic field”, *Phys. Rev.* **100**, 1243 (1955). 5

[47] T. L. Gilbert, “A phenomenological theory of damping in ferromagnetic materials”, *IEEE Trans. Magn.* **40**, 3443 (2004). 5, 7

[48] L. Berger, “Low-field magnetoresistance and domain drag in ferromagnets”, *J. Appl. Phys.* **49**, 2156 (1978). 9, 10

[49] L. Berger, “Exchange interaction between ferromagnetic domain wall and electric current in very thin metallic films”, *J. Appl. Phys.* **55**, 1954 (1984). 10

[50] L. Berger, “Emission of spin waves by a magnetic multilayer traversed by a current”, *Phys. Rev. B* **54**, 9353 (1996). 10

[51] J. C. Slonczewski, “Current-driven excitation of magnetic multilayers”, *J. Magn. Magn. Mater.* **159**, L1 (1996). 10

[52] Y. B. Bazaliy, B. A. Jones, and S.-C. Zhang, “Modification of the Landau-Lifshitz equation in the presence of a spin-polarized current in colossal- and giant-magnetoresistive materials”, *Phys. Rev. B* **57**, R3213 (1998). 10, 12

[53] S. Zhang and Z. Li, “Roles of nonequilibrium conduction electrons on the magnetization dynamics of ferromagnets”, *Phys. Rev. Lett.* **93**, 127204 (2004). 10, 11, 46

[54] C. Burrowes, A. P. Mihai, D. Ravelosona, J.-V. Kim, C. Chappert, L. Vila, A. Marty, Y. Samson, F. Garcia-Sanchez, L. D. Buda-Prejbeanu, I. Tudosa, E. E. Fullerton, and J.-P. Attané, “Non-adiabatic spin-torques in narrow magnetic domain walls”, *Nat. Phys.* **6**, 17 (2009). 12

[55] H. Stillrich, C. Menk, R. Frömter, and H. P. Oepen, “Magnetic anisotropy and the cone state in Co/Pt multilayer films”, *J. Appl. Phys.* **105**, 07C308 (2009). 14, 59, 61

[56] C. Chappert and P. Bruno, “Magnetic anisotropy in metallic ultrathin films and related experiments on cobalt films (invited)”, *J. Appl. Phys.* **64**, 5736 (1988). 14

[57] F. J. A. den Broeder, W. Hoving, and P. J. H. Bloemen, “Magnetic anisotropy of multilayers”, *J. Magn. Magn. Mater.* **93**, 562 (1991). 14

[58] J. D. Jackson, “Classical electrodynamics”, *New York: Wiley* (1999). 15

[59] W. Heisenberg, “Mehrkörperproblem und Resonanz in der Quantenmechanik”, *Zeitschrift für Phys.* **38**, 411 (1926). 18

[60] P. A. M. Dirac, “On the Theory of Quantum Mechanics”, *Proc. R. Soc. A Math. Phys. Eng. Sci.* **112**, 661 (1926). 18

[61] W. Heisenberg, “Zur Theorie des Ferromagnetismus”, *Zeitschrift für Phys.* **49**, 619 (1928). 18

[62] W. F. Brown, Jr., “Thermal Fluctuations of a Single-Domain Particle”, *Phys. Rev.* **130**, 1677 (1963). 21

[63] W. F. Brown, Jr., “Thermal fluctuation of fine ferromagnetic particles”, *IEEE Trans. Magn.* **15**, 1196 (1979). 21

[64] D. A. Garanin, “Fokker-Planck and Landau-Lifshitz-Bloch equations for classical ferromagnets”, *Phys. Rev. B* **55**, 3050 (1997). 21

[65] E. Feldtkeller, “Mikromagnetisch stetige und unstetige Magnetisierungskonfigurationen”, *Zeitschrift für Angew. Phys.* **19**, 530 (1965). 21

[66] H. Niedoba and M. Labrune, “Magnetization reversal via bloch points nucleation in nanowires and dots: a micromagnetic study”, *Eur. Phys. J. B* **47**, 467 (2005). 21

[67] I. E. Dzialoshinskii, “Thermodynamic theory of weak ferromagnetism in antiferromagnetic substances”, *Sov. Physics, J. Exp. Theor. Phys.* **5**, 1259 (1957). 22

[68] T. Moriya, “Anisotropic Superexchange Interaction and Weak Ferromagnetism”, *Phys. Rev.* **120**, 91 (1960). 22

[69] M. Bode, M. Heide, K. von Bergmann, P. Ferriani, S. Heinze, G. Bihlmayer, A. Kubetzka, O. Pietzsch, S. Blügel, and R. Wiesendanger, “Chiral magnetic order at surfaces driven by inversion asymmetry.”, *Nature* **447**, 190 (2007). 22

[70] J. Hirsch, “Spin Hall Effect”, *Phys. Rev. Lett.* **83**, 1834 (1999). 22

[71] P. P. J. Haazen, E. Murè, J. H. Franken, R. Lavrijsen, H. J. M. Swagten, and B. Koopmans, “Domain wall depinning governed by the spin Hall effect”, *Nat. Mater.* **12**, 299 (2013). 22, 23

[72] L. Néel, “Sur un nouveau mode de couplage entre les aimantations de deux minces ferromagnetiques”, *Comptes Rendus l’Académie des Sci.* **255**, 1676 (1962). 22

[73] B. D. Schrag, A. Anguelouch, S. Ingvarsson, G. Xiao, Y. Lu, P. L. Trouilloud, A. Gupta, R. A. Wanner, W. J. Gallagher, P. M. Rice, and S. S. P. Parkin, “Néel "orange-peel" coupling in magnetic tunneling junction devices”, *Appl. Phys. Lett.* **77**, 2373 (2000). 22

[74] M. A. Ruderman and C. Kittel, “Indirect exchange coupling of nuclear magnetic moments by conduction electrons”, *Phys. Rev.* **96**, 99 (1954). 22

[75] T. Kasuya, “A Theory of Metallic Ferro- and Antiferromagnetism on Zener’s Model”, *Prog. Theor. Phys.* **16**, 45 (1956).

[76] K. Yosida, “Magnetic Properties of Cu-Mn Alloys”, *Phys. Rev.* **106**, 893 (1957). 22

[77] L. Nordström, P. Lang, R. Zeller, and P. Dederichs, “Influence of the magnetic-layer thickness on the interlayer exchange coupling: Competition between oscillation periods”, *Phys. Rev. B* **50**, 13058 (1994). 22

[78] U. Gradmann, “Magnetism of surfaces and interfaces”, *J. Magn. Magn. Mater.* **6**, 173 (1977). 22

[79] P. F. Carcia, A. D. Meinhaldt, and A. Suna, “Perpendicular magnetic anisotropy in Pd/Co thin film layered structures”, *Appl. Phys. Lett.* **47**, 178 (1985). 22

[80] Y. Kajiwara, K. Harii, S. Takahashi, J. Ohe, K. Uchida, M. Mizuguchi, H. Umezawa, H. Kawai, K. Ando, K. Takanashi, S. Maekawa, and E. Saitoh, “Transmission of electrical signals by spin-wave interconversion in a magnetic insulator.”, *Nature* **464**, 262 (2010). 23

[81] O. A. Tretiakov and A. Abanov, “Current Driven Magnetization Dynamics in Ferromagnetic Nanowires with a Dzyaloshinskii-Moriya Interaction”, *Phys. Rev. Lett.* **105**, 157201 (2010). 23

[82] A. Thiaville, S. Rohart, E. Jué, V. Cros, and A. Fert, “Dynamics of Dzyaloshinskii domain walls in ultrathin magnetic films”, *Europhys. Lett.* **100**, 57002 (2012). 23

[83] A. Thiaville, J. García, R. Dittrich, J. Miltat, and T. Schrefl, “Micromagnetic study of Bloch-point-mediated vortex core reversal”, *Phys. Rev. B* **67**, 094410 (2003). 23

[84] S. Fukami, T. Suzuki, N. Ohshima, K. Nagahara, and N. Ishiwata, “Micromagnetic analysis of current driven domain wall motion in nanostrips with perpendicular magnetic anisotropy”, *J. Appl. Phys.* **103**, 07E718 (2008). 25

[85] L. Thomas, S.-H. Yang, K.-S. Ryu, B. Hughes, C. Rettner, D.-S. Wang, C.-H. Tsai, K.-H. Shen, and S. S. P. Parkin, “Racetrack Memory: A high-performance, low-cost, non-volatile memory based on magnetic domain walls”, in *2011 IEEE Int. Electron Devices Meet.* 24.2.1 (2011). 25

[86] W. B. Zeper, F. J. A. M. Greidanus, P. F. Carcia, and C. R. Fincher, “Perpendicular magnetic anisotropy and magneto-optical Kerr effect of vapor-deposited Co/Pt-layered structures”, *J. Appl. Phys.* **65**, 4971 (1989). 27, 61

[87] S. Hashimoto, Y. Ochiai, and K. Aso, “Perpendicular magnetic anisotropy and magnetostriction of sputtered Co/Pd and Co/Pt multilayered films”, *J. Appl. Phys.* **66**, 4909 (1989). 27

[88] N. Nakajima, T. Koide, T. Shidara, H. Miyauchi, H. Fukutani, A. Fujimori, K. Iio, T. Katayama, M. Nývlt, and Y. Suzuki, “Perpendicular Magnetic Anisotropy Caused by Interfacial Hybridization via Enhanced Orbital Moment in Co/Pt Multilayers: Magnetic Circular X-Ray Dichroism Study”, *Phys. Rev. Lett.* **81**, 5229 (1998). 27

[89] G. H. O. Daalderop, P. J. Kelly, and F. J. A. den Broeder, “Prediction and confirmation of perpendicular magnetic anisotropy in Co/Ni multilayers”, *Phys. Rev. Lett.* **68**, 682 (1992). 27

[90] S. Mangin, D. Ravelosona, J. A. Katine, M. J. Carey, B. D. Terris, and E. E. Fullerton, “Current-induced magnetization reversal in nanopillars with perpendicular anisotropy”, *Nat. Mater.* **5**, 210 (2006). 27

[91] D. G. Stinson and S.-C. Shin, “Magnetization and anisotropy of Co/Pd multilayer thin films”, *J. Appl. Phys.* **67**, 4459 (1990). 27

[92] D. Jeanniot and J. Desserre, “A transition-metal–rare-earth alloy for perpendicular magnetic recording”, *J. Appl. Phys.* **54**, 2820 (1983). 28

[93] K. Matsumoto, K. Ozaki, A. Chekanov, I. Tagawa, and K. Shono, “Magnetic Recording on Magneto-Optical Media Using Merge Type Giant Magneto-Resistive Head”, *Jpn. J. Appl. Phys.* **39**, L1161 (2000). 28

[94] M. Miyazaki, I. Shibata, S. Okada, K. Ito, and S. Ogawa, “A new protective film for magneto-optical TbFeCo media”, *J. Appl. Phys.* **61**, 3326 (1987). 28

[95] D. Miller, E. Marinero, and H. Notarys, “XPS oxidation study of TbFeCo films”, *Appl. Surf. Sci.* **35**, 153 (1988). 28

[96] S. N. Gadetsky, A. V. Stupnov, M. V. Zumkin, and E. N. Nikolaev, “Domain wall dynamics in TbFeCo thin films”, *IEEE Trans. Magn.* **28**, 2928 (1992). 28

[97] S. Li, H. Nakamura, T. Kanazawa, X. Liu, and A. Morisako, “Current-Induced Domain Wall Motion in TbFeCo Wires With Perpendicular Magnetic Anisotropy”, *IEEE Trans. Magn.* **46**, 1695 (2010). 28

[98] D.-T. Ngo, K. Ikeda, and H. Awano, “Direct Observation of Domain Wall Motion Induced by Low-Current Density in TbFeCo Wires”, *Appl. Phys. Express* **4**, 093002 (2011). 28

[99] J. Fassbender, D. Ravelosona, and Y. Samson, “Tailoring magnetism by light-ion irradiation”, *J. Phys. D. Appl. Phys.* **37**, R179 (2004). 28

[100] M. Fiebig, “Revival of the magnetoelectric effect”, *J. Phys. D. Appl. Phys.* **38**, R123 (2005). 29

[101] W. Eerenstein, N. D. Mathur, and J. F. Scott, “Multiferroic and magnetoelectric materials.”, *Nature* **442**, 759 (2006). 29

[102] M. Weisheit, S. Fähler, A. Marty, Y. Souche, C. Poinsignon, and D. Givord, “Electric field-induced modification of magnetism in thin-film ferromagnets”, *Science* **315**, 349 (2007). 29

[103] J. Dean, M. T. Bryan, T. Schrefl, and D. a. Allwood, “Stress-based control of magnetic nanowire domain walls in artificial multiferroic systems”, *J. Appl. Phys.* **109**, 023915 (2011). 29

[104] U. Bauer, M. Przybylski, J. Kirschner, and G. S. D. Beach, “Magnetoelectric charge trap memory.”, *Nano Lett.* **12**, 1437 (2012). 29

[105] U. Bauer, S. Emori, and G. S. D. Beach, “Voltage-controlled domain wall traps in ferromagnetic nanowires.”, *Nat. Nanotechnol.* **8**, 411 (2013). 29

[106] M. K. Niranjan, C.-G. Duan, S. S. Jaswal, and E. Y. Tsymbal, “Electric field effect on magnetization at the Fe/MgO(001) interface”, *Appl. Phys. Lett.* **96**, 222504 (2010). 29

[107] “µMag Standard Problems”, URL: http://www.ctcms.nist.gov/~rdm/mumag.org.html. 30

[108] G. S. Abo, Y.-K. Hong, J. Park, J. Lee, W. Lee, and B.-C. Choi, “Definition of Magnetic Exchange Length”, *IEEE Trans. Magn.* **49**, 4937 (2013). 31

[109] O. Chubykalo-Fesenko, U. Nowak, R. Chantrell, and D. Garanin, “Dynamic approach for micromagnetics close to the Curie temperature”, *Phys. Rev. B* **74**, 094436 (2006). 32

[110] U. Atxitia, P. Nieves, and O. Chubykalo-Fesenko, “Landau-Lifshitz-Bloch equation for ferrimagnetic materials”, *Phys. Rev. B* **86**, 104414 (2012). 32

[111] M. Becherer, G. Csaba, W. Porod, R. Emling, P. Lugli, and D. Schmitt-Landsiedel, “Magnetic Ordering of Focused-Ion-Beam Structured Cobalt-Platinum Dots for Field-Coupled Computing”, *IEEE Trans. Nanotechnol.* **7**, 316 (2008). 32

[112] S. Fukami, Y. Nakatani, T. Suzuki, K. Nagahara, N. Ohshima, and N. Ishiwata, “Relation between critical current of domain wall motion and wire dimension

in perpendicularly magnetized Co/Ni nanowires", *Appl. Phys. Lett.* **95**, 232504 (2009). 32

[113] W. F. Brown, Jr., "Virtues and Weaknesses of the Domain Concept", *Rev. Mod. Phys.* **17**, 15 (1945). 33

[114] W. F. Brown, Jr., "Criterion for Uniform Micromagnetization", *Phys. Rev.* **105**, 1479 (1957). 33

[115] A. Aharoni, "Theoretical Search for Domain Nucleation", *Rev. Mod. Phys.* **34**, 227 (1962). 33

[116] A. Aharoni, "Introduction to the Theory of Ferromagnetism", *Oxford: Clarendon Press* (1996). 33, 41

[117] A. Aharoni, "Micromagnetics: past, present and future", *Phys. B Condens. Matter* **306**, 1 (2001). 33

[118] Y. Nakatani, A. Thiaville, and J. Miltat, "Faster magnetic walls in rough wires", *Nat. Mater.* **2**, 521 (2003). 33

[119] E. C. Stoner and E. P. Wohlfarth, "A Mechanism of Magnetic Hysteresis in Heterogeneous Alloys", *Philos. Trans. R. Soc. A Math. Phys. Eng. Sci.* **240**, 599 (1948). 40

[120] H. Kronmüller, K.-D. Durst, and G. Martinek, "Angular dependence of the coercive field in sintered Fe77Nd15B8 magnets", *J. Magn. Magn. Mater.* **69**, 149 (1987). 40

[121] R. Skomski, "Simple Models of Magnetism", *Oxford University Press* (2008). 41, 57

[122] I. N. Bronstein, K. A. Semendjajew, G. Musiol, and H. Mühlig, "Taschenbuch der Mathematik", *Europa-Lehrmittel* (2013). 42

[123] W. Nolting, "Grundkurs Theoretische Physik 5.2", *Wiesbaden: Vieweg+Teubner Verlag* (1997). 42

[124] G. Tatara and H. Kohno, "Theory of current-driven domain wall motion: spin transfer versus momentum transfer", *Phys. Rev. Lett.* **92**, 086601 (2004). 43, 46

[125] A. Thiaville, Y. Nakatani, J. Miltat, and Y. Suzuki, "Micromagnetic understanding of current-driven domain wall motion in patterned nanowires", *Europhys. Lett.* **69**, 990 (2005). 43

[126] O. Tretiakov, D. Clarke, G.-W. Chern, Y. B. Bazaliy, and O. Tchernyshyov, "Dynamics of Domain Walls in Magnetic Nanostrips", *Phys. Rev. Lett.* **100**, 127204 (2008). 43, 44

[127] D. Clarke, O. Tretiakov, G.-W. Chern, Y. B. Bazaliy, and O. Tchernyshyov, “Dynamics of a vortex domain wall in a magnetic nanostrip: Application of the collective-coordinate approach”, *Phys. Rev. B* **78**, 134412 (2008). 43

[128] B. Krüger, “Current-Driven Magnetization Dynamics: Analytical Modeling and Numerical Simulation”, *PhD thesis, Hamburg* (2011). 43

[129] S.-W. Jung, W. Kim, T.-D. Lee, K.-J. Lee, and H.-W. Lee, “Current-induced domain wall motion in a nanowire with perpendicular magnetic anisotropy”, *Appl. Phys. Lett.* **92**, 202508 (2008). 49

[130] A. J. Newell, W. Williams, and D. J. Dunlop, “A generalization of the demagnetizing tensor for nonuniform magnetization”, *J. Geophys. Res.* **98**, 9551 (1993). 50

[131] “Tcl Developer Xchange”, URL: http://www.tcl.tk/. 58

[132] “Python”, URL: https://www.python.org/. 58

[133] G. Selke, “Design and Development of a GPU-accelerated Micromagnetic Simulator”, *PhD thesis, Hamburg* (2013). 58

[134] Z. S. Shan, J. X. Shen, R. D. Kirby, D. J. Sellmyer, and Y. J. Wang, “Temperature-dependent interface magnetism and magnetization reversal in Co/Pt multilayers”, *J. Appl. Phys.* **75**, 6418 (1994). 60

[135] G. Schütz, R. Wienke, W. Wilhelm, W. B. Zeper, H. Ebert, and K. Spörl, “Spin-dependent x-ray absorption in Co/Pt multilayers and Co50Pt50 alloy”, *J. Appl. Phys.* **67**, 4456 (1990). 60

[136] H. Stillrich, C. Menk, R. Frömter, and H. P. Oepen, “Magnetic anisotropy and spin reorientation in Co/Pt multilayers: Influence of preparation”, *J. Magn. Magn. Mater.* **322**, 1353 (2010). 61

[137] M. Kisielewski, A. Maziewski, M. Tekielak, J. Ferré, S. Lemerle, V. Mathet, and C. Chappert, “Magnetic anisotropy and magnetization reversal processes in Pt/Co/Pt films”, *J. Magn. Magn. Mater.* **260**, 231 (2003). 61

[138] C.-J. Lin, G. L. Gorman, C. H. Lee, R. F. C. Farrow, E. E. Marinero, H. V. Do, H. Notarys, and C. J. Chien, “Magnetic and structural properties of Co/Pt multilayers”, *J. Magn. Magn. Mater.* **93**, 194 (1991). 61

[139] R. L. Stamps, L. Louail, M. Hehn, M. Gester, and K. Ounadjela, “Anisotropies, cone states, and stripe domains in Co/Pt multilayers”, *J. Appl. Phys.* **81**, 4751 (1997). 61

[140] T. Koyama, D. Chiba, K. Ueda, K. Kondou, H. Tanigawa, S. Fukami, T. Suzuki, N. Ohshima, N. Ishiwata, Y. Nakatani, K. Kobayashi, and T. Ono, “Observation of the intrinsic pinning of a magnetic domain wall in a ferromagnetic nanowire.”, *Nat. Mater.* **10**, 194 (2011). 66, 77

[141] N. L. Schryer and L. R. Walker, “The motion of 180° domain walls in uniform dc magnetic fields”, *J. Appl. Phys.* **45**, 5406 (1974). 66

[142] H. Kronmüller and D. Goll, “Micromagnetic theory of the pinning of domain walls at phase boundaries”, *Physica B* **319**, 122 (2002). 68

[143] J. H. Franken, R. Lavrijsen, J. T. Kohlhepp, H. J. M. Swagten, and B. Koopmans, “Tunable magnetic domain wall oscillator at an anisotropy boundary”, *Appl. Phys. Lett.* **98**, 102512 (2011). 75

Publications

Published

A. Vogel, S. Wintz, T. Gerhardt, L. Bocklage, T. Strache, M.-Y. Im, P. Fischer, J. Fassbender, J. McCord, and G. Meier, “Field- and current-induced domain-wall motion in permalloy nanowires with magnetic soft spots”, *Appl. Phys. Lett.* **98**, 202501 (2011).

T. Gerhardt, A. Drews, and G. Meier, “Controlled pinning and depinning of domain walls in nanowires with perpendicular magnetic anisotropy.”, *J. Phys. Condens. Matter* **24**, 024208 (2012).

J. Kimling, T. Gerhardt, A. Kobs, A. Vogel, S. Wintz, M.-Y. Im, P. Fischer, H. P. Oepen, U. Merkt, and G. Meier, “Tuning of the nucleation field in nanowires with perpendicular magnetic anisotropy”, *J. Appl. Phys.* **113**, 163902 (2013).

T. Gerhardt, A. Drews, and G. Meier, “Current-driven domain wall depinning from an anisotropy boundary in nanowires”, *J. Phys. Condens. Matter* **26**, 206001 (2014).

Acknowledgment

At the end I'd like to thank all the people that contributed to this thesis and that supported me while I was working on it. In particular, I want to thank

Professor Dr. Dietmar P. F. Möller for the supervision of this thesis, regular fruitful discussions, and several delicious breakfasts with salmon.

Privatdozent Dr. Guido Meier for many inspiring and constructive meetings, continuous support with any kind of manuscript, and the fruitful collaboration.

Professor Dr. Ulrich Merkt for the possibility to do a PhD within the Graduiertenkolleg 1286, the patience with the monthly highlights, and the teaching of good scientific practice.

Christoph Hübner for almost exactly ten years full of both inspiring and way-out discussions, hours of hard work to solve physical problems, countless excellent lunch and coffee breaks, lots of pleasant distractions during work and in the evening, proof reading the thesis, and being a good friend.

Dr. Claas Abert for his everlasting willingness to discuss physical problems, lots of enjoyable lunch breaks and pleasant evening events, proof reading the whole thesis, and just being a great officemate.

Dr. André Drews for many inspiring discussions about micromagnetism and other things concerning life, leading our simulation sub group, and being an enjoyable officemate.

Dr. Gunnar Selke for sharing his endless knowledge about programming and solving every little problem concerning MicroMagnum with me.

Dr. Andreas Vogel for the fruitful collaboration and the pleasant and enjoyable journey to the MML conference in Japan.

Dr. Judith Kimling and Dr. André Kobs for the great collaboration.

Professor Dr. Teruo Ono and his group members for being such great hosts during my scientific visit in Kyoto, many interesting discussions about physics, and introducing me to the Japanese delicate food.

All members of Group N for inviting me to their regular summer and winter activities. It has been always a pleasure.

All members of the Graduiertenkolleg 1286 for the annual workshops that were always informative and amusing.

Dr. Katrin Buth for her commitment in the Graduiertenkolleg and correcting the monthly highlights.

The Deutsche Forschungsgemeinschaft for financial support via the Graduiertenkolleg 1286.

The "Theorists", namely Benjamin, Michael, Lars, and Max, for many pleasant lunch breaks, coffee breaks, and interesting discussions about physics, gadgets, and the physics of gadgets.

Dr. Markus Bolte for encouraging me to deal with micromagnetism and supervising me during my diploma thesis.

My parents for their willingness to always satisfy my curiosity during childhood and the everlasting support during my study without even asking. Danke Mutti, danke Vaddern.

My brother Viktor for giving me the certainty that there will always be a person in my life I can absolutely rely on.

My brother Julius for awaking my interest in any kind of computer and technical stuff. I am sure you are proud of me.

My friends, especially Malte, Salz, Herb, Aggi, Claudia, and Coco for having the time of my life during my study in Hamburg.

My girlfriend Hella for being always there for me, encouraging me, and supporting me. Thank you for our wonderful traveling and all the time we spent together so far. And thank you for forgiving me that this was too less during the last months.